ADVANCED SCIENCE
Open Access
www.advancedscience.com

Recent Advances in 2D Metal Monochalcogenides

Abdus Salam Sarkar and Emmanuel Stratakis**

The family of emerging low-symmetry and structural in-plane anisotropic two-dimensional (2D) materials has been expanding rapidly in recent years. As an important emerging anisotropic 2D material, the black phosphorene analog group IV_A–VI metal monochalcogenides (MMCs) have been surged recently due to their distinctive crystalline symmetries, exotic in-plane anisotropic electronic and optical response, earth abundance, and environmentally friendly characteristics. In this article, the recent research advancements in the field of anisotropic 2D MMCs are reviewed. At first, the unique wavy crystal structures together with the optical and electronic properties of such materials are discussed. The Review continues with the various methods adopted for the synthesis of layered MMCs including micromechanical and liquid phase exfoliation as well as physical vapor deposition. The last part of the article focuses on the application of the structural anisotropic response of 2D MMCs in field effect transistors, photovoltaic cells nonlinear optics, and valleytronic devices. Besides presenting the significant research in the field of this emerging class of 2D materials, this Review also delineates the existing limitations and discusses emerging possibilities and future prospects.

1. Introduction

Since the successful isolation of graphene,[1] research in atomically thin 2D materials has gained intensive interest. In particular, beyond graphene materials such as hexagonal boron nitride (h-BN),[2–4] transition metal dichalcogenides (TMDs),[2,4–6] multinary layered chalcogenides,[7] perovskites,[8–10] and MXenes[11–13] have opened up a new horizon in 2D material research. These 2D materials possess intriguing optical, electronic, mechanical, and optoelectronic properties, and are being explored for rich physics and many emerging scientific applications.[1,3–5,9,12,14,15] However, completing the intensive research on semimetal graphene and beyond graphene semiconducting 2D materials, group V element black phosphorene (BP) discovered as a 2D material in 2014,[16] leading to many discoveries of novel physical phenomena.[16–20] The puckered or wavy lattice structure with reduced crystal symmetry (D_{2h}) than graphene (D_{6h}) and TMDs make it more interesting for exhibiting the novel physical phenomena. Moreover, layer-dependent tunable bandgap,[21] high carrier mobility,[16,20] and strong in-plane anisotropy[18] make it promising for next-generation emerging electronic and photonic applications. The electronic bandgap of BP varies from 0.33 to 2.0 eV, when the thickness reduced to a monolayer. An ultrathin layer of BP revealed an extraordinary electrical hole mobility ≈5×10^3 cm^2 V^{-1} s^{-1} at room temperature,[22] which is much higher than the TMDs,[23] making it suitable for advanced electronic applications. Most importantly, in-plane anisotropic optical and electrical response along *x*-direction (armchair) and *y*-direction (zigzag) was directly visualized and studied, which added a new dimension.[18,24] Besides this, unique structural in-plane anisotropic nature in BP played a critical role in designing multifunctional and tunable 2D novel electronic, optoelectronic, and photonic devices.[17,18] In spite of a series of exotic novel physical phenomena, rapid ambient degradation of phosphorene is a critical issue for its practical implementations.[25–27]

Most interestingly, beyond graphene 2D materials, BP's isostructural and isoelectronic group IV_A–VI metal monochalcogenides (MMCs), with chemical formula MX (M = Si, Ge, and Sn and X = chalcogens) has been surged as a star 2D material (**Figure 1**) due to the low-cost, earth-abundant, and environmentally friendly features.[28–33] In 2015, first theoretical and experimental works revealing the electronic properties of monolayer or few-layer MMCs were published.[31,34] The results showed a direct and indirect bandgap with 1.0–2.3 eV energies covering part of the infrared and visible range, which is higher than the BP. Thereafter, the phonon-limited electronic carrier mobilities of MX monolayers are estimated theoretically to be on the order of 10^3 to 10^5 cm^2 V^{-1} s^{-1} by Xu et al.[35] Highest anisotropic electronic response ratio in a few-layer MXs has been recorded along armchair and zigzag direction to be ≈5.8,[36] which is larger than the existing anisotropic 2D materials. Most notably, monolayer MMCs

Dr. A. S. Sarkar, Dr. E. Stratakis
Institute of Electronic Structure and Laser
Foundation for Research and Technology-Hellas
Heraklion, Crete 700 13, Greece
E-mail: salam@iesl.forth.gr; stratak@iesl.forth.gr
Dr. E. Stratakis
Physics Department
University of Crete
Heraklion Crete 710 03, Greece

The ORCID identification number(s) for the author(s) of this article can be found under https://doi.org/10.1002/advs.202001655

© 2020 The Authors. Published by Wiley-VCH GmbH. This is an open access article under the terms of the Creative Commons Attribution License, which permits use, distribution and reproduction in any medium, provided the original work is properly cited.

DOI: 10.1002/advs.202001655

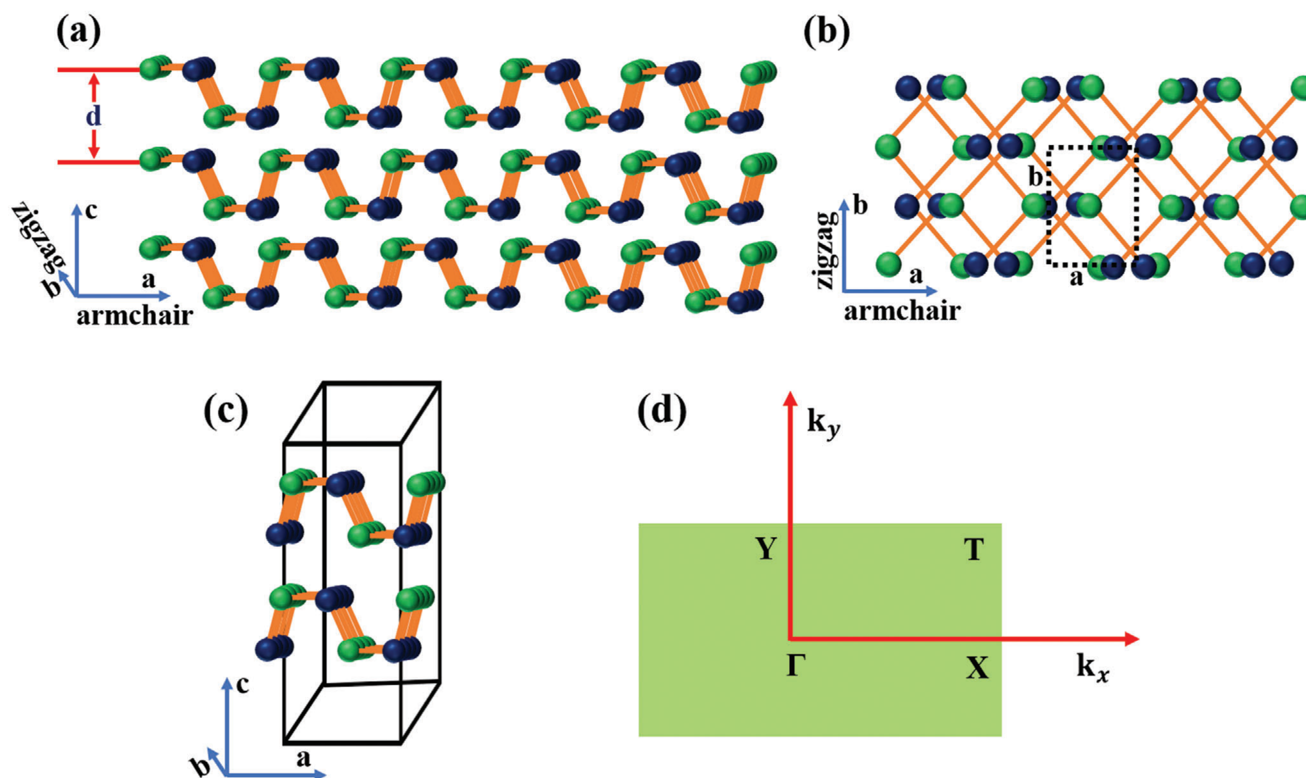

Figure 1. Atomic structures of phosphorene analogous MXs: a) side view and b) top view with the lattice vectors **a** and **b** along the *x* (armchair) and *y* (zigzag) directions. Green atoms are metal (M = Si, Ge, and Sn) and blue atoms are group VI chalcogens (X = S and Se). Each single layer is of thickness of *d* nm. c) The orthorhombic unit cell of MXs and d) the first Brillouin zone with high-symmetry points Γ, X, T, and Y. k_x, k_y momentum along armchair and zigzag direction.

exhibit orthorhombic crystal structure (*Pnma* space group) with low crystal symmetry C_{2v}, in which the inversion symmetry is further broken, which makes them possible to observe new order parameters (spin–orbital coupling) and polarization properties. Many exotic phenomena have been predicted on a monolayer MMCs, including valley physics,[37] spontaneous polarization and bulk photovoltaic effect,[38–41] piezo-phototronic,[42] giant piezoelectricity,[43] ferroelectricity,[44–47] multiferroics of ferroelectricity,[48] and ferroelasticity.[49] However, valley selective dichroism,[50] and more than 90% room temperature valley polarization (VP) degree[51] in SnS provide a completely novel platform for valleytronics. In addition, the giant optical second harmonic generation (SHG) in MMCs is also promising in nonlinear optoelectronic applications.[46,52]

In this article, the latest advances in the field of the emerging 2D group IV_A–VI metal monochalcogenide materials (MMCs) are reviewed. The intriguing physical (crystal and electronic structure) and optical properties are initially highlighted and discussed. Then the various methods that have been employed for the synthesis of such materials, including mechanical and liquid phase exfoliation, as well as vapor phase deposition techniques are demonstrated. Besides presenting the potential and significance of 2D MMCs in various electronic applications it will also delineate the existing limitations and discuss emerging possibilities and future prospects.

2. Crystal Structure and Properties of MMCs

2.1. Crystal Structure of MMCs

The monolayer crystal structure of group IV_A–VI MMCs is isostructural with orthorhombic black phosphorene.[28,31] The chemical formula of MMCs is the MX, where M is group IV metals (Si, Ge, Sn) and X is chalcogens (S and Se). M and X atoms are alternate with each other and form a puckered or wavy layer structure of zigzag (*y*) and the armchair (*x*) plane (Figure 1a,b).[28,31,41,53] In MXs, the presence of two atomic species (M and X) with different electronegativity lowers the crystal symmetry compared to other 2D crystals. In particular, the bulk structure belongs to the space group *Pnma* (D_{2h}^{16}), while in the monolayer, the inversion symmetry is broken placing them in the D_{2v}^{7} space group. The MXs monolayer has four atoms per unit cell (Figure 1b,c), in which each atom is covalently bonded to three neighbors of the other, forming zigzag (*y*) rows of alternating elements. The corresponding first Brillouin zone, as well as the high-symmetry points along armchair (*x*) and zigzag (*y*) directions, are indicated in Figure 1d. The valence electronic configuration of metal (M) and chalcogens (X) atoms are $4d^{10}ns^2np^2$ and ns^2np^4, where *n* is the periodic number of the element. MMCs show strong covalent bonding in the 2D plane and a strong interlayer force owing to the lone pair electrons, which generate a large electron distribution and electronic coupling between

 © 2020 The Authors. Published by Wiley-VCH GmbH

Table 1. Summary of typical MMCs crystal structure parameters and their properties.

MMCs	Space group	Crystal structures	Lattice parameters [Å]	Distance d[a)] [nm]	References
SiS		Orthorhombic	$a = 4.61$; $b = 3.27$	0.228–0.234	[62,63]
SiSe		Orthorhombic	$b = 5.0$; $b = 3.54$	0.246–0.249	[63,64]
GeS	D_{2h}^{16}	Orthorhombic	$a = 4.3$; $b = 10.47$; $c = 3.65$	0.56	[65–67]
GeSe	D_{2h}^{16}	Orthorhombic	$a = 10.84$; $b = 3.83$; $c = 4.39$	–	[67–69]
SnS	D_{2h}^{16}	Orthorhombic	$a = 4.33$; $b = 11.19$; $c = 3.98$	0.56	[70]
SnSe	D_{2h}^{16}	Orthorhombic	$a = 11.49$; $b = 4.15$; $c = 4.44$	0.62	[71,72]

a) Distance d is thickness of a monolayer MXs.

adjacent layers.[54–57] The MMCs are layered p-type semiconductors with 1:1 stoichiometry, with most studied examples being SiS, SiSe, GeS, GeSe, SnS, and SnSe. In particular, SnS has typical acceptor states, which are formed by Sn vacancies (V_{Sn}). On the other hand, sulfur vacancies (V_s) can also be formed, under appropriate Sn-rich conditions, as well as substitutional oxygen at sulfur sites (O_S), leading, in all cases, to p-type conductivity.[58] Stereochemically, active lone pair electrons in group IV metals electronic configuration, ns ($n = 5$ or 4), play a pivotal role in the structural distortion, resulting in the anisotropic crystal and layered structure.[57,59,60]

The physical properties of the MMCs are closely related to their crystal structure, which immensely influences the optical and electronic properties. Indeed, MXs exhibit various crystal phases, such as orthorhombic, hexagonal, and cubic. The exact phase is controlled by the different oxidation states of the metal and chalcogen atoms. For example in Sn-based MMCs, the chalcogen atom has a stronger electronegativity than the metal. As a result, the chalcogen captures two electrons from Sn atom, which leads to a change in its electronic configuration from $4d^{10}5s^25p^2$ to $4d^{10}5s^25p^0$; the same is true for Se-based MMCs, where the electronic configuration of Se changes to $4s^24p^6$.[54,61] As a consequence, the buckled crystal layer structure is distorted (Figure 1). The typical physical properties of the MMCs reported to date are presented in **Table 1**.[62–72]

The exotic physics of 2D materials is usually associated with crystal structural symmetry breaking. In particular, 2D graphene has highest symmetry of D_{6h}, which has sixfold rotation (in-plane), six two-fold perpendicular axis, and a mirror plane. A puckered structure of monolayer black phosphorene exhibits D_{2h} symmetry, which comprises a two-fold rotation axes and one mirror plane, leading to highly anisotropic optical, electronic, and thermal properties.[24,73–77] However, MMCs consist of two elements with different electronegativity, as opposed to the single element in black phosphorene. As a result, inversion symmetry in odd layer is broken to C_{2v}, which, in addition to a two-fold rotation, contains two mirror planes.[43] This unique feature leads to even more extraordinary optical and electronic properties than that of phosphorene and TMDs.[37,39,43,44,47,51,78] Apart from such intrinsic symmetries, other external factors can further tune the electronic properties, including piezo-phototronic and photoactivity.

The bulk structure of Ge and Sn-based monochalcogenides has a layered orthorhombic crystal structure of the space group *Pnma* (D_{2h}^{16}). The structure exhibits strong interlayer forces, giving rise to a distorted NaCl (d-NaCl) crystal structure. As a result, the crystals have different perspective views along a, b, and c axial directions, presenting a unique anisotropic nature. On the other hand, the Si-based monochalcogenides belong to different space groups, for example, the α-SiS monolayer structure.[79]

Table 2. Summary of typical electronic properties of pristine MMC monolayers.

MMCs	Band transition	Bandgap [eV]	VB [eV]	CB [eV]	References
SiS (pristine)	Indirect	1.44	–	–	[79]
		1.37 (at the PBE level)	–	–	[64,71]
SiSe (pristine)	Indirect	1.04 (at the PBE level)	–	–	[64]
GeS	Indirect	2.32	5.41	3.09	[31,80,81]
		2.15	5.31	3.36	
GeSe	Direct	1.54	–	–	[31]
		1.59	4.82	3.23	[80]
SnS	Indirect	1.96	–	–	[31]
		2.03	4.90	2.87	[80]
SnSe	Direct	1.44	–	–	[31]
	Indirect	1.39	4.61	3.22	[80]

2.2. Band Structure, Optical and Carrier Transport Properties

The electronic band structure of 2D materials is crucial for the understanding of the electronic and optical processes occurring in versatile electronic and photonic device applications. In particular, the layer-dependent electronic band structure of phosphoreneanalogue MMCs has been investigated by Gomes and Carvalho.[31] A tunable bandgap (E_g) with direct or indirect bandgap energy within the visible range is reported (**Table 2**). The electronic structures and properties were obtained by calculating the band structures using the Heyd-Scuseria-Ernzerhof (HSE) function. On the other hand, *ab initio* density functional theory using the Perdew-Burke-Ernzerhof (PBE) exchange correlation function, is used for SiS and SiSe, respectively. Moreover and as shown in **Figure 2**, the band structure topologies are common and similar to all MMCs. Besides this, the dispersion of the bands nearest to the gap is nearly the same along the Γ-X and Γ-Y directions, while the electronic configuration of the metal plays a critical role in such dispersion. Furthermore, apart from the

 © 2020 The Authors. Published by Wiley-VCH GmbH

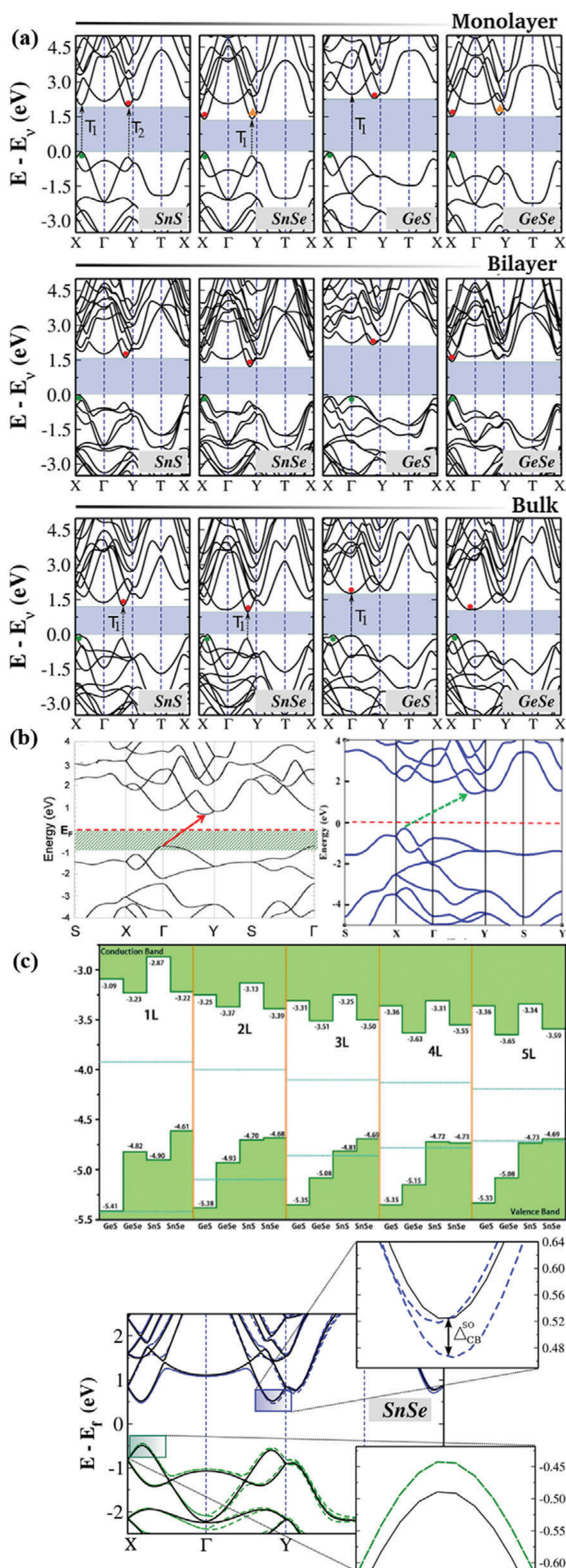

Figure 2. a) Electronic band structures for monolayer, bilayer, and bulk MMCs (calculated using the Heyd-Scuseria-Ernzerhof (HSE06) hybrid functional). Solid circles are VBM and CBM. Black arrows (dashed) are possible direct transitions (T1 and T2) to points very close in energy to the VBM and CBM. Reproduced with permission.[31] Copyright 2015, American Physical Society. b) Electronic structure of SiS monolayer, calculated using density functional theory (DFT) (left panel). Reproduced with permission.[79] Copyright 2015, American Chemical Society; SiSe monolayer calculated using HSE06 hybrid function (right panel). Reproduced with permission.[64] Copyright 2015, American Chemical Society. c) Top panel: Calculated band alignments of MXs of 1–5 layers (L) (at the HSE06 level). Reproduced with permission.[80] Copyright 2017, Royal Society of Chemistry. Bottom panel: Electronic band structure of SnSe monolayer with (dashed lines) and without (continuous lines) spin–orbit coupling effect. Reproduced with permission.[31] Copyright 2015, American Physical Society.

monolayer of GeSe, mono- and bi- layer GeS and bulk GeS exhibit indirect bandgap. Although, SnS has an indirect bandgap (calculated with HSE) regardless of the layer number. The corresponding E_g value is 1.96, 1.60, and 1.24 eV for monolayer, bilayer, and bulk SnS, respectively. In case of monolayer, bilayer, and bulk, the valence band maxima (VBM) and conduction band minima (CBM) are located along the Γ-X and Γ-Y lines (Figure 2). However, in case of monolayer, there are competing local CBM and VBM, which are very close in energy to the band edges. In a monolayer SnSe, the direct gap of 1.44 eV is calculated along the Γ-X line. However, an additional direct transition at 1.60 eV (T1) occurs in the Γ-Y direction. In addition, the monolayer GeS shows an indirect bandgap of 2.32 eV, which is along the Γ-X and Γ-Y lines of CMB and VBM. Mono- and bilayer GeSe shows a direct bandgap of 1.54 eV (along Γ-X line) and 1.45 eV (along Γ-X line, near the X point), respectively. The energy bandgap of such monolayers was verified by other methods, reported by Huang et al., Gong et al. and Wang and co-workers (Figure 2c).[80–82] In this work, the energy band alignment of CBM and VBM with respect to the vacuum level in MMCs with different number of layers has been estimated. The CBM exhibits a significant downshift, while the VBM remains relatively the same. Such change in the electronic band structure with layer number is quite similar among MMCs. The agreement was well fitted, except for the monolayer SnS, attributed to the presence of shallow core *d* bands. Apart from the mono- and bi- layer MMCs, the bulk electronic structure is also shown in Figure 2. The calculated bandgaps are 1.40, 1.00, 1.81, and 1.07 eV corresponding to the SnS, SnSe, GeS, and GeSe, respectively.

On the other hand, SiS and SiSe monolayers exhibit an indirect bandgap of 1.44 and 1.04 eV, respectively (Figure 2b).[64,79] Apart from the band structure, the spin–orbital coupling in monolayer MMCs has been estimated using a generalized gradient approximation (GGA) method. Such coupling solely depends on the inversion symmetry of the crystal itself, which is related to the presence of odd/even number of layers in MXs. In general, MMCs monolayers exhibit a very similar electronic band structure with and without spin–orbital coupling. However, in case of SnSe (Figure 2c) and GeSe the spin–orbital coupling is due to the conduction band splitting, while the VBM remains the same along Γ-X for all the cases. As shown in **Table 3**, the estimated spin–orbital coupling in SnS (CBM) is the largest among MMCs. Moreover, it is striking that the spin–orbital splitting in MMCs conduction band exceeds that of other 2D materials, for which the corresponding splitting lies between 3 and 30 meV (Table 3).[83]

The investigation of intrinsic electronic and optical properties of 2D materials is not only crucial for fundamental studies but also from applications perspective. During the last decade, a se-

 © 2020 The Authors. Published by Wiley-VCH GmbH

Table 3. Optical and electronic properties of MMCs.

MMCs	Absorption coefficient [cm^{-1}]	Carrier mobility [cm^2 V^{-1} s^{-1}]	Electronic properties	Spin–orbital coupling		References
				Δ_{VB}^{SO}	Δ_{CB}^{SO}	
SiS	10^5–10^7	1.50×10^3 (zigzag) 1.80×10^4 (armchair)	p-type	–	–	[62]
GeS	1.6×10^5	2.4×10^3	p-type	1	56	[31,36,66,87,89]
GeSe	10^5–8×10^5	$\approx 10^3$	p-type	9	48	[31,35,84]
SnS	5×10^4 to 5.7×10^5	$\approx 10^3$		8	87	[31,35,89]
SnSe	2×10^4 to 9.5×10^4	10^4	p-type	14	52	[31,35,84,88]

ries of reports have been focused on the theoretical investigation of such properties for monolayer 2D MMCs.[31,33,35,39,42,80,84–89] In particular, Feng and co-workers[35] systematically investigated the electronic mobility in monolayer MMCs and adopted a phonon-limited scattering model to interpret the physical phenomena occurring. In a 2D system, the mobility is provided by the formula $\mu_{2D} = \frac{e\hbar^3 C_{2D}}{k_b T m_e^* m_d (E_1^i)^2}$, where m_e^* is the effective mass of the electron along the transport direction and m_d is the average carrier effective mass. Using this formula, the predicted carrier mobilities for MMCs monolayers are in the order of 10^3–10^5 cm^2 V^{-1} s^{-1}, while there are highly structural in-plane anisotropic in nature along armchair and zigzag direction (Figure 1). For example, the electron mobilities of Ge and Sn-based monochalcogenides are higher along the armchair and zigzag direction, respectively. Exceptionally high carrier mobilities revealed in SnSe monolayer are attributed to the small effective masses and low deformation potential constants, along a particular direction (armchair or zigzag). Such carrier mobilities are highly anisotropic compared to BP and other 2D TMD monolayers. Besides the high carrier mobilities, the monolayer MMCs exhibit piezoelectricity, with large piezoelectric constants.[90] Such piezoelectricity is more pronounced than that in other 2D systems, such as hexagonal BN and TMD monolayers.[42]

3. Methods for MMCs Preparation and Characterizations

Since the first exfoliation of graphene, many methods have been developed to isolate ultrathin layers of 2D materials. All such methods are divided into top-down and bottom-up ones. The top-down approach relies on the exfoliation of thin 2D crystals from their parent layered bulk crystals and the most important are based on mechanical (ME), liquid phase (LPE), and electrochemical exfoliation (EE).[4,5,91–93] While, the most important bottom-up approaches include wet chemical synthesis (WCS), pulsed laser and chemical vapor deposition (PLD and CVD). Those methods are based on chemical reactions of certain precursors at given experimental conditions. In the following, we summarize the recent developments in the synthetic methods employed to produce ultrathin and single-layer MMCs.

3.1. Top-Down Methods

3.1.1. Mechanical Exfoliation

ME has been widely employed for obtaining few-layer and monolayers of graphene, TMDs, and BP from their bulk counterparts.[1,23,94] Generally, the mechanical force is employed via scotch tape to weaken the van der Waals interaction between the adjacent layers of 2D bulk crystals and peel off single- or few-layered flakes. This technique can produce high-quality and clean surface crystals, which is favorable for both fundamental studies and technological applications. Besides this, the clean surface attained in mechanically exfoliated 2D materials makes them more suitable to stack and form good-quality van der Waals heterostructures.[95–97] To date, there are few reports on ME of thin layer of 2D MMCs, such as GeS,[98–100] GeSe,[101–103] SnS,[50,57,104] and SnSe.[36,105,106] Owing to the high interlayer binding energy of MMCs, the exfoliation of an atomically thin single layer is quite difficult.

Tan et al.[107] has isolated the ME of thin layers of GeS, with various thickness (65 to 8 nm). The crystal quality of the exfoliated flakes was verified with Raman spectroscopy. As mentioned earlier, MMCs belong to the orthorhombic crystal structure *Pnma* (D_{2h}^{16}) crystal symmetry. In this structure, 24 phonon modes at the center of the Brillouin zone can be expressed as

$$\Gamma = 4A_g + 2B_{1g} + 4B_{2g} + 2B_{3g} + 2A_u + 4B_{1u} + 2B_{2u} + 4B_{3u} \quad (1)$$

where A_g, B_{1g}, B_{2g}, and B_{3g} are optically active Raman modes.[108–110] The Raman spectra of GeS exhibited three characteristic peaks, which are assigned to B_{3g}, A_g^1, and A_g^2 phonon modes. The B_{3g} and A_g modes, in particular, correspond to the in-plane shear vibration of adjacent layers parallel to one another in the x (armchair) and y (zigzag) directions, respectively (**Figure 3**c). Furthermore, chemical vapor transport (CVT) grown single crystal bulk GeS was utilized for the mechanical exfoliation of thin nanosheets (NSs).[98] The isolated flakes were highly crystalline in nature, few tens of nanometer thick, and micrometer-sized in lateral dimensions. Ulaganathan et al.[66] have isolated an ≈28 nm thin layer of GeS (Figure 3a), exhibiting a highly crystalline and large smooth surface, investigated for anisotropic electronic response. On the other hand, GeS flakes of variable thickness have been isolated by Li and co-workers.[98] Atomic force microscopy (AFM) imaging of the multilayer GeS flakes showed a three-step stack of up to about few hundreds of nanometers.

 © 2020 The Authors. Published by Wiley-VCH GmbH

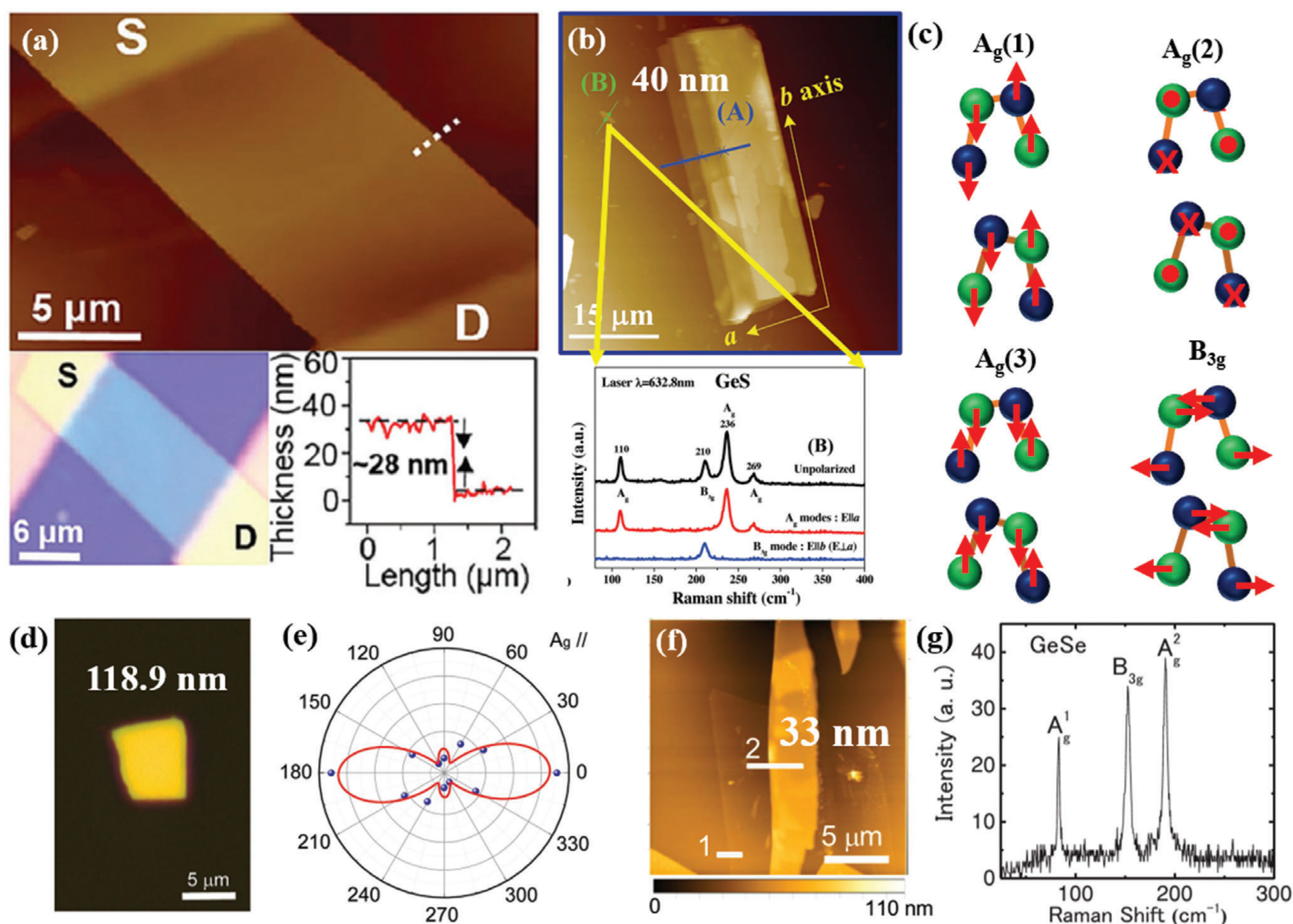

Figure 3. Mechanically exfoliated GeS and GeSe flakes. a) Atomic force (top panel) and optical microscopy (bottom panel) images. The thickness of the GeS flake is ≈28 nm (along the white dashed line (in top panel)). S and D correspond to source and drain, respectively. Reproduced with permission.[66] Copyright 2016, Royal Society of Chemistry. b) AFM image of exfoliated GeS flake with a thickness from 40 nm (solid green line B) to three-step stack of up to about 270 nm (solid blue line A). Polarized Raman spectra of the 40 nm-thick GeS flake (bottom panel). Reproduced with permission.[98] Copyright 2017, Wiley-VCH. c) Schematic representation of the motion of atoms for the different Raman active modes in MXs. d) Optical image of GeSe flake. e) Angle-resolved polar plot of the Raman peak intensity of A_g mode (188 cm^{-1}, Laser: 532 nm laser under parallel configuration). Reproduced with permission.[103] Copyright 2019, Wiley-VCH. f) AFM image with height profile of GeSe (indicate by line 2) and 3L-MoS_2 heterojunction, and g) Raman scattering spectra of a 33 nm GeSe flake (Laser line used: 532 nm). Reproduced with permission.[101] Copyright 2018, Wiley-VCH.

The thinnest flake obtained was measured to be ≈40 nm (Figure 3b). In such thick flake, four vibrational Raman modes were detected using unpolarized light, namely, at 110, 210, 236, and 269 cm^{-1} corresponding to A_g and B_{3g} symmetric modes; the position of such modes well agreed with theoretical predictions.[109] The anisotropic Raman response was clearly detected upon using parallel and perpendicular incident laser light.

Furthermore, few tens of nanometers thick GeSe flakes were micromechanically exfoliated by several groups.[103] In particular, Yang at al.[103] exfoliated 118.9 nm-thick flakes (Figure 3d), which were further investigated for their anisotropic optical properties. It is observed that the polarization dependent Raman spectra exhibited a periodic change in intensity with rotational angle (Figure 3e), corresponding to the two crystalline orientations along armchair and zigzag directions, respectively. The respective spectra were fitted using the classical Raman selection rules,[108,109] expressed by the relation $I \infty |e_i.R.e_s|^2$, where, e_i and e_s are the unit polarization vectors of incident and scattered light, and R is the Raman tensor.

Zhu and co-workers[102] isolated thinner GeSe flakes (230 to 14 nm) via ME to explore the anisotropic nature in current transport.[111,112] The anisotropy in structure of a GeSe flake was realized by the angular resolved polarized (ARP) Raman spectroscopy. Yang et al.[103] have adopted mechanical exfoliation to produce a few tens to hundreds nanometers thick flakes, which are highly anisotropic in nature. In anisotropic materials, when the polarization direction of the incident laser light is parallel to a crystal orientation (armchair or zigzag), the intensity of the optically active Raman modes reached a maximum or secondary maximum value.[113] A much thinner layer of GeSe flakes was isolated by Matsuda and co-workers[101] A stacked GeSe/MoS_2 heterojunction was reported (Figure 3f). A much thinner GeSe layer of 33 nm thickness was identified by the AFM height analyzer (Figure 3f). The Raman scattering spectrum of such thin

© 2020 The Authors. Published by Wiley-VCH GmbH

layer revealed the characteristic peaks at 83.4, 152.5, and 190.4 cm^{-1}, assigned to A_g^1, B_{3g}, and A_g^2 phonon modes (Figure 3g), respectively.[111] The Raman peaks were shifted to the higher wavelength range compared to a 14 nm GeSe flake.[102] The observed phonon mode shift with lowering the layer number in GeSe is similar to other anisotropic 2D materials such as black phosphorene.[114–116] However, there is no systematic study of layer number dependent Raman scattering evolution in mechanically exfoliated GeSe flakes.

The successful isolation of few layers of SnS and SnSe flakes has been experimentally realized via micromechanical exfoliation.[36,50,57,104,106,117] Nagashio and co-workers[118] produced thin layers of SnS flake by a micromechanical exfoliation method which was mediated by a tape exfoliation and aurum exfoliation (Au). The obtained flakes showed a wide range of distribution in size and thickness. The strong interlayer ionic bonding and the large electron distribution by lone pair electrons in Sn played a critical role to isolate them in large-area ultrathin layers. As also mentioned earlier the interlayer binding energy in a MXs is 146 meV per atom, which is much larger than those of graphite (24 meV per atom) and MoS_2 (38 meV per atom).[54,56] However, the tape-exfoliated SnS flakes were of several micrometers in lateral dimensions, with tens of nm thickness. On the contrary, much larger SnS flakes were obtained via the Au-mediated exfoliation approach. In this method, a strong semicovalent bonding between Au and S atoms enabled the isolation of larger ultrathin SnS layers. A significant surface roughness was observed in exfoliated flakes (≈0.1 nm), which may serve to produce a good quality interface with other 2D materials.[119–122] In another study, valley selective dichroism was identified in layered SnS by Chen et al.[50] The Raman vibrational modes, measured in a SnS flake about 109 nm-thick (**Figure 4**a), displayed a typical Lorentz shape peaking at 161, 191, and 217 cm^{-1}, corresponding to B_{3g}, A_g^1, and A_g^2 modes, respectively. As pointed out before, the structural anisotropy (along armchair and zigzag direction) is an important feature in 2D MMCs, which originates from the stereochemically active lone pair electrons in Sn 5s.[59,60,123] Therefore, the polarization dependence of the Raman scattering is a convenient way to determine the crystal orientation. Accordingly, the angular-resolved Raman scattering spectrum was recorded (Figure 4b) and the respective modes' intensity was displayed in a polar plot. The A_g mode intensity well followed the $a\cos^2 2\theta+b$ dependence, where θ is the polarization angle, a and b are fitting parameters. On the other hand, the B_{3g} mode intensity showed a $a\sin^2 2\theta+b$ dependence. Such observation of distinct fitting behavior of A_g and B_{3g} Raman modes is attributed to the different Raman tensors governing them,[70,124] which determine the structural anisotropy in armchair ($\theta = 0°$) and zigzag directions, respectively. Furthermore, a much thinner layer was isolated by Nagashio and co-workers.[57]

These cotch tape and Au exfoliation methods were adopted to isolate such thin flakes. The Au-exfoliated SnS flakes exhibited various thicknesses (Figure 4c,d), with the thinnest layer to be ≈4.3 nm. However, upon Au exfoliation, surface modification was observed, which badly affects the nanosheet properties. The formation of amorphous tin oxide (a-SnO_x) is revealed at the surface of the intrinsic SnS, in particular (Figure 4e,f).

Cho et al.[105] exfoliated a single crystal, prepared by the modified Bridgman technique to produce single-phase orthorhombic SnSe flakes, with the *Pnma* space group. Similar methodology was employed by Yang et al.[36] to prepare bulk SnSe flakes ranging from few tens to hundreds of nanometer thickness. It is shown that a 71 nm-thick SnSe crystal exhibited orthogonal geometry. In such crystal, the intersection angle of the two crystal planes is determined to be 90°.[126] A strong fourfold anisotropy with a period of 90° and minimum intensities along the 0° and 90° directions, identified as zigzag and armchair directions, respectively. Such anisotropic Raman spectral behavior in MXs is strongly dependent on the phonon symmetry, which was observed in other 2D materials having in-plane structural anisotropy.[127–131] In another study, a much thinner flake of SnSe was isolated by Zheng and co-workers.[106] The high quality of the SnSe flake was visualized by noncontact atomic force microscopy (nc-AFM) showing that very few vacancies were present. The crystal phase of the SnSe flake was identified by the corresponding Raman spectra (Figure 4g,h). Interestingly, Wei and co-workers[125] have isolated a 28 nm-thick SnSe flake (Figure 4i) to produce a heterostructure with molybdenum disulfide (MoS_2). The heterostructure was further used for electronic and optoelectronic investigations. In particular, the vibrational modes exhibited four characteristic peaks at 69.5, 109.0, 130.6, and 149.5 cm^{-1}, associated to A_g and B_{3g} active Raman modes.

In spite of the great advantages of the ME method, including that it is a relatively easy process and provides high-crystalline quality 2D flakes, the MMCs produced suffer from size repeatability and reproducibility of the layer number. At the same time, owing to the strong interlayer force and in-plane anisotropy the isolation of a single layer is still a challenge. In contrast, liquid phase exfoliation and chemical vapor deposition have been employed for the isolation of thin-layer, large-area, and controllable morphology nanosheets.

3.1.2. Solution or Liquid Phase Exfoliation

LPE is a well-known strategy to produce ultrathin layered 2D materials and has thus been extensively used to exfoliate 2D layered graphene and other crystals.[4,91,132–134] The method has been developed and advanced by Coleman and co-workers[132,135] in 2008 and has considered to be one of the most promising and simplest routes for the production of 2D materials in a large scale. It generally involves the process in which bulk layered crystals or powders are dispersed in a suitable solvent and are subjected to ultrasonication for a certain amount of time. Following ultrasonication, the suspension is centrifuged to separate the unexfoliated bulk and exfoliated thin NSs. The fundamental idea is that ultrasonic waves can induce liquid cavitation in the dispersion, which in turn leads to cavitation bubbles. The generated bubbles collapse onto the dispersed material. As a consequence, intensive tensile stress is applied to the dispersed bulk crystals, giving rise to thin layer exfoliation.

A critical factor for the success of LPE of layered 2D materials is the selection of appropriate solvent. Indeed, the solvent screening critically depends on the Hildebrand and Hansen solubility parameters.[136,137] However, recent reports have demonstrated that neither Hildebrand nor the Hansen parameters can

 © 2020 The Authors. Published by Wiley-VCH GmbH

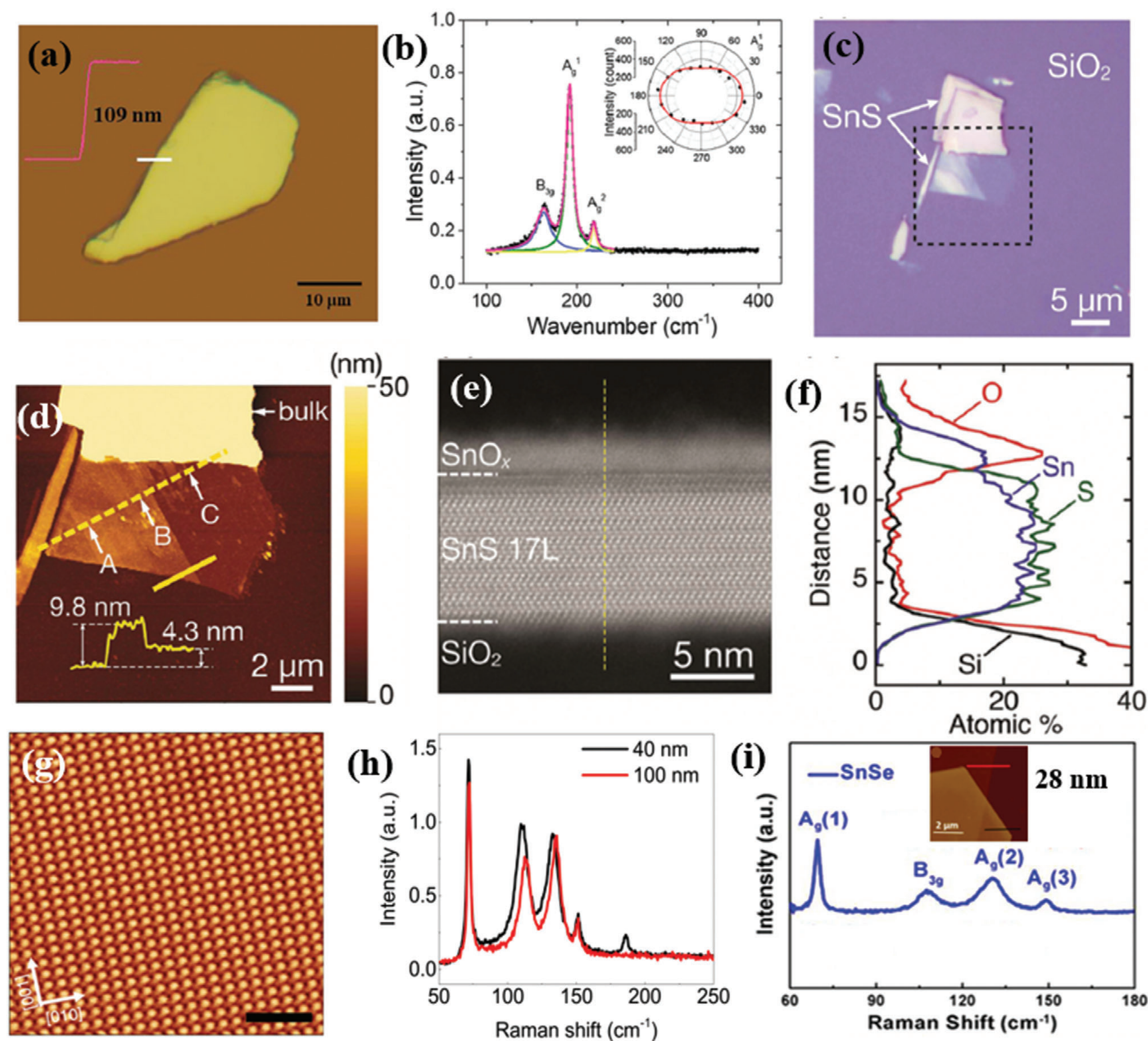

Figure 4. a) Optical microscopy image of a mechanically exfoliated, 109 nm-thick, SnS flake on SiO_2/Si substrate; the corresponding AFM height profile is shown in the inset. b) Raman scattering spectra of the SnS flake. The solid lines (blue, green, and yellow) are Lorentz- fitting curves of the active Raman modes; The angular-resolved Raman intensity of the A_g^1 mode is shown in the inset. The $\theta = 0°$ corresponds to the armchair, x direction of the crystal. Reproduced with permission.[50] Copyright 2018, American Chemical Society. c) Optical image of exfoliated SnS. d) AFM topography of the selected area in (c). Inset is the height profile along the solid yellow line. e) Cross-sectional high-angle annular dark-field scanning transmission electron microscopy (HAADF-STEM) image (at the point A in (d)). f) Energy-dispersive X-ray spectroscopy (EDS) depth profile along the dashed line in (e). Reproduced with permission.[57] Copyright 2018, Royal Society of Chemistry. g) Atomic-resolution noncontact atomic force microscope (nc-AFM) image of stoichiometric SnSe flake; the inset shows a typical optical image of $SnSe_2$ microdomains on SnSe. h) Raman spectra of the SnSe flake shown in (g). Reproduced with permission.[106] Copyright 2018, Author(s), licensed under a Creative Commons Attribution 4.0 License, Published by Springer Nature, and i) room-temperature Raman spectra of SnSe flake. Inset shows AFM height profile along the red line. Reproduced with permission.[125] Copyright 2017, American Chemical Society.

fully describe the solvent–solute interaction during the LPE of 2D materials.[138] Thermodynamic laws suggest a lower difference in surface energy between the 2D material to be exfoliated and the solvent is beneficial for LPE.[132,137] Besides this, the ultrasonication time, the temperature during ultrasonication, as well as the centrifugation rate, are critical parameters for efficient exfoliation, both from qualitative and quantitative point of view.[135,139] To date, few reports on the LPE synthesis of ultrathin layer MMCs have been presented, referring to GeS, GeSe, SnS, and SnSe (**Table 4**).[34,110,140–147] In contrast, there is no experimental evidence on the LPE of SiS and SiSe.

© 2020 The Authors. Published by Wiley-VCH GmbH

Table 4. Summary of the experimental synthesis of metal monochalcogenides (GeS, GeSe, SnS, and SnSe) via LPE.

MMCs	Synthesis method	Solvent	Average thickness [nm]	Lateral dimension [nm]	Layer number	References
GeS	LPE	Hexene, ethanol, IPA, NMP, DMF, acetone, chloroform	2.87 ± 0.65 (NMP)	66.91 ± 0.42	6 layers	[140]
GeS	LPE	NMP	1.3 ± 0.1	–	Tri-layer	[143]
GeSe	LPE	Ethanol	2	50–200	4 layers	[141]
GeSe	LPE	NMP	4.3 ± 0.2	–	8–9 layers	[142]
SnS	LPE	NMP	4.2 ± 0.24	5–100	6–8 layers	[34]
SnS	LPE	NMP	6	–	Few layers	[144]
SnS	LPE	IPA	4–8	50	Few layers	[146]
SnS	LPE	DMF	4.5	400–900	8 layers	[147]
SnS	LPE	Acetone	1.10	170	Bi-layer	[110]
SnSe	LPE	IPA	4.3	50–500	7 layers	[148]
SnSe	LPE	NMP	2.5	50–200	4 layers	[149]

Hersam and co-workers[140] isolated few-layer GeS NSs via anhydrous solvents LPE of bulk powder (**Figure 5**a). Considering the solvent and solute chemical properties a series of organic solvents exhibiting different surface tensions were investigated. It is reported that the isolated sheets in NMP showed the darkest dispersion (Figure 5b,c), which is an evidence of this solvent suitability to efficiently stabilize the exfoliated GeS sheets. The structural integrity of exfoliated crystals was verified by studying the lattice vibration modes (Figure 5d), including the B_{3g} mode (213 cm^{-1}), corresponding to the in-plane shear vibration of parallel layers in the zigzag direction and the A_g modes (112, 240, and 270 cm^{-1}) corresponding to shear vibration of parallel layers in the armchair direction (*a*-axis). A standard probability density function was used to fit the characteristic size histograms (through AFM) recorded for the exfoliated flakes (Figure 5e–g), namely

$$y = y_0 + \frac{A}{x\sigma\sqrt{2\pi}} e^{-\frac{\left(\ln\frac{\sigma}{\mu}\right)^2}{(2\sigma^2)}} \tag{2}$$

where, y_0 is a constant offset, A is a constant prefactor, x is either the flake thickness or length, σ is log normal standard deviation, and μ is the long normal mean. In another study, a cascade centrifugation method was employed to achieve much thinner layer of GeS sheets by Fan et al.[143] The LPE method was adopted to exfoliate bulk powders in NMP solution in which different centrifuge settings were employed to realize thinner layers. The thickness was found to be as thin as 13.2 ± 2, 4.2 ± 0.3, 3.2 ± 0.2, and 1.3 ± 0.1 nm, corresponding to 2-4k, 4-6k, 6-8k, and 8-10k settings, respectively (Figure 5h). The thinnest layer of GeS achieved was 1.3 ± 0.1 nm (8-10k), which corresponds to approximately two monolayers.

A different method was adopted by Ye et al.[141] The GeSe flakes were prepared via sonication-assisted LPE with cascaded centrifugation. A series of solvents were tested, namely, IPA, DMF, CHP, SDS, and SC, leading to GeSe NSs with quite different lateral size and thickness, which are redispersible. The CHP-exfoliated NSs produced largest lateral size, while exfoliation in IPA produces much smaller sizes. However, the thinner layer, achieved in ethanol, showed lateral dimensions in the range 50–200 nm, which is highly single crystalline in nature with hexagonal structures (**Figure 6**a,b). Even thinner layers were subsequently obtained upon centrifugation at different conditions. In particular, the thickness of the GeSe NSs, obtained at the centrifugation speeds of 9k, 6k, and 3k rpm, showed an average thickness of 2, 5.5, and 6 nm, respectively (Figure 6c–h). The orthorhombic GeSe crystals obtained belong to the D_{2h}^{16} symmetry, which exhibits 12 optically active Raman modes ($4A_g$+$2B_{1g}$+$4B_{2g}$+$2B_{3g}$).[108,111] Three such modes, which are optically active and peaked at 80, 150, and 180 cm^{-1}, correspond to A_g^3, B_{3g}^1, and A_g^1, respectively. Beyond this time, the isolated GeSe sheets showed a bandgap variation from their bulk counterpart. Zhang and co-workers[142] have systematically investigated the sonication effects during the LPE of GeSe NSs. The typical process is demonstrated in Figure 6i. A series of organic solvents were tested including NMP, DMF, water, ethanol, and IPA, and the effect of centrifugation speed (within the ranges 1-14k, 2-14k, and 3-14k) on thickness and lateral size of the exfoliated GeSe was examined.

A significantly decreased size distribution and average lateral size with no discernable oxide phase impurities were detected in the NMP-exfoliated GeSe flakes. While the lowest average thickness was estimated to be around 4.3 ± 0.2 nm (Figure 6j), which correspond to tri-layers based on the previous theoretical calculations.[150–152] Besides this, the exfoliated GeSe sheets are highly crystalline with clear crystal lattice spacing (≈0.23 nm) (Figure 6k).

In 2015, O'Brien and co-workers[34] first reported the LPE of anisotropic layered SnS. Following this work, many research groups have been intensively focused on exfoliation of ultrathin SnS layers.[110,144,145] In the first report,[34] bulk SnS powder was dissolved in NMP and ultrasonication was employed to induce cavitation effects in the dispersion. In particular, the isolated SnS sheets (1500 rpm (Sol A) and 10 000 rpm (Sol B)) exhibited an average height of 4.1 and 7.8 nm, respectively (**Figure 7**a), which corresponds to multilayer SnS. On the contrary, the exfoliated NSs were 50–100 nm in lateral dimension (Figure 7c), often with aspect ratios of around 1.5–2.0. The sharpening in the Raman modes (A_g, B_{3g}, and B_{3u}) in SnS NSs compared to the broad bulk ones was another examination of the thin nature

© 2020 The Authors. Published by Wiley-VCH GmbH

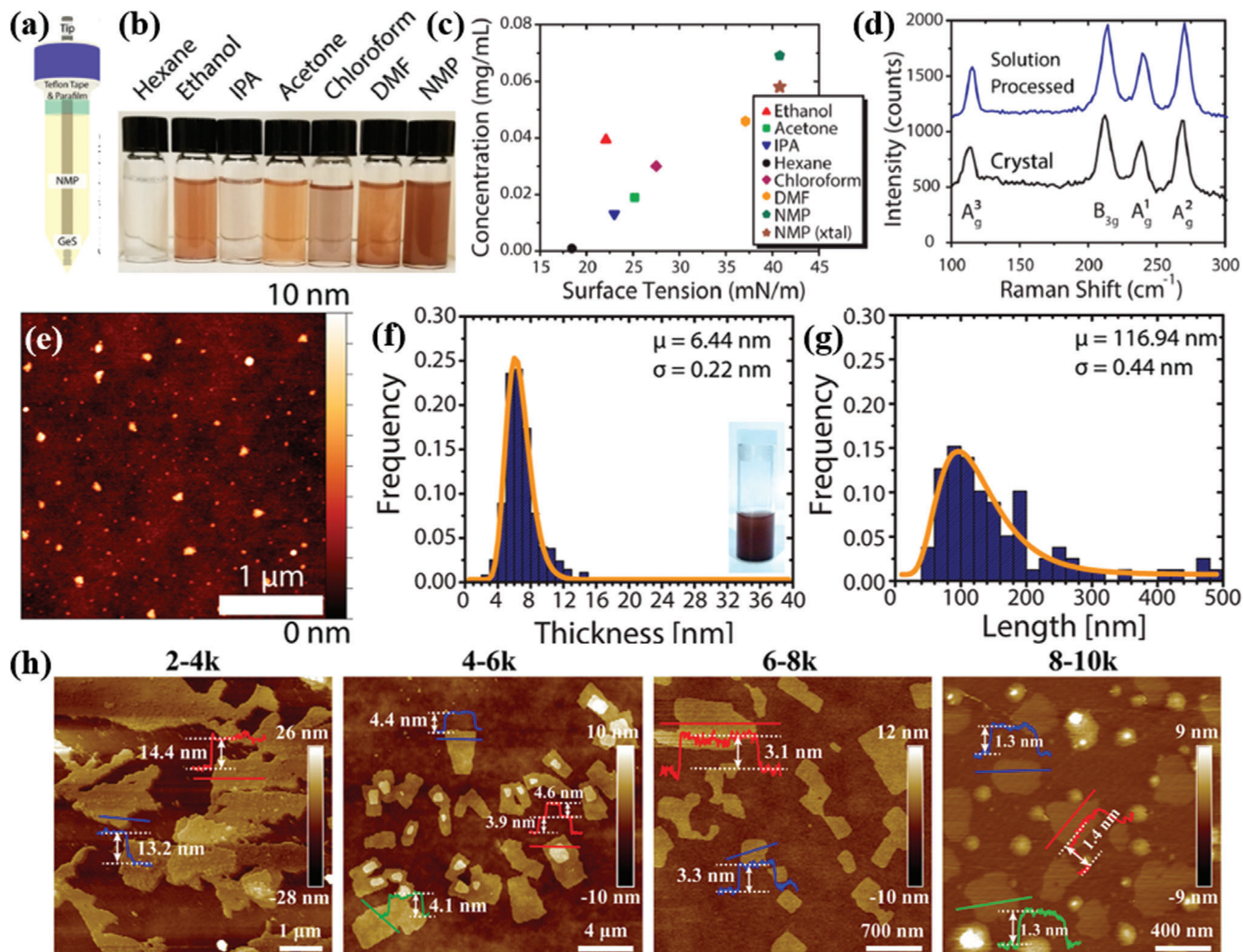

Figure 5. a) Schematic of tip sonicator. The solution tube is sealed with Teflon tape and parafilm to minimize exposure to ambient atmosphere. b) Exfoliated GeS NSs in various solvents (centrifuged at 1000 rpm for 10 min), and c) concentration of exfoliated bulk powder of GeS as a function of solvent surface tension. The NMP-exfoliated GeS is considered as a reference concentration. d) Raman spectra of a bulk GeS crystal and solution-processed GeS flakes. e) AFM topography image of NSs. f) TEM image of NSs. g) Thickness (inset: as-prepared GeS dispersion) and h) lateral size histograms (from statistical TEM analysis) of the as-exfoliated GeS NSs. i) Thickness (inset: centrifuged GeS dispersion at 500 rpm) and j) lateral size histograms (from statistical TEM analysis) of the centrifuged GeS NSs. Reproduced with permission.[140] Copyright 2018, American Chemical Society. h) AFM images, corresponding height profiles, and thickness distribution histograms of LPE GeS NSs collected with different centrifugation speeds. Reproduced with permission.[143] Copyright 2019, American Chemical Society.

of the exfoliated flakes (Figure 7b). In another approach, both a bath and tip sonicator have been employed to create the cavitation events in SnS colloidal dispersion.[144] Liquid cascade centrifugation (LCC) was utilized to prepare size-selected 2D SnS NSs in NMP. The thinnest sheets of 6.0 nm, comprising ten or more monolayers, were separated. The isolation of thin-layer SnS using LCC method is an effective way to exfoliate few-layer SnS sheets, which is in good agreement with other 2D materials prepared by the LCC technique.[153,154] The size-selective Raman modes appeared gradually blueshifted as the thickness of the 2D NSs decreases, which is attributed to the confined oscillation when more layers of SnS are added and bonded by van der Waals forces. Furthermore, a lower boiling point solvent, isopropyl alcohol (IPA), was tested as an exfoliation medium by Zhang and co-workers.[145] A similar approach of LPE by the work of O'Brien and co-workers[34] has followed. The isolated SnS flakes showed a 50 nm lateral dimension with an average thickness of 6 nm. A high-quality crystal with lattice spacing was identified, which confirmed the crystal phase integrity, even after exfoliation. The overall investigation indicated that the low boiling point solvent is more suitable to isolate thin-layer SnS. However, the exfoliated SnS sheets are limited to few nanometers thick.

Most recently, Sarkar et al.[110] have reported the isolation of thinner SnS sheets via pushing one step forward the O'Brien's[34] method. An organic solvent was chosen to exfoliate bulk SnS crystal in a bath sonicator with a power of 100 W and 40 kHz frequency for 10 h. Acetone, in particular, was identified as the most suitable solvent for the successful exfoliation of electronic grade ultrathin SnS layers. The separated SnS sheets showed

© 2020 The Authors. Published by Wiley-VCH GmbH

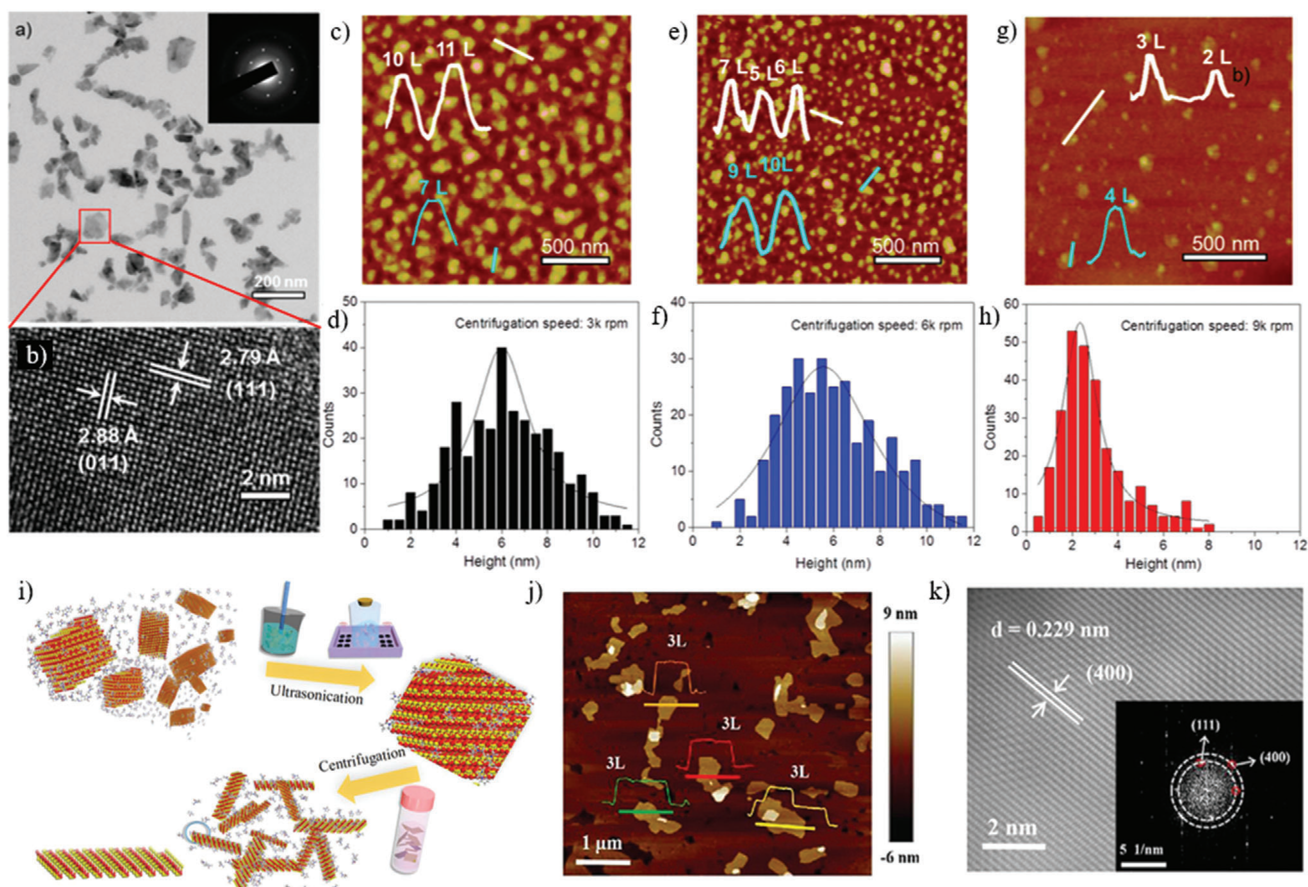

Figure 6. TEM image of a) GeSe sheets (inset: selected area electron diffraction (SAED) pattern taken from a single flake marked by red rectangle), b) high-resolution transmission electron microscopy (HRTEM) image of a GeSe sheet. c,e,g) Height-mode AFM images of exfoliated GeSe NSs collected at different centrifugation speed of 3k, 6k, and 9k, respectively (inset: height profiles). d,f,h) Histogram analysis for the thickness of GeSe NSs such as those shown in the panels (c), (e), and (g), respectively. Reproduced with permission.[141] Copyright 2017, American Chemical Society. i) Schematic illustration of the LPE process used to obtain ultrathin GeSe NSs. j) AFM topography image and height profile of LPE GeSe NSs. k) HRTEM image of exfoliated GeSe NSs in NMP solvent; the inset shows the SAED pattern. Reproduced with permission.[142] Copyright 2019, American Chemical Society.

an average thickness of ≈1.10 nm and average lateral dimensions of ≈170 nm (Figure 7d–f). Those sheets are highly crystalline in nature, as perfect rhombus-like lattice fringes with sharp selected area electron diffraction (SAED) patterns were observed (Figure 7g–i). Besides this, the optical properties of SnS sheets were explored toward thermoelectric and nanophotonic applications.

Nan and co-workers[148] have utilized the LPE of SnSe in a low boiling point solvent IPA. The thinnest NS (≈1 nm), comprising two monolayers of SnSe, was obtained.[155] Very recently, Ye et al.[149] have investigated the intensive LPE of SnSe in seven different solvents and various centrifugation conditions (cascade centrifugation). Among the solvents tested, the NMP-exfoliated SnSe exhibited the larger, in lateral dimensions, flakes. A cascade centrifugation was employed, during which the NSs, collected at 8k rpm exhibited lateral sizes in the range ≈50–200 nm (**Figure 8**a,b). The obtained average thicknesses of NSs 9.5, 6, and 2.5 nm correspond to layer numbers of 16, 10, and 4, respectively (Figure 8g–i). The orthorhombic diffraction pattern, together with the lattice spacing and the highly crystalline order are in well agreement with the crystal structure (*Pnma*) of SnSe (Figure 8c). while, the relative presence of Sn and Se confirms the preservation of elemental composition (Figure 8d–f). The collected Raman spectra at different centrifugation speed exhibited four characteristics peaks. Considering that SnSe belongs to *Pnma* (D_{2h}^{16}) symmetry and thus have 12 active Raman modes, the peaks appeared at 70, 105, 127, and 150 cm^{-1}, correspond to the A_g^1, A_g^2, B_{3g}^1, and A_g^2, respectively (Figure 8j). Besides this, the chemical composition (molar ratio of Sn:Se) of exfoliated SnSe was determined to be 1:1. On the contrary, the high-resolution X-ray photoelectron spectroscopy (XPS) spectral investigation revealed Sn core level Sn $3d_{3/2}$and Sn $3d_{5/2}$, while Se shown Se $3d_{3/2}$and Se $3d_{5/2}$ doublets (Figure 8k,l). Accordingly, an electronic grade ultrathin layer of SnSe has not yet been realized.

Most interestingly, it is found that the low boiling point solvents, which have considerably lower surface tension, are suitable for the exfoliation of thin-layer MMCs, particularly SnS and SnSe. The surface energy of such solvents played crucial role to create cavitation during ultrasonication process.

© 2020 The Authors. Published by Wiley-VCH GmbH

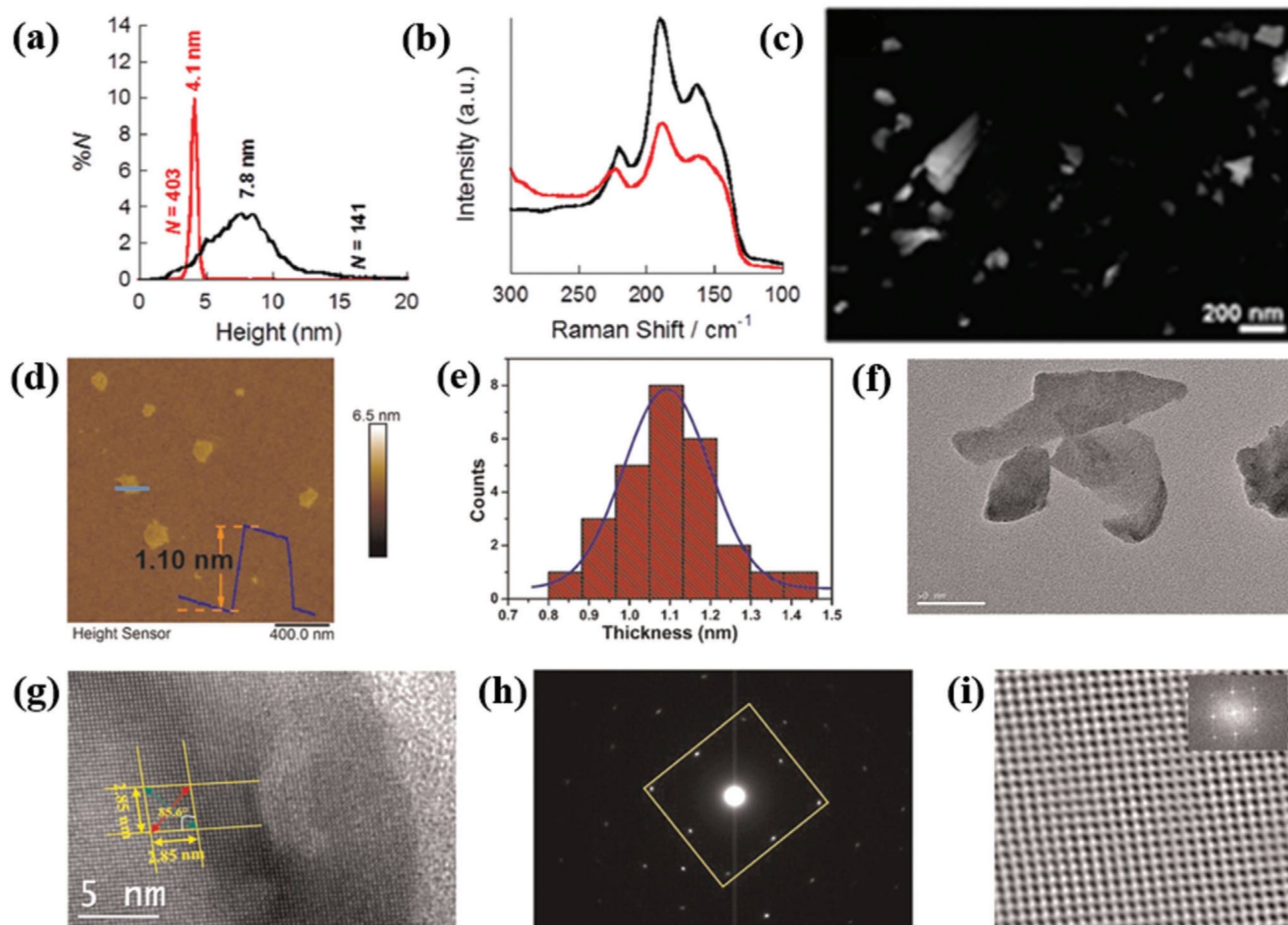

Figure 7. Liquid phase exfoliated SnS nanosheets: a) Particle size distribution for NS height, as determined for SnS sol-A (black curve) and SnS sol-B (red curve); b) Raman scattering spectra of SnS samples; c) low-resolution high-angle annular dark-field (HAADF) scanning transmission electron microscopy (STEM) image of SnS. Reproduced with permission.[34] Copyright 2015, American Chemical Society. As-synthesized ultrathin SnS layers: d) atomic force microscopy image (scale bar: 400 nm); e) histograms of thickness distribution; f) low-resolution TEM image (scale bar: 50 nm); g) HRTEM image (scale bar: 5 nm). The length of lattice fringes (ten fringes) was measured to be 2.85 nm along both different directions. h) SAED pattern. i) Fast Fourier transform (FFT) filtered atomic resolution of the selected area. Inset: FFT pattern of the selected region in HRTEM image. Adapted with permission.[110] Copyright 2020, Author(s), licensed under a Creative Commons Attribution 4.0 License, Nature Publishing Journal.

3.2. Bottom-Up Methods via Vapor Phase Deposition

The vapor phase deposition process is widely used for the synthesis of atomic scale 2D semiconducting layered materials[6,156–158] and is divided into the physical (PVD) and chemical vapor deposition (CVD) methods. In the PVD process, no chemical reactions are taking place. In case of 2D MMC's growth, either a single solid precursor of the final product is used or co-deposition of the chalcogen and transition metal precursors on a substrate takes place. On the other hand, the CVD process employs reactive precursors and high vacuum, in which the precursors react and/or decompose on the surface of the substrate at high temperature to form ultrathin flakes. This process is one of the most effective method to realize large area growth of atomically thin layers of 2D TMDs. Next we summarize the most important reports to synthesize 2D MMCs, such as GeS,[159] GeSe,[68,160] SnS,[70,124,161,162] and SnSe[61,163–165] via vapor phase deposition.

Sutter and co-workers[159] synthesized a few-layer GeS flake via vapor transport. For this purpose, the GeS powder was heated to temperatures in the range of 430–450 °C, while the mica substrate temperature was varied from 320 to 350 °C. The substrate temperature played a significant role on the dimensionality of GeS flakes attained (**Figure 9**a–e). In particular, the use of low substrate temperature led to small-sized NSs (edge length of ≈1.5 µm) (Figure 9f). Flakes of larger size were obtained at a higher substrate temperature of 340 °C (Figure 9g). A bimodal size distribution was particularly observed in that case due to the secondary nucleation of the smaller flakes. The thickness of as-grown GeS varied from 77 to 24 nm (Figure 9h–j). However, the average flake thickness, identified by AFM height was found to be 34.5 nm. The crystal structure and morphology of the flakes were investigated by transmission electron microscopy (TEM). A perfect orthorhombic crystal structure with faceted shapes and clear crystal planes was revealed in GeS (Figure 9l,m). Those

 © 2020 The Authors. Published by Wiley-VCH GmbH

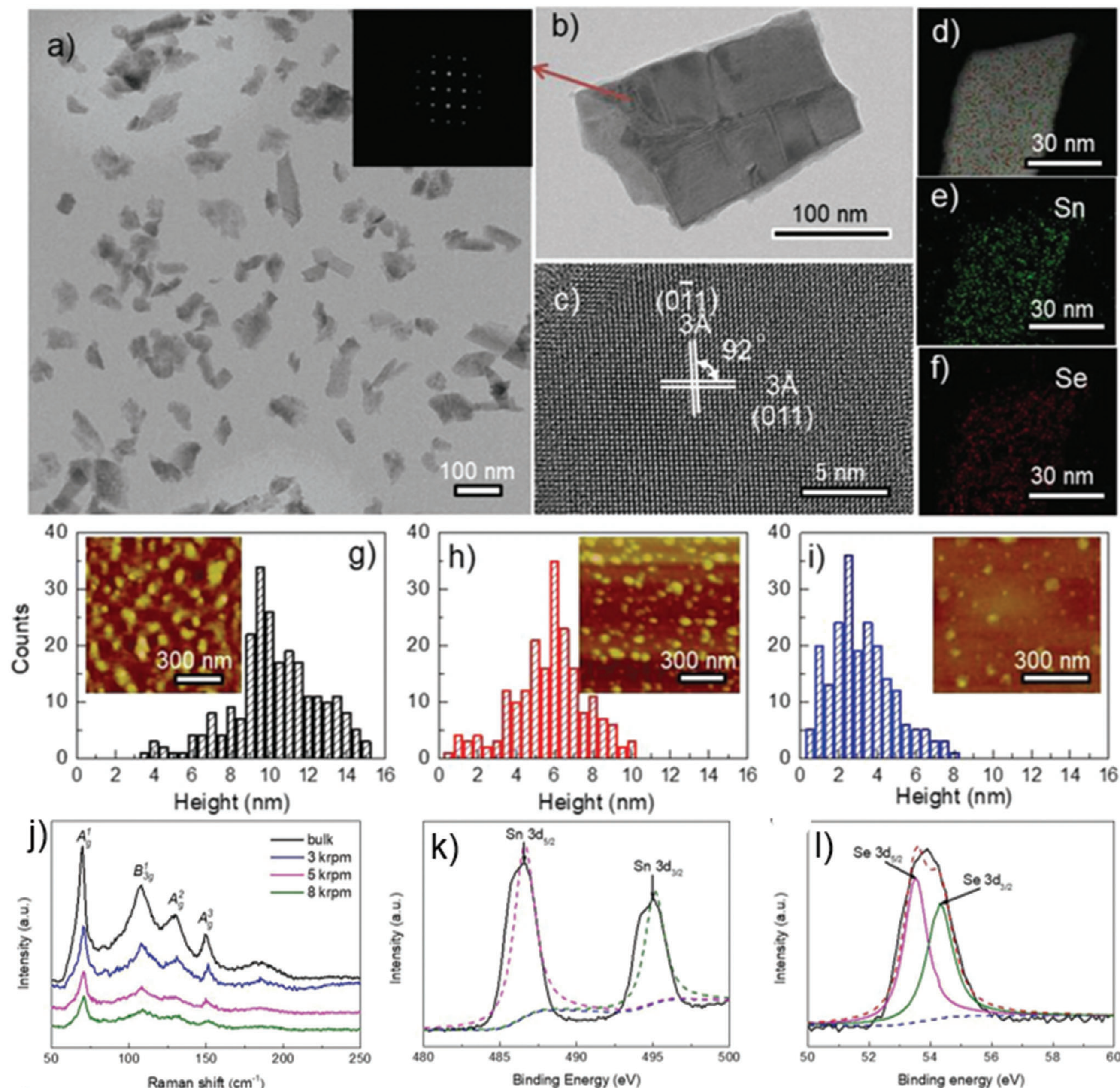

Figure 8. a) TEM image of exfoliated SnSe NSs; b) a single SnSe flake (inset: FFT image of the SnSe NS in (b)); c) HRTEM image of SnSe NSs; d–f) STEM image and the elemental mapping of Sn and Se; g–i) histogram of thickness distribution and inset shows corresponding AFM images of exfoliated SnSe NSs collected at various centrifugation speeds; j) Raman spectra of bulk SnSe and exfoliated NSs; k,l) high-resolution XPS spectra of core level of Sn 3d and Se 3d region. Reproduced with permission.[149] Copyright 2019, Wiley-VCH.

GeS flakes are single-crystalline with orthorhombic space group *Pnma* (Figure 9l–n). The vibrational properties of as-grown GeS flake (340 °C) were investigated by polarized Raman spectroscopy (Figure 9o), showing the characteristic modes of vibrations (A_g and B_{3g}). It is also observed that the intensity of the phonon modes in Raman spectra was changing with incident light polarization.

Mukherjee et al.[68] have reported the growth of high-quality, single-crystalline, micrometer-sized 2D GeSe NSs using a CVD process with various substrate temperatures. A horizontal single-zone tube furnace was used for the synthesis, in which a mixture of Ge and Se powders (1:1 molar ratio) was heated at 480 °C for 4 h under high mTorr vacuum. The dynamical behavior of such CVD process is represented in **Figure 10**a. The process involved the sublimation of bulk GeSe powder (source) into gaseous products and their subsequent transport be the carrier gas (Ar) followed by condensation of the gas molecules onto the substrate, placed at the temperature range 390–430 °C. The constant flow of the

 © 2020 The Authors. Published by Wiley-VCH GmbH

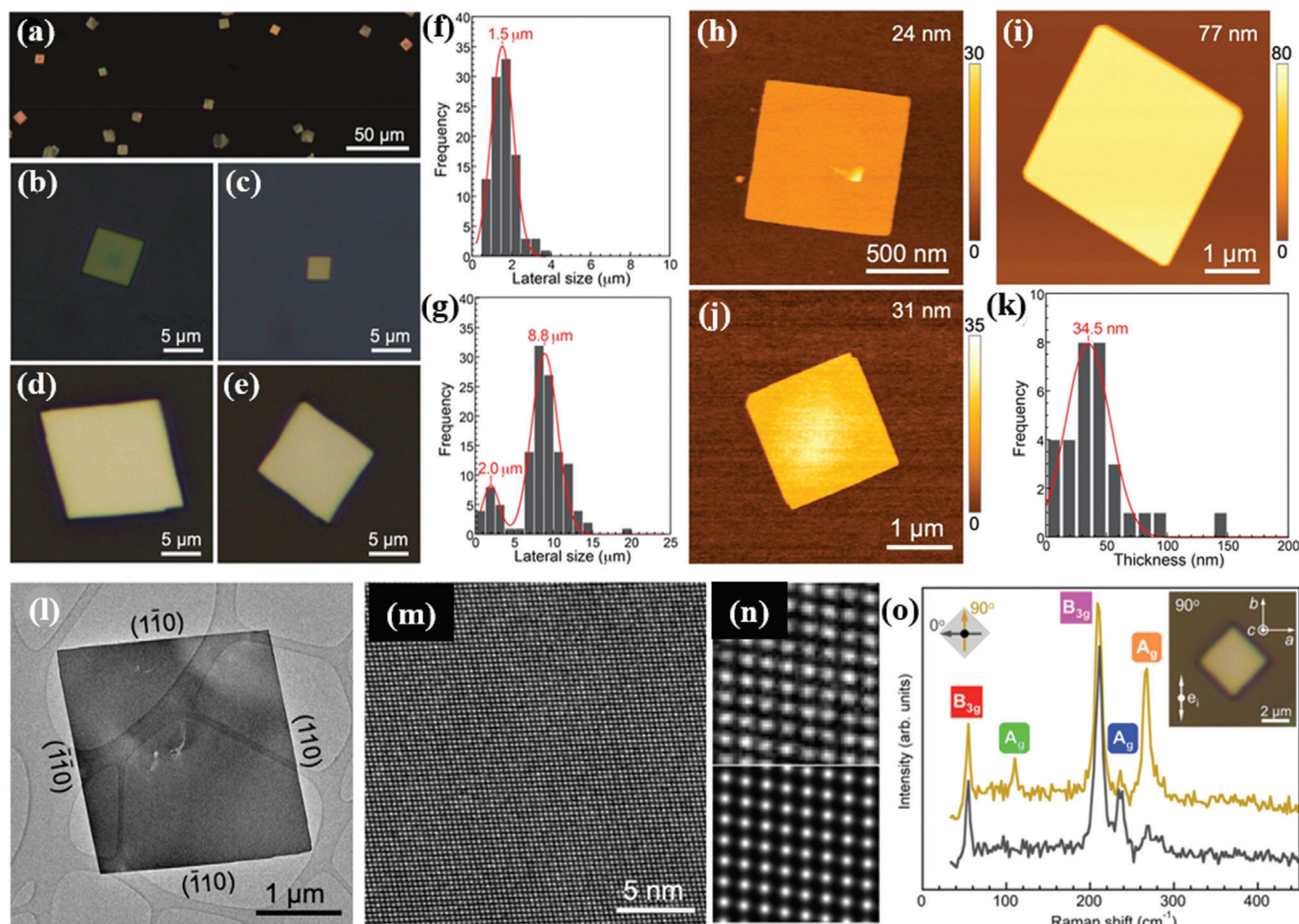

Figure 9. a) Optical image of as-grown GeS flakes on mica substrate. b–e) Higher magnification optical images. Flake size distribution obtained by growth: f) monomodal at 320 °C and g) bimodal at 340 °C (growth time: 10 min). h–j) AFM topography image of GeS flakes with different thickness. k) Thickness distribution of GeS flakes grown at 340 °C for 10 min. l,m) TEM images of low and high-resolution SnS flakes. n) Higher magnification view of (m) (top), and multislice image simulation (bottom). o) Anisotropic Raman spectra of synthesized GeS flake (thickness ≈ 500 nm) obtained with 0° and 90° orientations of the incident laser light linear polarization. Laser excitation wavelength was 532 nm with 16.8 μW laser incident power. Inset: an optical image of the measured flake and the direction of the incident electric field vector. Reproduced with permission.[159] Copyright 2019, American Chemical Society.

sublimated gas molecules and their subsequent adsorption and recrystallization to growth sites assisted the growth of the nanostructures. The obtained nanostructures were found to exhibit different morphologies (Figure 10b–d), depending on the substrate temperate (zones 1, 2, 3). The growth of different crystalline nanostructures strongly depends on the concentration gradient of GeSe vapor at the lower temperature zone (zone 3, large distance from the source). The typical lateral and longitudinal dimension of the NSs are measured to be in the range of 4–160 μm and 60–140 nm, respectively (Figure 10e,f).

Furthermore, Hu et al.[166] have reported a high quality single-crystalline ultrathin layer of 2D GeSe flakes, which are synthesized by a salt-assisted CVD method (Figure 10g,h). In this process, mixed $GeSe_2$ and KCl powder was heated to 550 °C for 0.5 h. During the heating process a mixed gas of H_2 and Ar was passed through the quartz tube used in the process. The $GeSe_2$ was easily reduced to GeSe with H_2 ($GeSe_2 + H_2 \rightarrow GeSe + H_2Se$); in this reaction the salt KCl used played an assisting role. It was observed that the as-grown thinnest GeSe flakes on mica substrates were ≈5 nm (Figure 10i), corresponding to eight monolayers. The Raman spectra of GeSe flakes with different thickness (5, 9, and 15 nm) exhibited four characteristic modes of vibration, A_g^1, B_{3g}, A_g^2, and A_g^3, respectively (Figure 10j), peaked at 81.8, 151.9, 173.5, and 189.2 cm^{-1} for a 15 nm-thick flake. These Raman modes blueshifted upon increasing the layer number. Such blueshift can be attributed to the strong interlayer coupling in thicker GeSe NSs. Similar shifts were observed in many 2D materials, including graphene, MoS_2, and GaSe.[166–169]

Moreover, the synthesized GeSe flakes are highly uniform and homogeneous, which is reflected in respective Raman mapping of B_{3g} mode (Figure 10k). In addition, a sequence of polarization-resolved Raman spectra for A_g and B_{3g} modes has been recorded, showing that the angular dependence on crystallographic directions of the NSs is identical to that of mechanically exfoliated GeSe flakes.[102]

 © 2020 The Authors. Published by Wiley-VCH GmbH

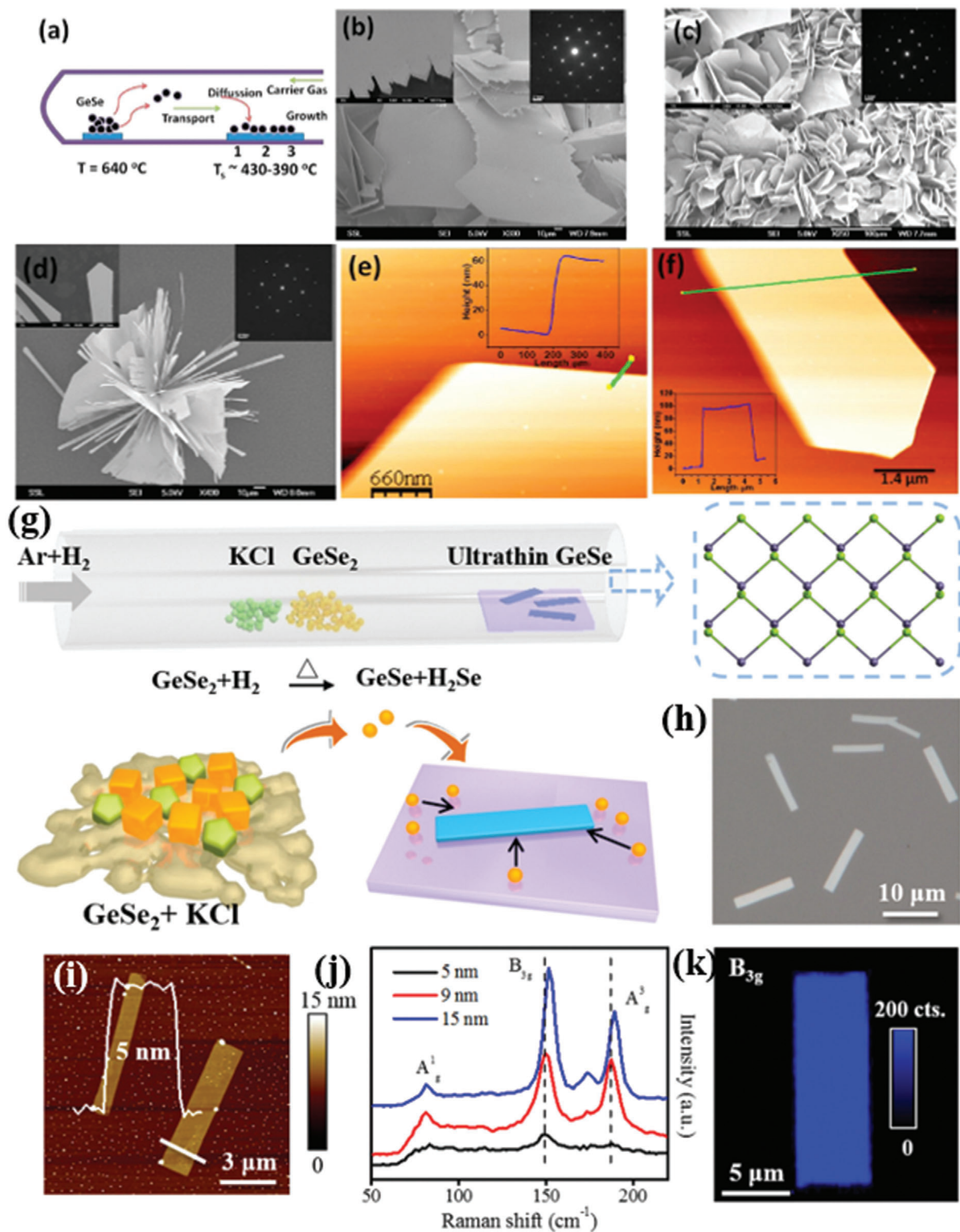

Figure 10. a) Schematic CVD synthetic process. b–d) Scanning electron microscopic (SEM) images of CVD grown GeSe flakes on the areas indicated by 1, 2, and 3 in (a), respectively (insets: top right corners of (b)–(d) are SAED patterns for representative flakes). The insets panel at the left corners of (b)–(d) are the magnified SEM images. e,f) AFM images of GeSe flakes and corresponding height profile (inset in (e) and (f)) of the flakes (the solid line in (e) and (f)). Reproduced with permission.[68] Copyright 2013, American Chemical Society. g) Schematic representation of the salt-assisted CVD with atomic structure of the layered GeSe. h) Optical image of as-grown GeSe flakes. i) AFM image of GeSe flakes with height profile. j) Raman spectra of GeSe flakes. k) Raman mapping (B_{3g} mode) of GeSe flake. Reproduced with permission.[166] Copyright 2019, American Chemical Society.

© 2020 The Authors. Published by Wiley-VCH GmbH

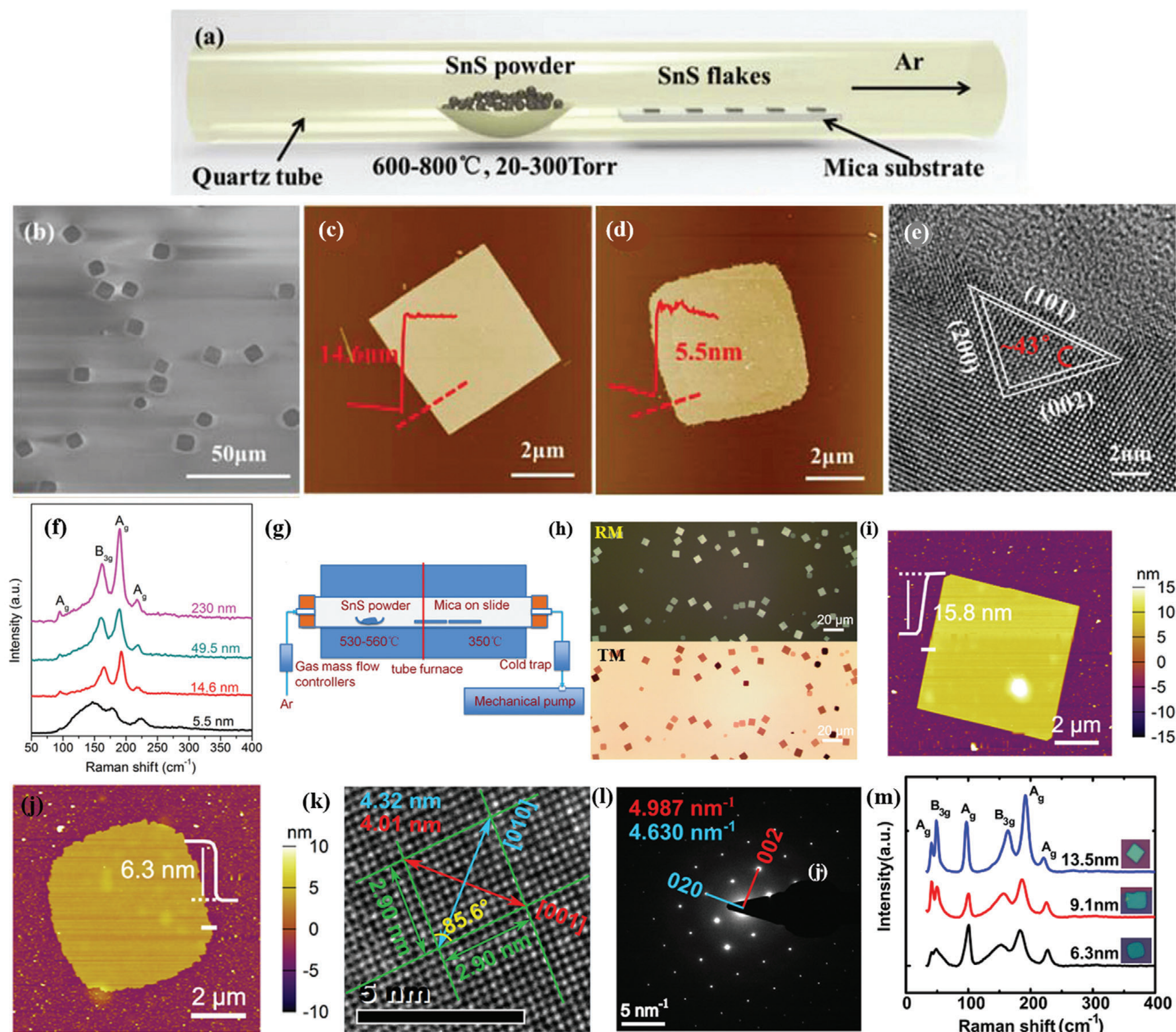

Figure 11. a) Schematic of PVD growth for anisotropic SnS flakes; b) SEM image of the anisotropic SnS flakes synthesized at 600 °C. c,d) AFM images and height profile of anisotropic SnS flakes. e) HRTEM image of the SnS flake; f) Raman spectra of the SnS flakes with different thicknesses. Reproduced with permission.[70] Copyright 2016, Royal Society Chemistry. g) Schematic representation of the PVD growth system; characterization of synthesized 2D SnS nanoplates. h) Optical microscopy images on mica substrates (RM and TM correspond to reflection transmission mode of microscopy). i,j) AFM images with height profile. k) High-resolution TEM image. l) SAED pattern corresponding to the flake shown in (k). m) Raman spectra of SnS nanoplate with different thickness. The corresponding optical microscopic images are shown in the inset. Reproduced with permission.[172] Copyright 2017, American Chemical Society.

PVD synthesis of orthorhombic SnS has been reported by Meng and co-workers.[70] The authors investigated the effects of growth temperature and pressure. During synthesis bulk SnS powder was evaporated into a horizontal single zone tube furnace, upon heating at 600–800 °C for 10 min at a pressure around 20–300 Torr (**Figure 11**a). Mica sheets were used as substrates, which were placed downstream to the tube center at a distance of ≈8–20 cm from the evaporation area. A natural cooling process was employed to cool down the system. Throughout the experiment, Ar was used as a carrier gas with a constant flow rate. The synthesized SnS flakes on mica substrates exhibit quasi-rhombic shapes with a lateral size in the range from hundreds of nanometers to few µm (Figure 11b,c). However, the random nucleation of SnS resulted in a spatial nonuniformity of the grown flakes (Figure 11c,d). The thinner NSs showed relatively rough surfaces and edges than the thicker ones, which signified the incomplete crystal growth of SnS flakes. They further confirmed that the growth temperature and pressure significantly affect the domain size and grain boundary edge structure of synthesized 2D materials.[170,171] High-resolution TEM images (Figure 11e) of the synthesized SnS showed a perfect rhombus lattice with fringe spacings of ≈0.29, ≈0.4, and ≈0.43 nm, corresponding to the

© 2020 The Authors. Published by Wiley-VCH GmbH

interplanar spacings of the (101), (002), and (200) planes of the orthorhombic SnS, respectively. The corner angle is measured to be 43°, which agreed well with the theoretical value. The vibrational properties of synthesized 2D SnS flakes with different thickness were monitored, showing that the SnS flakes exhibited four characteristic phonon modes, i.e., three A_g and one B_{3g}, peaked at 95.5, 190.7, 216.8, and 162.5 cm^{-1}, respectively. It was identified that the Raman intensity and peaks deviate from the peak positions of A_g and B_{3g} upon lowering the vertical dimensionality. The strange spectral behavior in Raman spectrum (Figure 11f) of the thinnest NS (5.5 nm) was due to poor crystallinity (Figure 11d).

In another work, Tian et al.[172] have reported the synthesis of layered anisotropic 2D SnS via PVD. A lower sublimation temperature was adopted to evaporate the bulk SnS powder. In their typical synthesis, a two-zone tube furnace was used (Figure 11g). For the synthesis, the bulk SnS powder was heated at 530–560 °C, while a high purity Ar gas was used to carry the SnS vapor and deposit it onto mica substrates (Figure 11h). The obtained NSs exhibited the orthorhombic crystal structure, lateral dimensions of 5–15 µm, and minimum thickness of 6.3 nm (Figure 11i,j). TEM analysis showed perfect rhombus lattice fringes (Figure 11k,l) with *d* spacings of 2.90, 2.90, 4.32, and 4.01 nm, corresponding to [011], [01$\bar{1}$], [010], and [001] directions, respectively. Moreover, the measured corner angle (85°), between the [011] and [01$\bar{1}$] planes, well agreed with the theoretical predictions.[173,174] While, the perfect rhombus lattice fringes in SAED pattern further confirmed the single crystallinity of the NSs. Finally, the NSs exhibited the typical characteristic A_g and B_{3g} Raman modes (Figure 11m), with the thicker NSs to show stronger and sharper Raman modes compared to the thinner counterparts. This confirmed the better crystalline quality of the thicker NSs, which was consistent with the edge morphology obtained from AFM images.

The synthesis of few-layer 2D SnSe via PVD has been reported by various groups.[61] Zhao et al.[163] have realized the synthesis of single-crystal SnSe NSs on mica substrates in a controlled manner. A 15.8 nm thick SnSe NS having orthogonal lattice fringes with well-defined lattice spacings (0.30 nm) and intersect angle (92°) of the crystal planes was identified, which further confirmed the orthorhombic SnSe crystal structures.[126,175] In PVD method, the temperature mainly controls the evaporation quantity of bulk SnSe, while the pressure affects the nucleation and growth process. With the evaporation temperature and pressure fixed at 500 °C and 70 Torr, the deposition temperature was varied (from 340 to 390 °C), and as a result controlled synthesis of SnSe NSs was achieved.[176] A few years ago, Xu et al.[164] have followed a synthesis process similar to that reported by Zhao et al.,[163] however the sublimation and the deposition temperatures were kept higher. In particular, the sublimation, deposition temperature of SnSe, and argon flow rate was set at 650 °C (in 17 min), 350–450 °C, and 200 standard cubic centimeters per minute (sccm). Following this process, SnSe NSs with a uniform surface were grown. However, a distribution of thickness (10–210 nm) was found (Figure 12a,b), which can be controlled through the growth conditions. Interestingly, the rectangular NSs showed clear orthogonal lattice fringes with two similar lattice spacings of 0.30 nm. The measured angle (94°) between two crystallographic planes is well matched with the orthorhombic SnSe crystal structure.[175,177] The observed orthogonal structure together with the orthogonal symmetry (Figure 12c) confirmed the single-crystal nature of the synthesized SnSe NSs. However, the corner angle was obtained to be 94°, which differ from that of other reports.[163] In fact, this discrepancy originates from the impact of different value of structural anisotropy (along armchair and zigzag direction) during the growth.

Owing to the phase transition occurred during CVD growth the substrate temperature critically affects the stoichiometry in SnSe (i.e., the Sn:Se ratio).[178–180] Recently, Wang and Pang[178] used a proper proportion of SnO_2 and Se precursors to synthesize 2D SnSe or $SnSe_2$ NSs with lateral sizes of few micrometers. Specifically, the Sn:Se stoichiometry was varied by changing the weight of Se from 50 to 500 mg. It was revealed that the shape of as-grown sample switches from square to truncated triangle (Figure 12d,e). As a consequence, the phase controlled growth of 2D tin selenides is possible by adjusting the nominal Sn:Se ratio. The AFM height analysis of SnSe NSs revealed a quite flat top surface and thickness of 59.8 and 95.1 nm (Figure 12e). On the other hand, the obtained thickness of the different shape $SnSe_2$ flakes grown were ≈67.7 and ≈20.8 nm, respectively. In order to shed light on the CVD process, a simple growth mechanism was discussed.

In particular, when the bulk SnO_2 powders are heated to react with Se vapor, the reaction forms SnSe or $SnSe_2$ via the following reaction paths

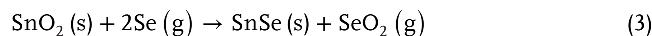

$$SnO_2\,(s) + 2Se\,(g) \rightarrow SnSe\,(s) + SeO_2\,(g) \tag{3}$$

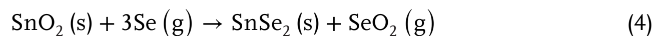

$$SnO_2\,(s) + 3Se\,(g) \rightarrow SnSe_2\,(s) + SeO_2\,(g) \tag{4}$$

When the amount of Se is low, the first chemical reaction takes place giving rise to the formation of SnSe. On the other hand, upon increasing the weight of Se precursor, the second chemical reaction is dominant and $SnSe_2$ NSs are formed.

Very recently, Khan et al.[181] have introduced a novel bottom-up synthesis method to obtain SnS monolayers. In particular, a molten droplet of Sn was exposed to an anoxic atmosphere containing a sulfur source at 350 °C. As a result, the surface forms a sulfide skin in a self-limiting Cabrera–Mott reaction. Then liquid metals are employed to exfoliate ultrathin SnS sheets and to transfer them onto the desired substrates. Using this method, SnS nanosheets with large lateral dimensions can be attained, with a highly crystalline orthorhombic structure (Figure 12f,g). The ultrathin SnS layer thickness obtained was measured to be 0.7 nm (Figure 12h), which was further confirmed by Raman spectroscopy (Figure 12i). The characteristic features agreed well with the phonon mode in a thin-layer SnS. This synthesis method may be suitable for the isolation of the MMCs single layer.

Another bottom-up approach is the WCS method. This method comprises hot injection, one-pot synthesis, hydrothermal intercalation, and sequential deposition.[4,61,126,182,183] As a fast and low-cost method for producing nanomaterials for large-scale industrial application, the WCS of MMCs nanosheets has drawn attention recently to produce SnS, SnSe, GeS and GeSe nanosheets.[150,184] In a typical wet synthesis of colloidal MMC nanosheets using the hot injection method, the group IV elements, such as $SnCl_2$, $SnCl_4$, and Ge_4, are used as an inorganic halide metal source.[150,184] On the other hand, organic materials,

 © 2020 The Authors. Published by Wiley-VCH GmbH

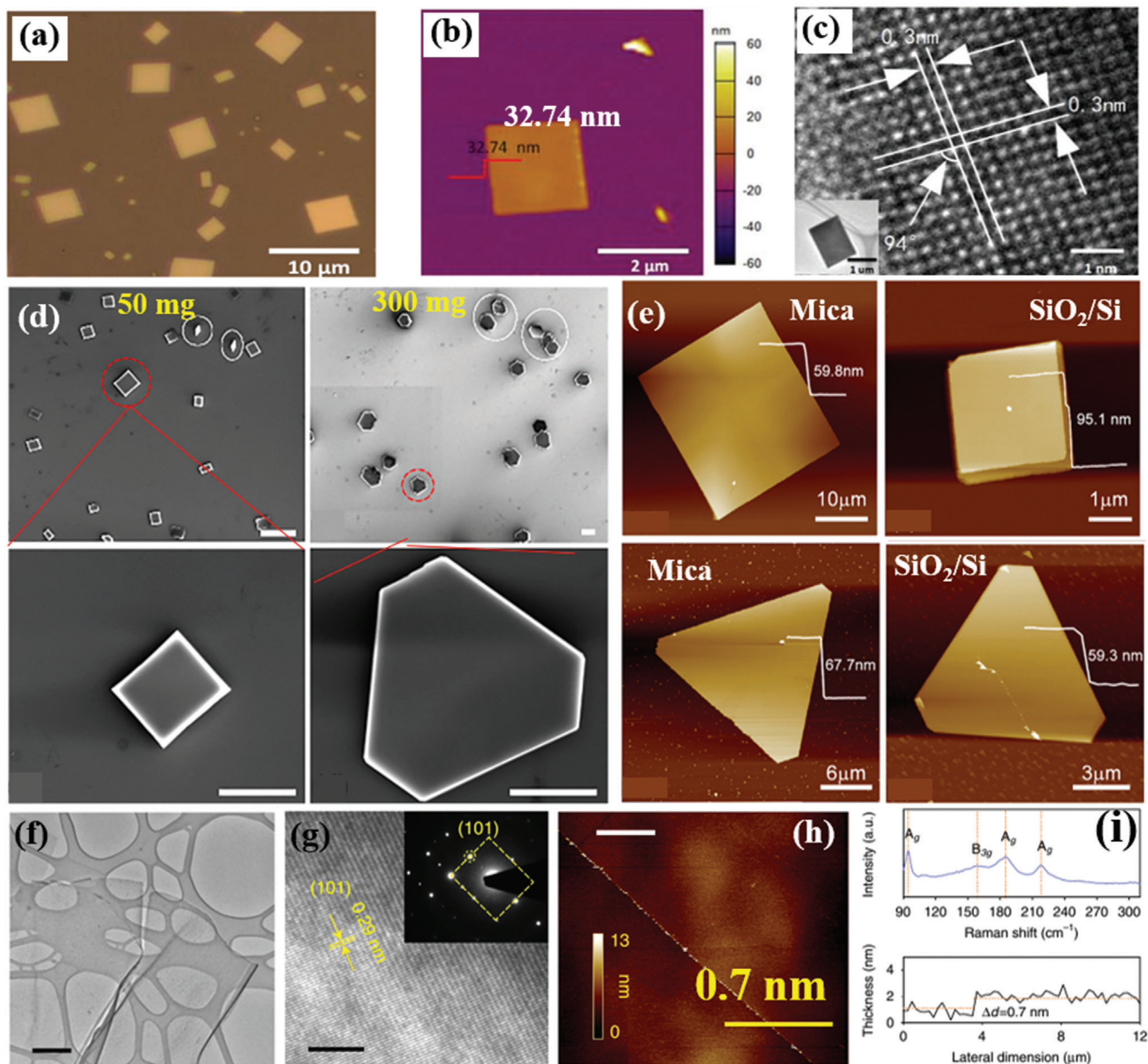

Figure 12. a) Optical image of SnSe NS on mica substrates (lateral size distribution of 2 to 8 µm). b) AFM image with height profile (inset solid line, height 32.74 nm). c) HRTEM image of a NS (scale bar is 1 nm); a low-magnification TEM image is shown in the inset. Reproduced with permission.[164] Copyright 2017, American Chemical Society. d) SEM images of as-grown flakes on SiO_2/Si substrates with 50 and 300 mg Se powders (scale bar: 20 µm (top panel) and 10 µm (bottom panel). e) AFM images of as-grown and of different shape flakes on mica and SiO_2/Si. Reproduced with permission.[178] Copyright 2018, Elsevier. f) TEM image of SnS monolayer synthesized using a liquid metal exfoliation method. Scale bar is 500 nm. g) HRTEM fringe pattern. Inset: SAED pattern. Scale bar is 5 nm. h) AFM image of the SnS monolayer, and i) Raman spectrum and AFM height profile of the SnS monolayer. Scale bar 8 µm. Reproduced with permission.[181] Copyright 2020, Author(s), licensed under a Creative Commons Attribution 4.0 License, Nature Publishing Group.

such as dodecanethiol, trioctylphosphine selenide (TOP-Se), and thioacetamide, are used as group VI elements. Both reactants are mixed together with organic solvents and heated up to the reaction temperature. Subsequently, the obtained products are redispersed into an organic solvent and centrifuged to isolate the required nanosheets. In 2013, Li et al.[184] have adopted one-pot synthesis as a WCS method to synthesize ≈300 nm wide and 2 ML (≈1 nm) thick SnSe nanosheets. In another report, Schaak and co-workers[150] have adopted one-pot synthesis method to prepare GeS and GeSe nanosheets. The obtained GeS nanosheets were 5 nm thick with (2–4) µm times (0.5–1) µm average lateral dimensions. For GeSe a larger range of thicknesses was achieved (5–100 nm). Apart from the aforementioned approaches, much larger MMC flakes have been synthesized via WCS.[182,183]

Table 5 summarizes the comparison of the various synthesis methods applied for the synthesis of MMC flakes. In general,

Table 5. Comparison of the typical methods used for the synthesis of MMCs nanosheets.

Method	Brief description of the synthesis method	Materials	Lateral dimension	Vertical dimension	Advantages	Limitations	References
Mechanical exfoliation	Scotch tape is used to peel off thin layer from bulk crystal. Gold tape, polymer matrix is used to transfer thin layer on required substrates.	GeS	Few tens of nm	8 nm	Simplicity, high crystal quality, low defects	Low exfoliation yield, repeatability in size, reproducibility in layer number, and the large-area uniform flake	[107]
		GeSe	Tens of µm	33 nm			[101]
		SnS	Several µm	4.3 nm			[57]
		SnSe	Tens of µm	90 nm			[105]
Liquid phase exfoliation	Bulk crystals or powders are dispersed in a suitable solvent and are subjected to ultrasonication for a certain amount of time. Suspension is centrifuged to isolate the ultrathinlayer of nanosheets (NSs).	GeS	–	1.3 ± 0.1	Solution-processed, large-scale bulk production, high yield, low cost, simplicity	Thickness control, relatively smaller lateral dimension, proper choice of solvent	[143]
		GeSe	50–200 nm	2			[141]
		SnS	170 nm	1.11 nm			[110]
		SnSe	150 nm	2–10 nm			[149]
Chemical vapor deposition	One of the reliable method to produce 2D material for electronics. The CVD process employs reactive precursors and high vacuum, in which the precursors react and/or decompose on the surface of the substrate at high temperature to form ultrathin flakes.	GeS	1.5–20 µm	10 nm	Large scale lateral size, precise controllable Thickness and lateral dimension, less defects	High temperature, ambient environment, high vacuum, Relatively complicated recopies, costly	[159]
		GeSe	Few µm	5 nm			[166]
		SnS	Few µm	5.5 nm			[70]
		SnSe	1–6 µm	6–40 nm			[163]
Wet chemical synthesis	Chemical method, surfactants or polymers assisted direct synthesis process	GeS	2–4 µm	5 nm	Solution processability, high production yield	Defects, surfactants on the surface	[150]
		GeSe	–	5–100 nm			[150]
		SnS	8 µm	7 nm			[182]
		SnSe	300 nm	1 nm			[184]

there is currently no method that can produce high crystal quality and ultrathin (down to monolayer) coupled with high-lateral-dimension nanosheets. For example, the mechanical exfoliation and CVD/PVD techniques can produce as large as few µm to tens of µm in lateral dimensions MMCs, while it is difficult to isolate nanosheet thicknesses below 4 nm. On the other hand, the LPE and WCS methods can produce ultrathin, even monolayer flakes, however, the lateral dimension is very small and thus not favorable for optical and electronic properties investigations. Besides this, mechanically and LP exfoliated MMCs exhibit high crystal quality, contrary to the CVD/PVD grown ones.[172] This is primarily due to the strong interlayer coupling energy (armchair/zigzag)

 © 2020 The Authors. Published by Wiley-VCH GmbH

in MMCs, which restricts the isolation of a single layer with high crystallinity. In this context, there are a few possible ways to overcome the different limitations. As far as the ME and PVD/CVD techniques, by proper choice of the deposition substrate and optimized protocols, one could make the lateral growth stronger than the vertical one, and as a result thinner and larger flakes can be attained. On the other hand, the postetching of mechanically exfoliated MMC flakes via chemical routes and/or laser processing can overcome the thickness limitation and give rise to large-area monolayer flakes.

4. Applications: Theory and Experiment Prospect

Since the isolation of single-layer graphene a new era of 2D electronics has begun. The semimetallic nature with gapless band structure of graphene imposes important limitations in electronic, optoelectronic, and photonic applications. However, 2D MMCs exhibit a wide range of direct or indirect bandgaps. More important, MMCs are highly anisotropic in nature, as they exhibit in-plane structural anisotropy along the armchair and zigzag crystalline directions. Such structural anisotropy is revealed in electronic, optoelectronic, and photonic response. In the following, we will present an overview of the very recent advances in electronic, optoelectronic, and photonic applications of MMCs, giving emphasis in VP and SHG.

4.1. Electronic Devices Exhibiting Anisotropic Response

In-plane anisotropy found in a layered BP open up a new horizon in 2D MMCs research for emerging nanophotonic and optoelectronic device applications.[19,185] Following such first studies, in-plane phosphorene-analogous group IV–VI MMCs have received significant interest due to their anisotropic optical and electronic response.[100,103,113,117,186] In wavy structured MXs, the effective mass, dielectric constant, and refractive index are entirely different along armchair compared to zigzag direction. Stereochemically active lone pair electrons in 5s (e.g., Sn) or 4s (e.g., Ge) and different electronegativity in chalcogens (e.g., S or Se) play a crucial role in such anisotropy. This interesting feature critically affects the exotic optical and electronic behavior of such materials, therefore adds a new dimension to their optoelectronic properties and stimulates the development of angle-resolved photonics and optoelectronics.[129] Accordingly, understanding the effect of electrical and optoelectrical anisotropy in MMCs has evolved rapidly in the recent years.

Several groups had investigated the electrical anisotropy in few-layer GeS NSs.[100,187] Matsuda and co-workers,[187] in particular, introduced a highly polarization sensitive and broadband photodetector (**Figure 13**a), based on multilayer germanium sulfide (GeS). A 45 nm GeS flake was used to fabricate a field effect transistor (FET) device. Photoresponse was controlled via tuning of the gate bias voltage (V_g) and the light intensity. The transfer characteristics (V_g–I) of FET device exhibited a p-type behavior (Figure 13b), and the obtained carrier mobility was measured to be 1.6×10^{-3} cm^2 V^{-1} s^{-1}. A high on/off current ratio ($>10^4$) was also recorded at ±40 V. Moreover, current hysteresis appeared in the voltage sweeping, in which trap/defect states play a dominant role. The anisotropic crystal structure of GeS, causing its strong linear dichroism,[107] was investigated through measuring of the photoresponse of the GeS photodetector with highly polarized light. It is found that the measured photocurrent (at $\lambda \approx 750$ nm) strongly depends on the polarization angle (θ) of incident light (Figure 13c). The photocurrent sensitivity (polar plot of Figure 13d) reaches its maximum value at 0° and its minimum at 90° polarization, corresponding to armchair and zigzag directions, respectively. This strong electrical anisotropy is perfectly consistent with the anisotropy in optical absorption. As a consequence, a GeS-based linear dichroic photodetector was demonstrated with a dichroic ratio of 1.45. In another study, Li et al.[100] presented a photodetector fabricated using a GeS NS with a thickness of 28.7 nm (Figure 13e,f). It is shown that the angle-resolved photocurrent (Figure 13g) presented in a polar plot changed dramatically with incident light.

Hu and co-workers[113] first reported on the anisotropy in optical and electrical behavior of CVD-grown few-layered GeSe. Following this study, Zhai and co-workers[188] reported on back-gated FETs from mechanically exfoliated GeSe NSs of 40 nm thickness. The characteristic I–V curves were linear (Figure 13h,i), indicating an Ohmic contact between the electrodes and the GeSe NSs. Besides this, the transfer characteristics exhibited a p-type semiconducting behavior (Figure 13j,k). A high on/off ratio ($\approx 10^3$) and hole (0.8 cm^2 V^{-1} s^{-1}) mobility at room temperature were measured, which are comparable with other metal dichalcogenides such as SnS_2 and $SnSe_2$.[189–191] Furthermore, the photoresponsive behavior of the fabricated FET exhibited a deviation from the linear relationship (**Figure 14**a,b) under illumination (532 nm intensity of 0.42 mW cm^{-2}). It is shown that a Schottky emission charge carrier transport mechanism takes place due to the large density of photoinduced charge carriers under illumination (Figure 14c). This phototransistor exhibited excellent stability in both photoresponse and decay rate. An anisotropic optoelectronic behavior was also investigated on such phototransistors (Figure 14d–f). In particular, the normalized photocurrent demonstrated three periodic peaks at 0°, 180°, and 360° with two valleys at 0° and 270°, while a strong polarization-sensitive photodetection with peak-to-valley ratio ≈1.3 was obtained. A strong electrical anisotropy was also measured in a multiterminal FET device in which the electrodes are placed at an angle of 45°. Moreover, significant impact of anisotropy in angle-resolved hole mobilities at different temperatures was recorded (Figure 14f). Indeed, the calculated hole mobility along armchair and zigzag direction is ≈6.03 and ≈3.25 cm^2 V^{-1} s^{-1}. It is observed that the effective mass, m, played a crucial role to the mobility (μ), as $\mu \alpha \frac{1}{m}$. Based on theoretical calculations, the respective masses are $m_{armchair} = 0.16m_0$ and $m_{zigzag} = 0.33m_0$, where, m_0 is the free electron mass.[172,192] Notably, the theoretically calculated mobility ratio ($\mu_{armchair}/\mu_{zigzag}$) is well matched with the experimental value. This ratio was shown to increase from 1.85 to 3.15 upon decreasing the temperature from 300 to 60 K (Figure 14g). Such anisotropy in μ along armchair and zigzag direction pave a new root to employ GeSe for novel optoelectronics applications. In addition, Liu et al.[193] have also investigated similar anisotropic electronic properties in GeSe devices. Figure 14h presents the schematic diagram of the angle-resolved transport setup they used for electrical anisotropy measurements. The typical I–V characteristics exhibited a linear relationship in dark condition, while the current significantly increased under laser

© 2020 The Authors. Published by Wiley-VCH GmbH

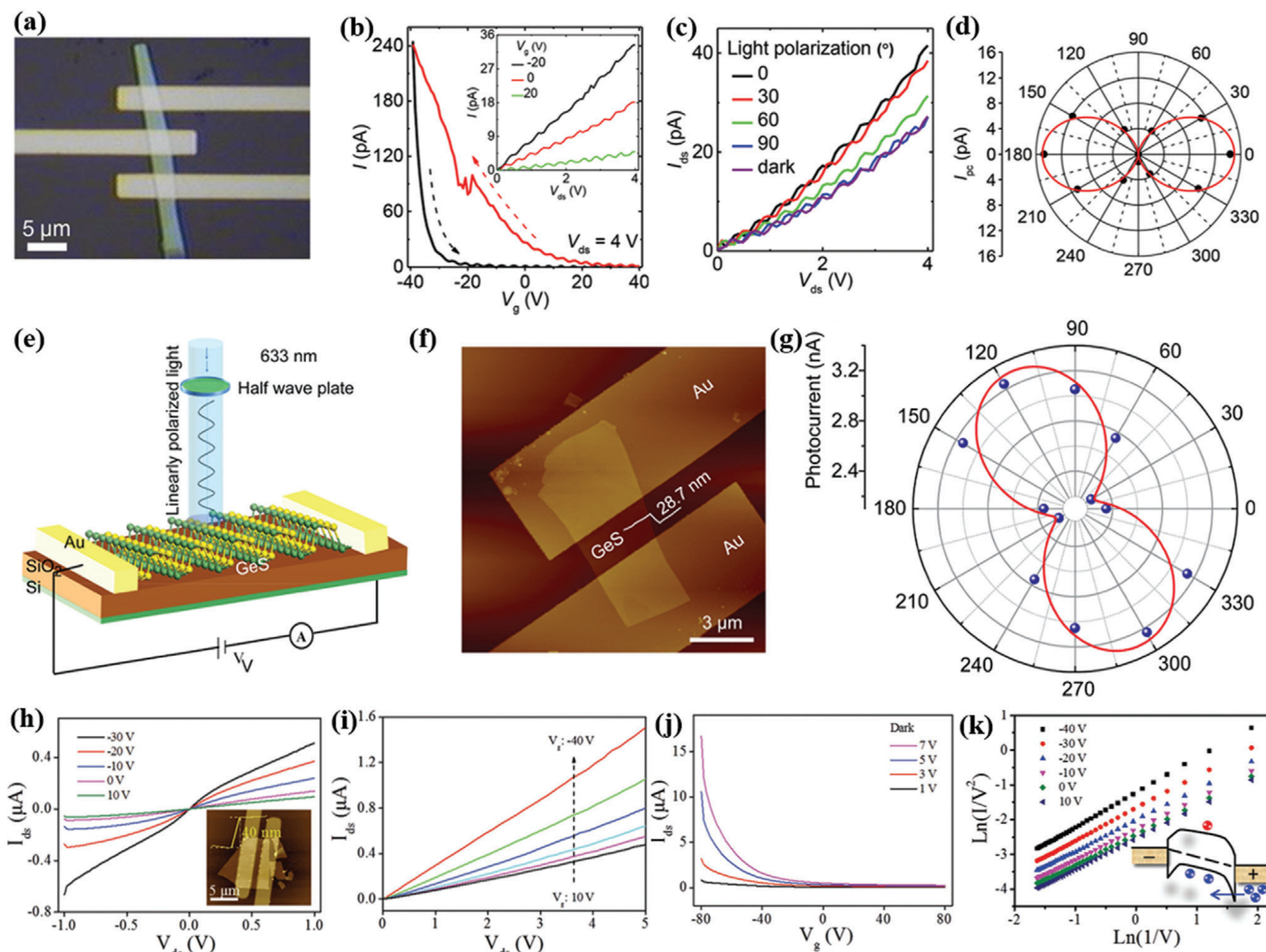

Figure 13. a) Optical image of fabricated GeS photodetector (45 nm thick GeS); b) gate bias voltage dependent transfer characteristics. Sweeping direction (black and red dotted arrow) indicating the forward and reverse voltage scans, respectively (−40 to +40 V and +40 to −40 V). The inset shows V_{ds}–I characteristics at various back-gate voltages. c) Incident light (λ = 750 nm) polarization dependent I_{ds}–V_{ds} characteristics of a GeS FET device (P = 32 µW cm^{-2}). d) Polar plots of photocurrent. The angle θ is the polarization direction of the incident light relative to the armchair direction. The solid red curve represents the cos2θ function. a–d) Reproduced with permission.[187] Copyright 2017, Royal Society of Chemistry. e) Schematic diagram of a GeS phototransistor. f) AFM image of the device (scale bar: 3 µm). and g) polar plot of photocurrent as a function of the polarization angle. e–g) Reproduced with permission.[100] Copyright 2019, American Chemical Society. h) The I_{ds}–V_{ds} characteristics of a GeSe transistor at different gate voltages. The AFM image of the device and height profile is shown in the inset (thickness and scale bar: 40 nm and 5 µm, respectively). i) Device characteristic curves at different gate bias voltages. j) Transfer characteristics of the device. k) Direct tunneling plots at different gate voltages. The inset shows an illustration of carrier tunneling. Reproduced with permission.[188] Copyright 2018, Wiley-VCH.

illumination. A significant photoresponsivity (7.05 A W^{-1}) and specific detectivity (3.04 × 10^{8} Jones) were recorded, which is the highest value among recent reports. Furthermore, high photocurrent sensitivity to polarization angle was observed (Figure 14i), namely, a significant increase in photocurrent (55%) upon using a 90° polarization angle (Figure 14j). Moreover, the polarized photocurrent showed a correlation with the phonon scattering in zigzag direction, namely, when the incident light is parallel to the zigzag direction the LO phonons get excited, while the TO phonon get excited when it is parallel. The LO phonons, in particular, exhibited relatively large scattering cross sections to the charge carriers. The potential anisotropy in the electrical behavior of SnS NSs was investigated by Xue and co-workers.[172] For this purpose, PVD-grown SnS nanoplatelets were used to fabricate FET devices. The anisotropy in electrical transport was investigated on devices with cross-Hall-bar structure (**Figure 15**a). The temperature-dependent transfer characteristics of the fabricated FET devices along zigzag and armchair directions were subsequently recorded. The hole mobility of the devices was calculated using the following equation

$$\mu = \frac{L}{W}\ \frac{\mathrm{d}G}{C_g \mathrm{d}V_g} = \frac{\mathrm{d}\sigma}{C_g \mathrm{d}V_g} \qquad (5)$$

where, L and W are the length and width of the channel, G is the conductance, C_g is the gate capacitance per unit area, and σ is the conductivity along armchair or zigzag direction (Figure 15b).

© 2020 The Authors. Published by Wiley-VCH GmbH

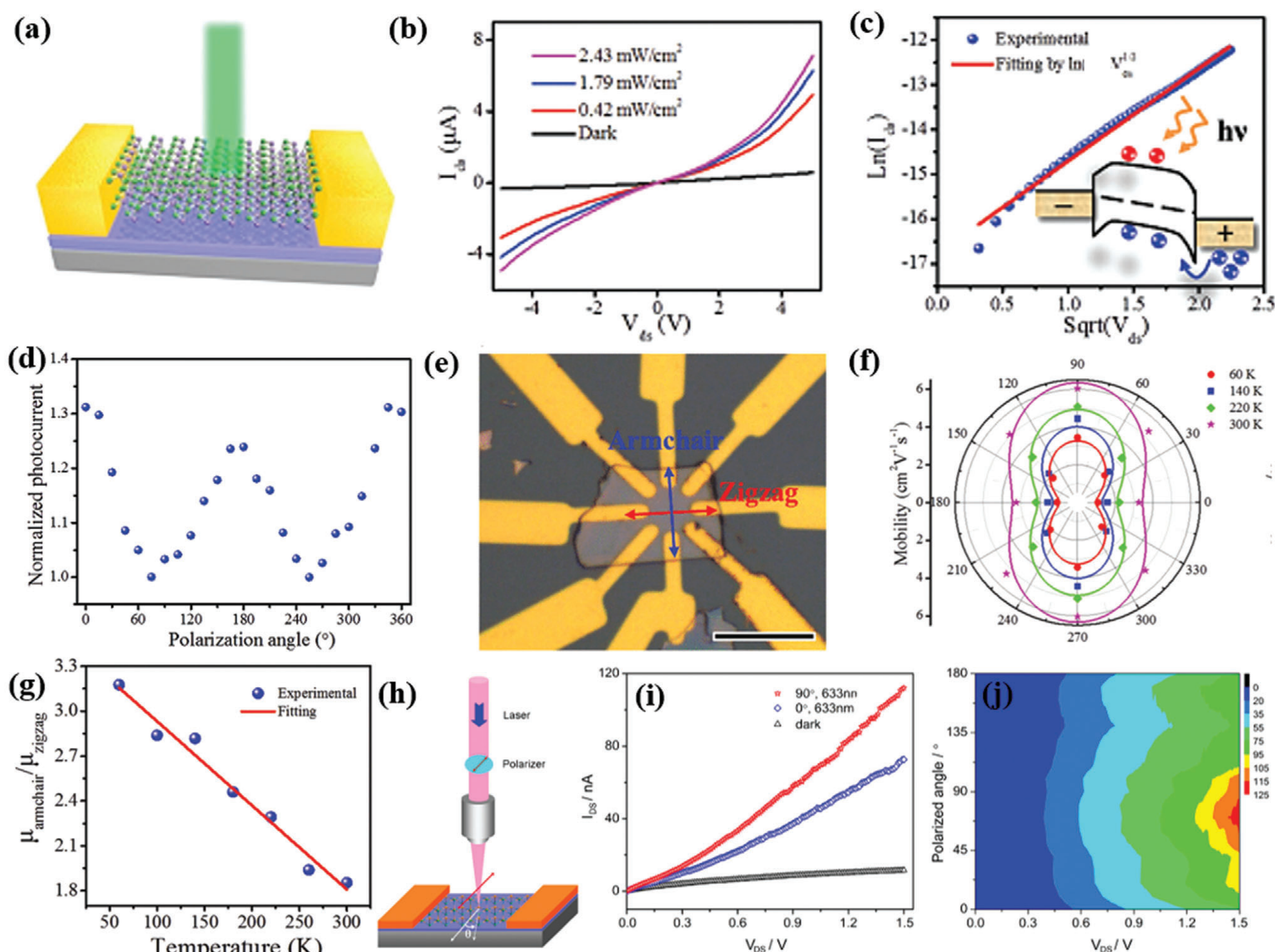

Figure 14. a) Schematic of a GeSe photodetector. b) *I–V* characteristicsc under dark and light illumination with different power intensities. c) Charge carrier transport via thermionic emission; Inset: Illustration of carrier transport under illumination. d) Normalized photocurrent as a function of the incident light polarization angle θ. e) Optical image of the device used for anisotropic electrical measurements (the scale bar is 10 µm). f) Angle-resolved mobility at different temperatures from 60 to 300 K. g) Temperature-dependent mobility ratio ($\mu_{armchair}/\mu_{zigzag}$) along the armchair and zigzag directions. Adapted with permission.[188] Copyright 2018, Wiley-VCH. h) Schematic diagram of a setup used for angle-resolved transport measurements. i) Polarized angle dependent *I–V* curves under dark and illumination with 633 nm laser; j) 2D color map of the angle-resolved transport in GeSe. Reproduced with permission.[193] Copyright 2019, American Chemical Society.

It is found that the electrical mobility and conductivity values were higher in zigzag direction, explained with the difference in the effective masses along the two principle axes. In particular, Vidal et al.[58] and Guo et al.[174] calculated that the effective masses along the zigzag and armchair directions are very different, namely, $m_{zigzag} = 0.21m_0$ and $m_{armchair} = 0.36m_0$. The estimated hole mobility ratio is $\mu_{zigzag}/\mu_{armchair} \approx 1.7$, which showed an excellent agreement with the experimentally obtained value (Figure 15c,d). Furthermore, the activation energy was investigated along both directions in the crystal and found to be 46.5 ± 1.7 and 43.1 ± 0.8 meV along armchair and zigzag direction, respectively. Very recently, Loh and co-workers[46] have reported gate-tunable in-plane ferroelectricity in few-layer SnS FETs. A molecular beam epitaxy (MBE)-grown few-layer NS of 15 nm thickness used to fabricate a large-area SnS FET device exhibited cyclic *I–V* characteristics with −50 V back gate voltage and ±5 V applied bias (Figure 15e). This characteristic was explained by the presence of polarized domains in SnS. Initially, with the positive bias voltage increasing from 0 V, the device shows a low resistive state (LRS) with negatively polarized domains. When the positive bias voltage exceeds +4.3 V, the negatively polarized domains start to reverse to positively polarized ones and enter into the high resistive state (HRS) (from +4.3 to +5 V). The HRS stays as the voltage is decreased to 0 V. The corresponding coercive field, i.e., the electric field when current peak was ≈10.7 kV cm^{-1} (at ±4.3 V), is remarkably smaller than the theoretically calculated value.[39] Such ferroelectric switching in multidomain SnS films was governed by the domain wall motion. In addition, an electrostatically tuned ferroelectricity has appeared (Figure 15f) in SnS due to the carrier depletion. Such carrier depletion was tuned upon variation of the gate voltage. The gate voltage-dependent polarization was recorded by applying a constant voltage sweep (1 V) between the source and the drain (Figure 15g). The total polarization in the FET device can

© 2020 The Authors. Published by Wiley-VCH GmbH

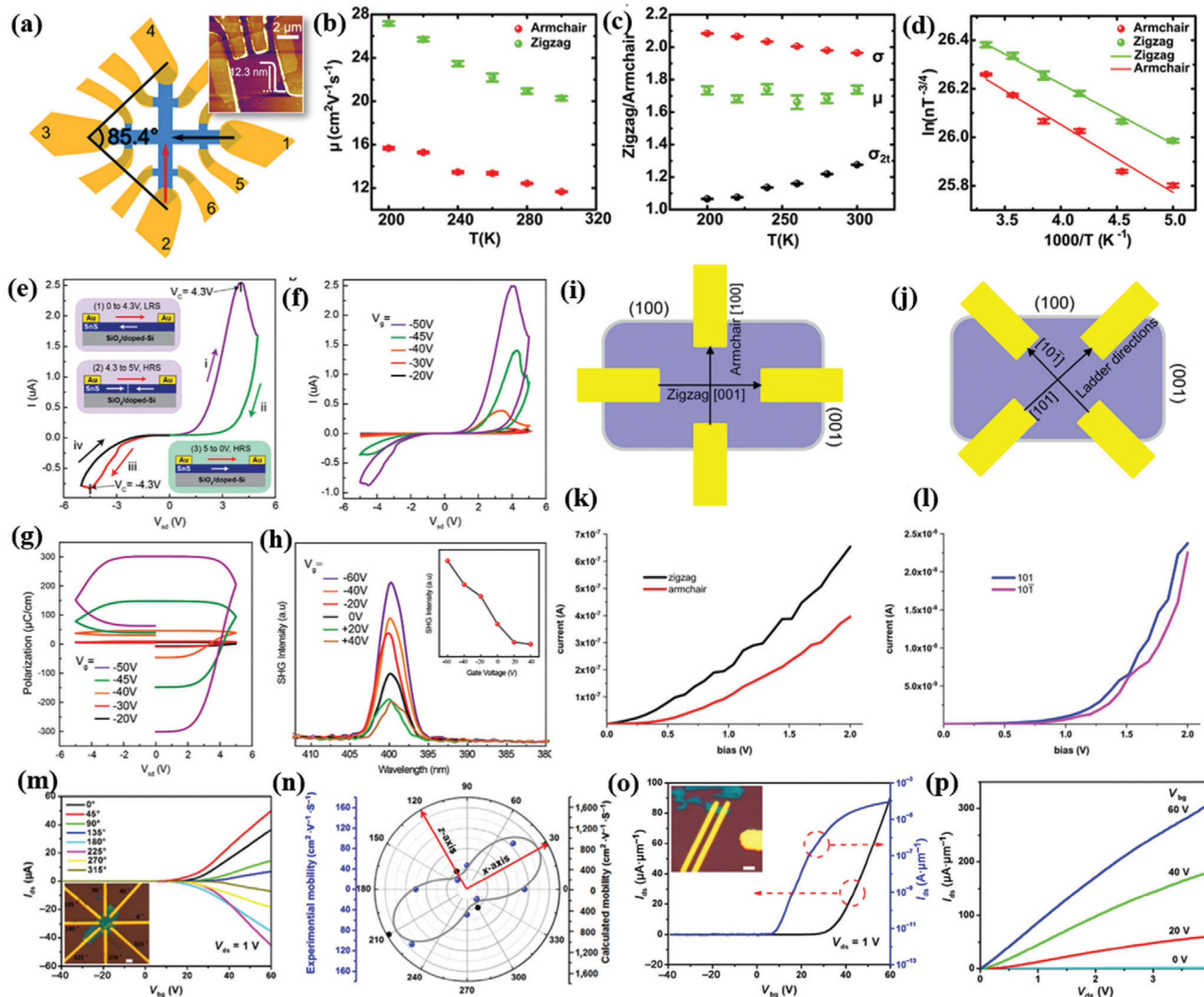

Figure 15. a) Schematic of SnS (12.8 nm) FET device. The black and red arrows represent the anisotropic armchair and zigzag directions, respectively (a). Inset: AFM image of the device. b) Mobility (μ) versus temperature at zero gate voltage. c) Temperature-dependent ratio of μ, σ, and two-terminal conductivity (σ_{2t}). d) Carrier density as a function of temperature. Adapted with permission.[172] Copyright 2017, American Chemical Society. *I–V* characteristics and SHG response of a FET based on few-layer SnS. e) The *I–V* hysteresis curve of the SnS FET device. f) *I–V* hysteresis curves of a lateral SnS memory device measured at different gate bias voltages. g) Gate voltage versus polarization hysteresis curves of the memory device. h) Second harmonic generation (SHG) peaks generated by exciting the back-gated SnS device with laser pulses. Inset: SHG peak intensity as a function of the gate bias voltage. Reproduced with permission.[46] Copyright 2019, American Chemical Society. Schematic representation of the SnS NSs contacted along i) anisotropic directions and j) isotropic directions. k) The current–voltage (*I–V*) characteristics along the armchair and zigzag directions. l) The *I–V* characteristics along isotropic directions. Reproduced with permission.[182] Copyright 2019, American Chemical Society. m) Room-temperature transfer characteristics of SnSe FET based on few-layer NSs. Inset is the optical image of the fabricated device. n) Normalized field-effect mobility of the SnSe FET shown in (m). Blue and black dots are experimental and theoretical data points, respectively. The gray line is the fitting curve. o) Room-temperature transfer characteristics (I_{ds}–V_{gs}) of the transistors along the *x*-direction (at V_{ds} = 1 V). Inset is an optical image of the fabricated device. p) Output characteristics with various back-gate voltages V_{bg}. Adapted with permission.[36] Copyright 2017, Springer Nature.

be calculated as $P(V) = \frac{1}{d}\int I(V)\mathrm{d}V$, where, d is the channel length.

Such remnant polarization increases upon increasing the negative gate bias voltage, namely, increasing the p-doping level in SnS. Gate bias voltage-dependent SHG was additionally observed in the SnS FET device. The SHG peak appeared at 400 nm with an excitation of 800 nm (Figure 15h). The corresponding peak intensity increased with applying more negative gate voltage.

In another study, Klinke and co-workers[182] have demonstrated anisotropy in the electronic behavior of LPE-synthesized large-area single-crystalline multilayered SnS NSs. Four contacts were used to measure the anisotropy in conductivity of the NSs along armchair and zigzag crystallographic directions (Figure 15i–k). The obtained conductivity in armchair (001) and zigzag (100) directions was measured to be 39 and 65 S m^{-1}, respectively. The ratio of the conductivity along armchair and zigzag ($\sigma_{armchair}/\sigma_{zigzag}$)

© 2020 The Authors. Published by Wiley-VCH GmbH

was equal to ≈1.7, which is in very good agreement with reported values.[172,183,188] Besides this, the conductivity along the (101) and (10Î) (ladder) crystal directions was also measured and found to be isotropic, namely, 2.2 and 2.3 S m^{-1}, respectively (Figure 15l). These primary results showed the great potential of SnS as a building block for future electro-optic device application.

A much larger anisotropy in electrical performance was found in few-layer SnSe NSs of 10 nm thickness.[36] The typical angle-resolved electrical measurements have been carried out in a FET configuration with eight-electrode devices spaced at 45° (Figure 15m). The transfer characteristics of the devices were collected with four pairs of diametrically opposite bars as source/drain contacts, by applying an electrical field using a back-gate voltage V_{bg} in the range of −40 to +60 V. The corresponding n-type field effect mobility was obtained by $\mu_x = [dI_{ds}/dV_{bg}] \times [L/(WC_i V_{ds})]$ and found to be highly angle-dependent (Figure 15n); the highest mobility revealed in the 30°/210° direction, while the lowest in 120°/300°. This behavior was closely fitted with the function $\mu_\theta = \mu_x \cos^2(\theta - \varphi) + \mu_z \sin^2(\theta - \varphi)$, where μ_x and μ_z are the mobilities along the armchair (x) and zigzag direction (z), respectively. The calculated anisotropy in electrical field effect mobility along x and z direction ($\mu_{x(max)}/\mu_{z(max)}$) was ≈5.8, which is the highest value among other anisotropic materials, including SnS (1.7),[172] ReS_2 (3.1),[194] and BP (1.5).[20] *Ab initio* theoretical calculations offered a qualitative explanation for the angular dependence of the mobility, which was compared with experimental results. However, the theoretically predicted anisotropy in electrical mobility ratio is slightly lower (≈4.3) than the experimental value. Besides this, the electrical performance was probed in two-terminal SnSe devices (Figure 15o,p); the highest FET mobility obtained was 254 $cm^2 V^{-1} s^{-1}$, and an ON/OFF ratio exceeding $\approx 2 \times 10^7$, which is higher value than that observed in the anisotropic BP.[195]

4.2. Energy Conversion

In a typical solar energy conversion device, the donor materials dominate the main physical processes, including light absorption and exciton transport. In such devices, 2D materials are widely used as in the active (donor) or in various interface/interconnecting layers for exciton generation or charge extraction.[196–204] A promising novel donor material should have direct bandgap (1.2–1.6 eV), high absorption coefficient, high carrier mobility, and low exciton binding energy, E_B. A low E_B is favorable for the efficient separation of photogenerated charge carriers. Besides this, in a solar energy device, the power conversion efficiency (PCE) largely depends on the band alignment between donor and acceptor materials. Another promising alternative property is the bulk photovoltaic effect, attributed to a nonlinear optical (NLO) response that yields net photocurrent in materials with net polarization.[38,205] Owing to their outstanding light absorption properties, 2D TMDs (e.g., MoS_2, $MoSe_2$, WS_2, and WSe_2) have been widely investigated for their application in solar energy conversion.[206] In a similar manner, in-plane anisotropic layered 2D MMCs have recently been investigated as potentially promising materials in photovoltaics.[38,41,42,109,172,207–212]

Dai and co-workers[41] have designed and investigated a new photovoltaic system based on novel 2D MMCs. In particular, the photoresponse and the photovoltaic performance of GeS, GeSe, SnS, and SnSe monolayers were evaluated by means of theoretical quantum transport simulations. The corresponting E_B values have been additionally estimated to be 0.68, 0.52, 0.25, and 0.21 eV for GeS, GeSe, SnS, and SnSe, respectively. These binding energies are much weaker compared with the respective ones calculated for SiC, GaN, and MoS_2 monolayers (**Figure 16**a).[213] Notably, some Se-based MMCs exhibit two times lower E_B than TMDs, leading to easier separation of the photoexcited monolayer MMCs, which were calculated (**Table 6**)[31] and found to be comparable with 3D Si ($\epsilon = 11.9$), 2D MoS_2 ($\epsilon = 7$), and anisotropic BP.[214–216] The higher dielectric constant of selenium-based MMCs comply with lower E_B values. The photovoltaic performance of monolayer MMCs was evaluted with a two-probe device configuration (Figure 16b) and a large photocurrent was measured under illumination with 0.1 W cm^2 light. Moreover, the obtained photocurrent along armchair direction was higher as compared to the zigzag one. Notably, in seleneum-based monolayers, the induced photocurrents, namely, 12.0 and 14.0 mA mm^{-2} for Ge and Sn ones, respectively, were higher than the sulfur-based ones. In addition, a redshift in photocurrent appeared in selenides compared to sulfides (Figure 16c–j). This important phenomenon is attributed to their lower bandgaps.[43,217] The photovoltaic performance was evaluated through a photoresponce coefficient (R_{ph}) and EQE. It is important that the R_{ph} vaules in MMCs are much higher than those of MoS_2 phototransistors and three orders of magnitude higher than that of graphene detectors. As shown in Table 6, the corresponding EQE values are higher in selenides than sulfides, indicating that the former are more suitable as photovoltaic materials than the latter ones. Very recently, Rangel et al.[38] have reported a large photocurrent shift (≈100 μA V^{-2}) in single-layer Ge and Sn MMCs. Such shift was correlated with the large spontaneous effective 3D electric polarization of ≈1.9 C m^{-2} in Ge and Se MMCs.

In addition, Lv et al.[219] have systematically explored the electrical properties of bilayer GeSe with different metal electrodes. In particular, the interface geometry, electronic properties, band alignment, Schottky and tunneling barriers were calculated with Au, Ag, Al, Cu, Pt, and Ni, electrodes, respectively. Among such metals tested, Au, Pt, and Ni showed lower Schottky and tunneling barriers. In addition, a heterostructure of monolayer SnS with a bilayer GeSe has been constructed to investigate the resulting photovoltaic performance (**Figure 17**a), in which the CBM and VBM energy of donor is much lower than the energy of acceptor and forming a type-II band alignment. This type-II band alignment is favorable for effective separation of photogenerated charge carriers. In such device, the PCE was calculated to be 18% (Figure 17b), which is larger than the best certified efficiency of organic photovoltaic cells[220] and comparable with other heterostructures-based[221–223] solar cells.

The extended absorption of MMCs in the IR range was exploited by Hou et al.[224] The authors fabricated bi-component heterojunction solar cells (Figure 17c) comprising an organic perovskite layer matched with a GeS, SnS, GeSe, or SnSe layer. The calculated absorption efficiency of the bi-component devices complied well with that of the combined absorption of the two components (Figure 17d–g). Notably, the device comprising a GeSe layer coupled with a $CH_3NH_3PbI_3$ one to form its active area exhibited a strong absorption in the range of 300–1200 nm.

© 2020 The Authors. Published by Wiley-VCH GmbH

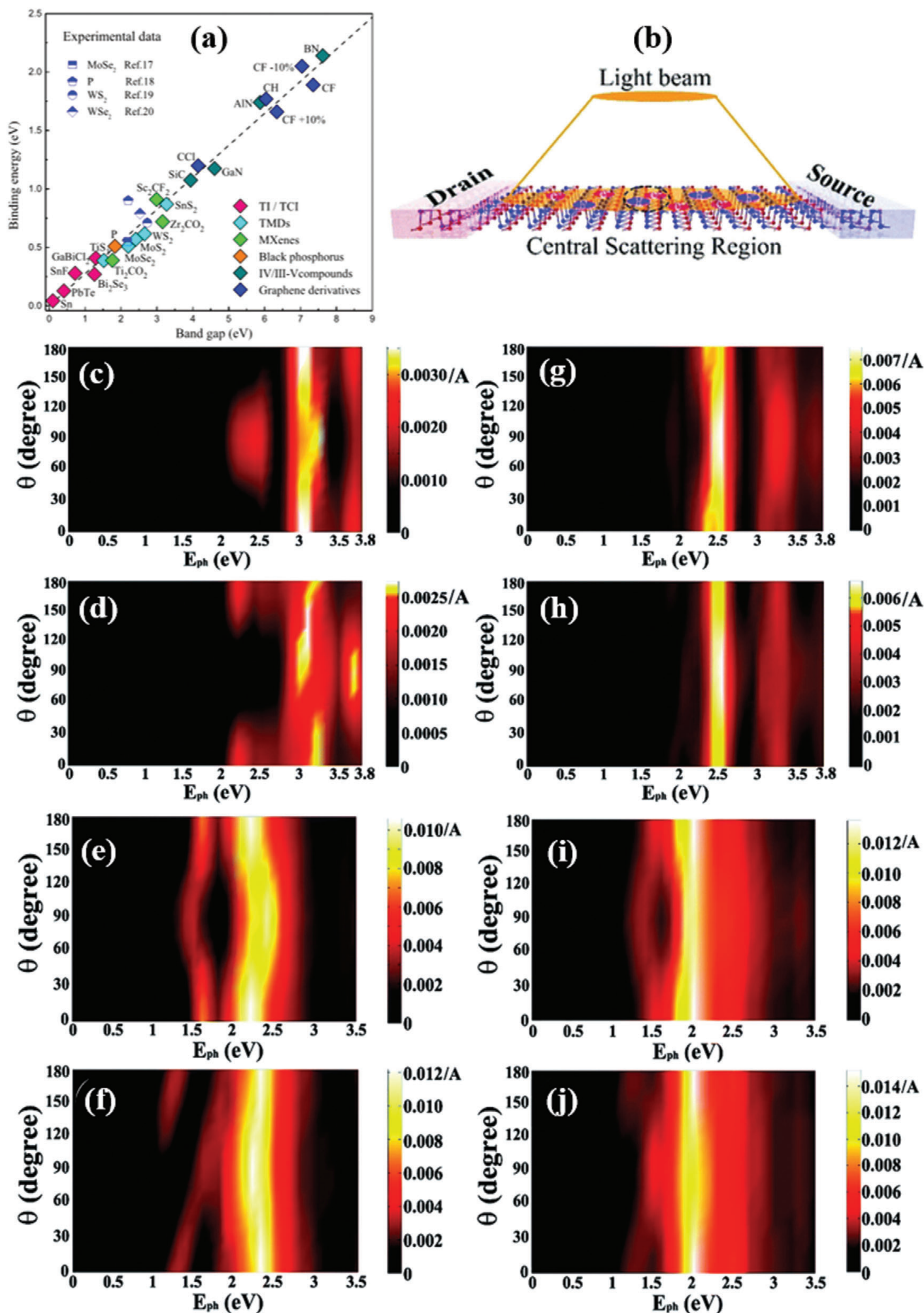

Figure 16. a) Bandgap versus exciton binding energy of existing 2D and bulk materials. Reproduced with permission.[213] Copyright 2017, American Physical Society. b) schematic of two-probe monolayer devices. Photocurrent along armchair and zigzag direction for c,d) GeS, e,f) GeSe, g,h) SnS, and i,j) SnSe monolayer; the vertical axis is the polarizing angle and the horizontal one the photon energy. Reproduced with permission.[41] Copyright 2017, Royal Society of Chemistry.

 © 2020 The Authors. Published by Wiley-VCH GmbH

Table 6. Summary of dielectric constant of different materials with structural in-plane anisotropy obtained from theoretical calculations[31,214,216,218].

Materials	Layer number/thickness	Dielectric constant (ϵ)		EQE [%]	References
Si	2 nm thick	11.9		–	[215,216]
MoS_2	Monolayer	7		–	[214,216]
BP		7.47 (armchair)	3.06 (zigzag)	–	[218]
GeS		8.7 (armchair)	8.6 (zigzag)	10.27	[31,41]
GeSe		13.8 (armchair)	14.7 (zigzag)	25.43	[31,41]
SnS		9.9 (armchair)	10.0 (zigzag)	22.01	[31,41]
SnSe		12.5 (armchair)	12.8 (zigzag)	30.32	[31,41]

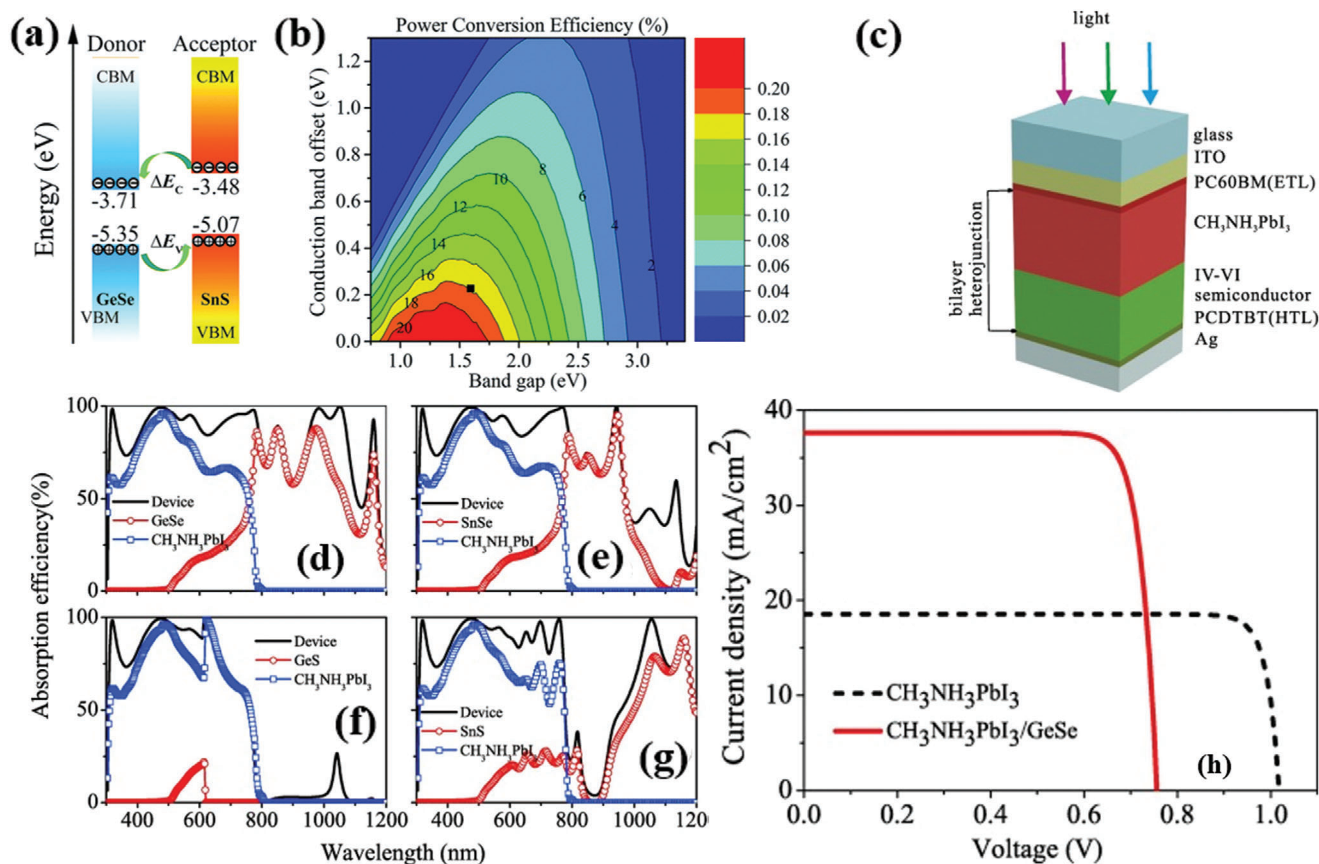

Figure 17. a) The energy band alignments of 2D GeSe and SnS monolayers. b) Contour plot of the computed power conversion efficiency. Reproduced with permission.[219] Copyright 2018, The Royal Society of Chemistry. c) Schematic structure of a bicomponent heterojunction solar cell comprising a perovskite ($CH_3NH_3PbI_3$) layer coupled with an MMC one to form its active area; Calculated absorption efficiency of d) $CH_3NH_3PbI_3$/GeSe, e) $CH_3NH_3PbI_3$/SnSe, f) $CH_3NH_3PbI_3$/GeS, and g) $CH_3NH_3PbI_3$/SnS. h) J–V curves of bicomponent and single-layer (perovskite only) solar cell. Reproduced with permission.[224] Copyright 2018, Elsevier.

Likewise, the corresponding external and internal quantum efficiency of the bi-component heterojunction solar cells were extended in the range of 300–1200 nm, contrary to those of the single perovskite layer cell, which were only limited in the range of 300–800 nm. Furthermore, the current density–voltage characteristic curves of the solar cells were presented (Figure 17h). It is shown that all the electrical parameters, including the short-circuit current, J_{sc}; the open-circuit voltage, V_{oc}; the fill factor (FF); and the PCE of the bicomponent cell were much higher than those of the single-layer ones. In particular, the obtained J_{sc}, V_{oc}, FF, and PCE values were 37.62 mA cm^{-2}, 0.76 V, 83.14%, and 23.77% for the bi-component solar cell and 18.53 mA cm^{-2}, 1.02 V, 88.15%, and 16.66% for the single perovskite cell, respectively. The significant rise of J_{sc} observed in the bi-component cell can be attributed to the enhanced absorption, at higher wavelengths, by the GeSe layer. In another work, Michael et al.[42] have investigated the performance of 2D piezo-phototronic based solar cells. In such devices, an external strain was applied to monitor the

 © 2020 The Authors. Published by Wiley-VCH GmbH

piezo-phototronic effect. The strain-induced PCE of a monolayer SnS, SnSe, GeS, and GeSe can improve up to 18.2%, 16.6%, 7.0%, and 15.4%, respectively.

Another important application of MMCs is their catalytic activity.[225–228] In particular, the photocatalytic water splitting for energy conversion and the electrode catalyst (cathode) activity for energy storage have been theoretically investigated. In photocatalytic water splitting and electrode catalytic activity, both the electronic structure and the optical properties of the semiconductor play an important role. When an incident light falls on a semiconducting catalysis material, an electron gets excited to CB and generate electron–hole (e–h) pairs. Subsequently, the electrons then take part in hydrogen evolution reaction (HER), while the holes cause an oxygen evolution reaction (OER), which are expressed as: H_2: $2H^+ + 2e^- \rightarrow H_2$ (HER) and O_2: $H_2O + 2h^+ \rightarrow 1/2O_2 + 2H +$ (OER), respectively. The minimum E_g required for these two processes to simultaneously take place is 1.23 eV.[229] More interestingly, Zhang et al.[230] have reported that an indirect bandgap material is more suitable for photocatalytic activity. Most of MMCs exhibit larger bandgaps (direct or indirect) than the minimum energy required for the water splitting reaction (>1.23 eV).[226] In particular, the GeSe, SnS, and SnSe exhibited larger overpotential, which was behaving as a potential material for HER. On the contrary, SiS, SiSe, and GeS exhibit good photocatalytic activity in basic and acidic conditions. Apart from the photocatalytic activity, MMCs are predicted to be promising as cathode catalyst materials in Li-O_2 batteries.[227] However, the impact of in-plane anisotropy of MMCs in catalytic activity has not yet been investigated.

4.3. Valleytronics

The term *valleytronics* comes as the combination of the words *valley* and *electronics* and describes the ability to tune the carrier conduction in the valleys of a material's band structure. The idea was initially applied for the development of new quantum computing devices,[231–234] which use the valley polarization as a means to store and/or carry the quantum information.[231,235] Castro Neto and co-workers[37] theoretically predicted the valley properties and the optical selection rules in MMCs. In particular, the 2D form of SnS was studied via a combination of ab initio calculations and k·p theory. In monolayer SnS, two pairs of valleys were identified, placed along two perpendicular axes, which can be selected exclusively with linearly polarized light and can be separated using nonlocal electrical measurements. Thereafter, Park and co-workers[39] investigated the multistability of the direction of the puckering of monolayer MMCs using first principle calculations. It is found that the monolayer of SnS and GeSe exhibits two inequivalent valleys in momentum space, which are dictated by the puckering orientation along armchair or zigzag direction. These valleys can be excited selectively using linearly polarized light.

The valleytronic behavior of low-dimensional materials can be probed through the variation of different experimental conditions, such as cryogenic temperature and/or strong electric and magnetic field. However, such requirements inevitably pose a plethora of practical challenges that create a high barrier in advancing the technology toward practical applications. Very recently, the realization of valley polarization at room temperature in MMCs was revealed. In particular, Lin et al.[51] demonstrated the direct access and identification of different sets of valleys in bulk in-plane anisotropic SnS (**Figure 18**a). The valley selectivity was recorded via the photoluminescence (PL) setup for SnS (Figure 18, top panel) and the corresponding polarization degree of the valleys was determined by[236]

$$P_{2D} = \frac{I(\sigma_-) - I(\sigma_+)}{I(\sigma_-) + I(\sigma_+)} \tag{6}$$

where $I(\sigma_{+/-})$ represents the left (+) and right (−) circularly polarized PL intensity. Two peaks of SnS PL spectra were recorded at 817 nm (A) and 995 nm (B) (Figure 18b), respectively. To account for the valley polarization, the PL spectra were recorded upon rotating the sample with respect to the incident and detection polarizations (Figure 18c,d) that were parallel to each other. The polarization degree is called intervalley polarization

$$P_{\text{intervalley},\Gamma X} = \left(\frac{I_{\Gamma X||}(\theta = 90°) - I_{\Gamma Y||}(\theta = 90°)}{I_{\Gamma X||}(\theta = 90°) + I_{\Gamma X\perp}(\theta = 90°)} \right) \tag{7}$$

and

$$P_{\text{intervalley},\Gamma Y} = \left(\frac{I_{\Gamma Y||}(\theta = 0°) - I_{\Gamma Y||}(\theta = 0°)}{I_{\Gamma Y||}(\theta = 0°) + I_{\Gamma X||}(\theta = 0°)} \right) \tag{8}$$

where, $I_{i||}(\theta)$ stand for the PL intensity under parallel polarization for the *i* valley. It is observed that the (A) peak maximizes at the polarization that minimizes the (B) peak and vice versa. Such 90° phase shift between the peaks signifies the selectivity of two valleys. The corresponding intervalley polarization degrees of the 817 (lying on ΓY axis) and 995 nm (lying on ΓX axis) peaks, calculated using the formula (7) and (8) were 92% and 62%, respectively. Unlike other 2D materials, SnS has a unique valleytronic system, which relies on the nondegeneracy of the valleys. In such system, the valley polarization degree, between valleys and within a valley, can be assessed by

$$P_{\text{intravalley},\Gamma X} = \left(\frac{I_{\Gamma X||}(\theta = 90°) - I_{\Gamma X\perp}(\theta = 90°)}{I_{\Gamma X||}(\theta = 90°) + I_{\Gamma X\perp}(\theta = 90°)} \right) \tag{9}$$

and

$$P_{\text{intrarvalley},\Gamma Y} = \left(\frac{I_{\Gamma Y||}(\theta = 90°) - I_{\Gamma Y\perp}(\theta = 90°)}{I_{\Gamma Y||}(\theta = 90°) + I_{\Gamma Y\perp}(\theta = 90°)} \right) \tag{10}$$

The intravalley polarization degrees in ΓX ($P_{\text{intravalley},\Gamma X}$) and ΓY ($P_{\text{intravalley},\Gamma Y}$) directions were realized to be 95% and 96%, respectively. Such intravalley polarization values are among the highest polarization degrees reported, from experiments conducted at cryogenic temperatures.[236–238]

In another study, Chen et al.[50] have explored a novel valley-selective linear dichroism of the PL in SnS. The PL spectra (at 77 K) of a bulk SnS (of 109 nm thickness) exhibited two photon emission peaks located at 1.16 and 1.204 eV (**Figure 19**a,b). The origin of PL was theoretically predicted previously,[37] attributed to the presence of two valleys with close energy gaps

© 2020 The Authors. Published by Wiley-VCH GmbH

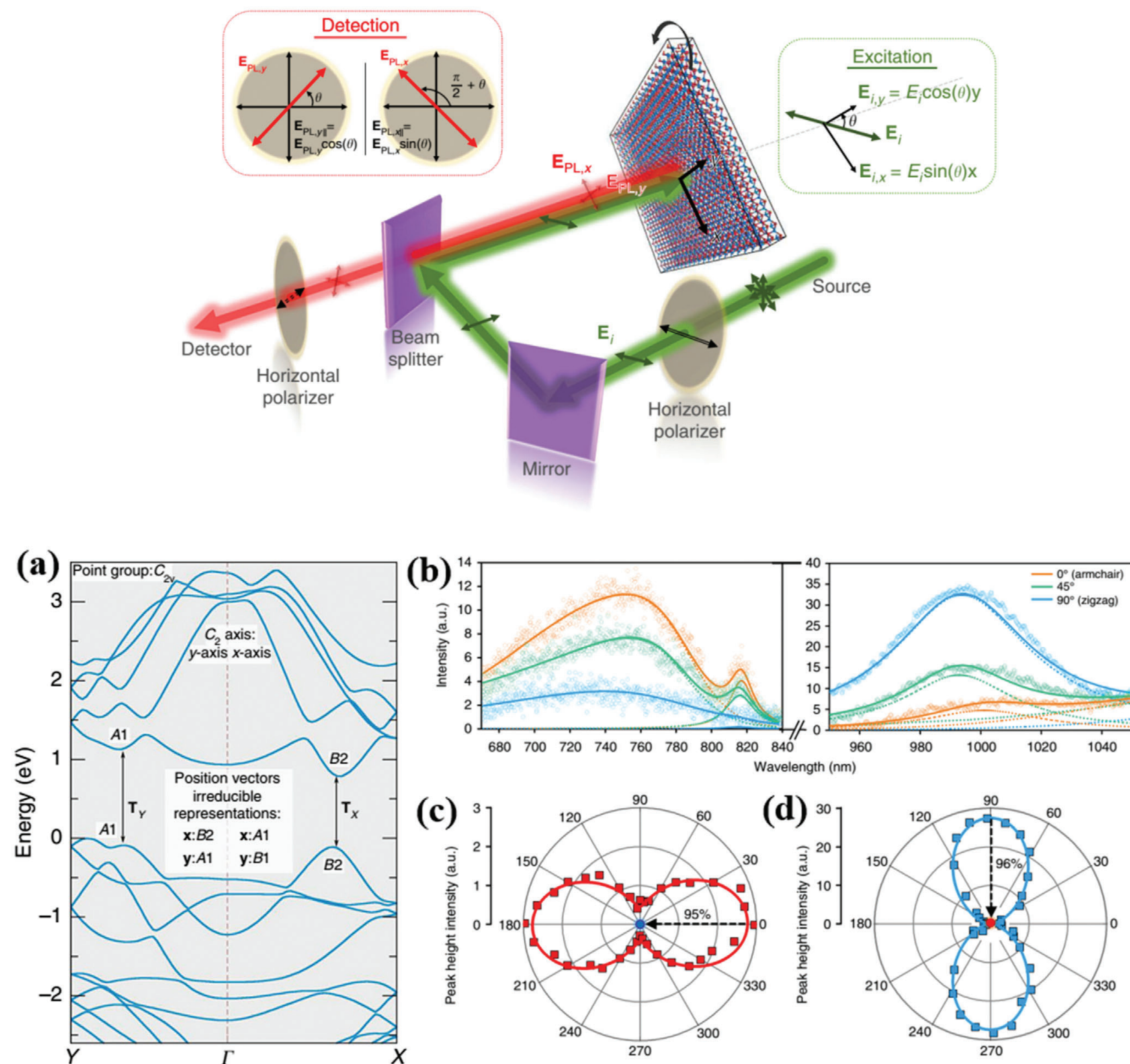

Figure 18. Top panel: schematic of the experimental setup for valley polarization measurements. a) Electronic band structure of bulk SnS. The *Y* and *X* axes correspond to the armchair and zigzag directions, respectively; PL measurements of SnS. b) Deconvolution of PL peaks with respect to sample orientation (rotation by 45° and 90°, respectively). c,d) Polar plots of PL peak intensities for the different valleys (at 817 and 995 nm). The black dashed arrows are the two data points before and after the 90° rotation of the second polarizer, corresponding to PL intensities at the ΓY and ΓX valleys, respectively. Reproduced with permission.[51] Copyright 2018, Author(s), licensed under a Creative Commons Attribution 4.0 License, Nature Publishing Group.

along the ΓX and ΓY directions in momentum space.[239] On the other hand, Gomez and Carvalho[31] have reported that the $E_C^Y - E_V^X < E_C^Y - E_V^Y < E_C^X - E_V^X$, where E_I^J (J = X, Y and I = C, V) is the energy of the CBM and VBM of the ΓX and ΓY valleys, respectively. Considering that the two PL peaks arise from the band-edge transitions, the polarized PL spectra were monitored and presented in Figure 19c. It is observed that the angular-resolved PL intensities of the two PL peaks exhibited different polar shapes with $\cos^2\theta$ and $\sin^2\theta$ dependencies (Figure 19d,e). Furthermore, the band-edge emission along the ΓX and ΓY valleys is dependent on the excitation linear polarization. In particular, for each valley ΓX or ΓY the emission becomes dominant when the excitation linear polarization is parallel to its corresponding crystal orientation in real space. The experimentally obtained degrees of polarization for anisotropic emissions from ΓX and ΓY valleys were 8.5% and 3.4%, respectively.

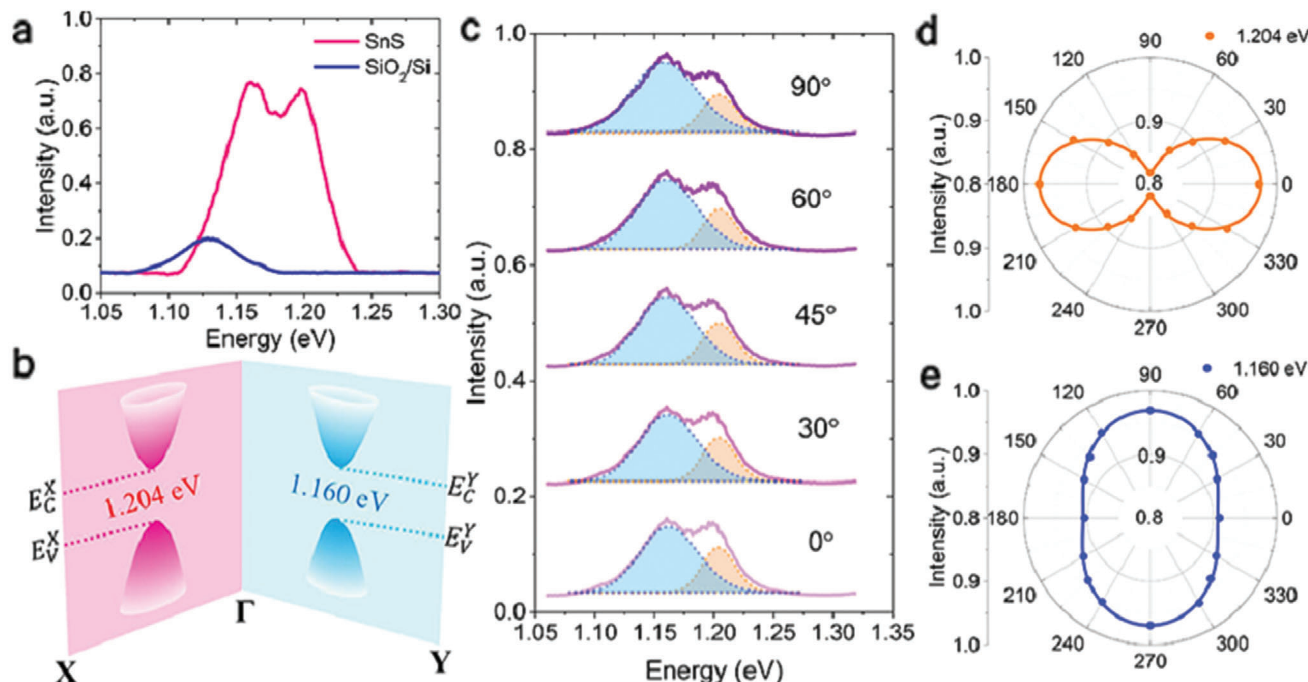

Figure 19. a) PL spectra of a SnS flake and its substrate (excitation photon energy of 2.33 eV at 77 K), b) band structure schematics of layered SnS corresponding to two valleys of close energy gaps in the ΓX and ΓY direction. c) PL spectra under different excitation linear polarization directions. d,e) Angular-resolved PL intensity of the emission peaks at 1.204 eV (Γ-X valley) and 1.160 eV (Γ-Y valley). Reproduced with permission.[50] Copyright 2018, The American Chemical Society.

4.4. Second Harmonic Generation

SHG is a NLO process describing the light–matter interaction where the induced polarization depends nonlinearly on the external electric field. SHG has been broadly applied for the materials analysis, sensors development, advanced spectroscopy, high-resolution imaging, lasers, frequency conversion, electro-optic modulators, and switches.[240–243] Macroscopically, the nonlinear process is described by the light-induced polarization expressed as

$$P = \varepsilon_0 \left(\chi E + \chi^{(2)} E^2 + \chi^{(3)} E^3 + \cdots\right) \tag{11a}$$

$$P = \varepsilon_0 \chi E + P_{\mathrm{NL}} \tag{11b}$$

where, ϵ_0 is the permittivity in vacuum, χ is the electric susceptibility of the medium, and E is the electric field of the incident light. The first term is the linear part, while the rest is the nonlinear part (P_{NL}). The $\chi^{(n)}$ (n = 1,2,3...) corresponds to the elevated-order nonlinearity in the medium. The generation of NLO response depends on the intrinsic crystalline symmetry, the microscopic transition dipole matrix, as well as on the specific frequency and orientation of the optical field applied. On top of them, a centrosymmetric or non-centrosymmetric crystal structure plays a pivotal role due to the different order electric susceptibility tensors describing each case. To date, a large number of 2D materials including mono/multilayer MoS_2, $MoSe_2$, WS_2, WSe_2, hBN, GaSe, and InSe has been reported to exhibit the second and higher order harmonics generation.[244–251] However, all of them belong to the centrosymmetric point group D_{3h} comprising a single independent SHG susceptibility tensor element. On the other hand, the MMC monolayers belong to a non-centrosymmetric point group and thus exhibit up to five independent SHG susceptibility tensor elements. Qian and Wang[52] have theoretically investigated the optical second harmonic generation in monolayer MMCs. In particular, the quasiparticle band structure of a monolayer GeSe has been calculated using first principles, quasi-atomic orbital method. Moreover, the second-order susceptibility tensors in MMCs, MoS_2, and hBN were estimated (**Figure 20**a–c). Specifically, the MMCs monolayers belong to the point group C_{2v}, while MoS_2 and hBN ones in D_{3h}. The D_{3h} point group exhibits one independent nontrivial SHG susceptibility tensor element that satisfies the relation $\chi^{(2)}_{yxx} = \chi^{(2)}_{xyx} = \chi^{(2)}_{xxy} = -\chi^{(2)}_{yyy}$. On the other hand, the C_{2v} exhibits five independent susceptibility tensor elements (Figure 20a) satisfying the relations $\chi^{(2)}_{yxx}$, $\chi^{(2)}_{yyy}$, $\chi^{(2)}_{yzz}$, $\chi^{(2)}_{xyx} = -\chi^{(2)}_{xxy}$ and $\chi^{(2)}_{zzy} = \chi^{(2)}_{zyz}$. The obtained magnitude of the calculated susceptibility tensor element at 3.22 eV was calculated to be 5.16×10^6 pm^2 V^{-1} for GeSe, which is much higher than that of MoS_2 (3.02×10^5 pm^2 V^{-1}) and hBN (6.38×10^4 pm^2 V^{-1}). Moreover, an independent SHG tensor element ($\chi^{(2)}_{xyx} = \chi^{(2)}_{xxy}$) with a substantial magnitude, which is much higher than the other three components of a GeSe monolayer, was predicted. The angular dependence of the SHG response that can be measured, for example, by rotating the crystal, and measuring the SHG polarization and intensity can provide important information on 2D materials anisotropy.[244,252,253] Considering normal incidence geometry, the angular dependent SHG susceptibilities for the point group C_{2v} and D_{3h} had been calculated. The

© 2020 The Authors. Published by Wiley-VCH GmbH

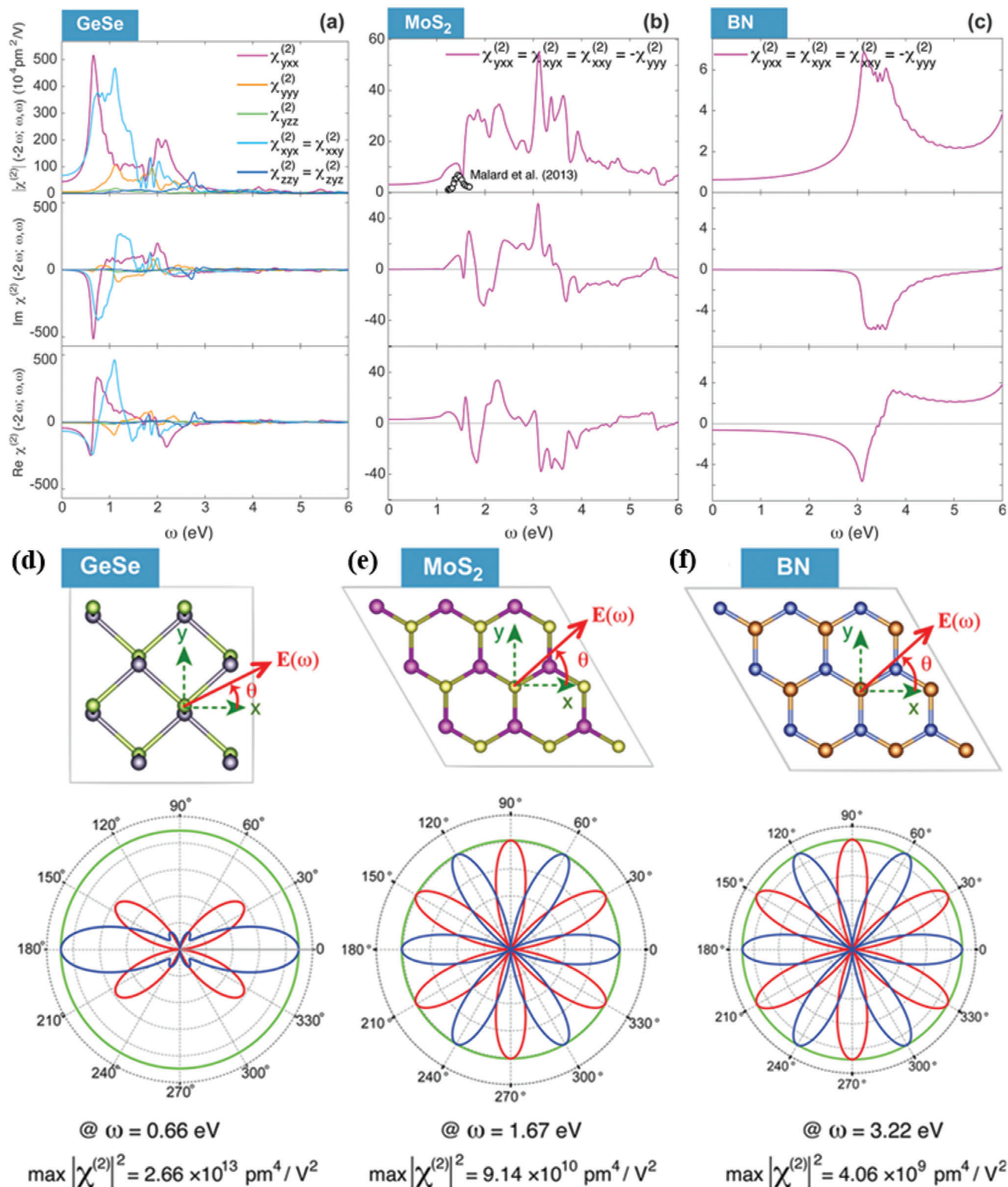

Figure 20. The magnitude, imaginary, and real component of SHG susceptibility for: a) a GeSe monolayer which has seven nonzero susceptibility tensor elements, b) a MoS_2 monolayer which has four independent SHG elements, and c) a h-BN monolayer with only one independent element. Black dots indicate the experimental values. d–f) Polarization anisotropy of SHG susceptibilities in monolayer GeSe, MoS_2, and h-BN. The red/blue solid lines are the polarization components of the SHG response parallel/perpendicular to the polarization of the incident electric field $E(\omega)$. θ is the rotation angle between $E(\omega)$ and the crystal lattice. Reproduced with permission.[52] Copyright 2018, American Chemical Society.

© 2020 The Authors. Published by Wiley-VCH GmbH

corresponding angulardependent polar plots of SHG are shown in Figure 20d–f, together with the corresponding frequency of the excitation field, ω and the maximum $\chi^{(2)}$ values. A significantly polarized colossal SHG response in monolayer GeSe with its maximum value located at an angle of 0° was observed. On the other hand, the polar plots of MoS_2 monolayer precisely reflect the D_{3h} symmetry. In the case of monolayer GeSe, the total susceptibility ($\chi_{\text{total}}^{(\text{abc})}$ $(-2\omega, \omega, \omega)$) contains an interband contribution ($\chi_{\text{intra}}^{(\text{abc})}$), a modification due to the intraband motion ($\chi_{\text{inter}}^{(\text{abc})}$), and a modulation due to interband motion ($\chi_{\text{mod}}^{(\text{abc})}$). Such contributions were accounted by six tensor terms

$$\chi_{\text{intra}}^{(\text{abc})} \equiv \chi_{\text{i}}(\omega) + \chi_{\text{i}}^{(\text{v})}(2\omega) + \chi_{\text{i}}^{(\text{r})}(2\omega) \tag{12}$$

$$\chi_{\text{inter}}^{(\text{abc})} \equiv \chi_{\text{e}}(\omega) + \chi_{\text{e}}(2\omega) \tag{13}$$

$$\chi_{\text{mod}}^{(\text{abc})} = \chi_{\text{m}}(\omega) \tag{14}$$

Among such susceptibility terms, the $\chi_{\text{i}}^{(\text{v})}(2\omega)$ and $\chi_{\text{i}}^{(\text{r})}(2\omega)$ are the leading ones behind the giant SHG susceptibility in GeSe monolayer, governed by the interband and intraband Berry connection in the monolayer. These leading susceptibility terms are distributed at four spots in the vicinity of the first Brillouin zone and concentrated around the two valleys in the bandgap. Moreover, the authors have predicted SHG strength in the monolayer and trilayer GeSe and SnSe, which has very similar SHG strength and shape.

5. Summary and Outlook

In this Review, we have presented the fundamental properties and recent advancements on the synthesis of layered 2D, in-plane anisotropic, phosphorene analog group IV_A–VI MMCs and their emerging promising applications in electronics, optoelectronics, and nanophotonics. The in-plane anisotropy along the armchair and zigzag directions makes these materials more important to explore the rich physics of 2D materials. Nevertheless, the experimental research on MMCs is still in a preliminary stage. Among the synthesis approaches, the mechanical exfoliation is fairly simple and easy to obtain low defect and highly crystalline nanoflakes. However, the low exfoliation yield, lateral size repeatability, and reproducibility in layer number, harshly restrict its application for large-area electronics and optoelectronics. LPE is an effective method for bulk production and is widely used for the solution processable flexible organic and hybrid electronic applications. However, the control synthesis of MMCs with thickness uniformity in various solvents has not been investigated yet. Besides this, the choice of appropriate solvent for successful isolation into thinner layers is also an important topic of research. In contrast, the physical and/or chemical vapor deposition is no doubt the most promising route for large-area 2D materials production for future electronic applications. At present, the synthesized MMCs are restricted only in few monolayers and therefore the isolation of single layer with good crystallinity remains a great challenge. In general, there is a huge room for further study on the controlled synthesis of electronic-grade ultrathin, even atomically thin, MMC layer by means of top-down and bottom-up approaches.

To date, the optical and electrical anisotropic properties of orthorhombic MMCs have been investigated in few-layer NSs, while the intriguing anisotropic optoelectronic response of a monolayer is only theoretically predicted. Such unique anisotropic response appeared due to the puckered crystal lattice structures of MMCs, resulting from the difference in the effective mass and refractive index along the armchair and zigzag directions, respectively. On top of that, the large absorption coefficient and the large spin–orbital coupling pave the way for the application of MMCs in solar energy harvesting and valley electronics. Apart from the current inability to isolate MMCs monolayers, the fast growing field of MMCs is also hampered by a huge gap between the materials' fundamental studies and device applications.

Notably, puckered structured Ge and Sn-based chalcogenides are p-type semiconductors, which are desirable to form heterojunctions with n-type TMDs to explore the interface physics at the nanoscale and the subsequent electronic properties. As a consequence, strong light–matter interaction and reduced dimensionality leads to the formation of quasi-1D excitons and trions within in-plane anisotropic MMCs, while quasi-2D excitons and trions in isotropic TMDs materials. Therefore, heterostructures of in-plane anisotropic/isotropic 2D materials can provide unique interlayer interactions between quasi-1D and 2D excitonic species. This may find promising applications including high-performance photoemitters and exciton–polariton lasers. Nevertheless, to date there are limited studies on such interlayer optical and electronic responses.[254–258] Furthermore, the highly anisotropic electrical and optical properties in MMCs integrated with 0D (quantum dots) or 1D organic and/or inorganic and perovskite semiconductor materials could open up a new path for next-generation electronic applications. Overall, the very recent exciting achievements in the field of few-layer MMCs showed a great potential for their application in next-generation electronic, optoelectronic, and emerging nanophotonics, including valley electronics, solar cells, sensors, and nonlinear optical applications. However, the wealth of arising possibilities in fundamental research of 2D MMCs and the emerging new approaches to MMCs monolayer synthesis and functionalization prescribe a future where tuning of MMC band structure and subsequent electronic properties can be accomplished with a level of sophistication that we cannot presently imagine.

Note added. We noticed that during the peer review process, a novel study on the PVD growth of monolayer SnS and the demonstration of room temperature purely in-plane ferroelectricity and SHG was published by Nagashio and co-workers.[259]

Acknowledgements

This work was supported by the EC HORIZON 2020 projects 'NFFA–Europe', under Grant agreement No. 654360 and 'MouldTex', under Grant Agreement No. 768705. The authors are thankful for the kind permission from the corresponding publishers to reproduce the figures included into this article.

 © 2020 The Authors. Published by Wiley-VCH GmbH

Conflict of Interest

The authors declare no conflict of interest.

Keywords

2D metal monochalcogenides, growth, in-plane anisotropy, photonics; roptoelectronics

Received: May 4, 2020
Revised: July 24, 2020
Published online: September 6, 2020

[1] K. S. Novoselov, A. K. Geim, S. V. Morozov, D. Jiang, Y. Zhang, S. V. Dubonos, I. V. Grigorieva, A. A. Firsov, *Science* **2004**, *306*, 666.
[2] K. S. Novoselov, D. Jiang, F. Schedin, T. J. Booth, V. V. Khotkevich, S. V. Morozov, A. K. Geim, *Proc. Natl. Acad. Sci. USA* **2005**, *102*, 10451.
[3] J. D. Caldwell, I. Aharonovich, G. Cassabois, J. H. Edgar, B. Gil, D. N. Basov, *Nat. Rev. Mater.* **2019**, *4*, 552.
[4] C. Tan, X. Cao, X. J. Wu, Q. He, J. Yang, X. Zhang, J. Chen, W. Zhao, S. Han, G. H. Nam, M. Sindoro, H. Zhang, *Chem. Rev.* **2017**, *117*, 6225.
[5] S. Manzeli, D. Ovchinnikov, D. Pasquier, O. V. Yazyev, A. Kis, *Nat. Rev. Mater.* **2017**, *2*, 17033.
[6] W. Choi, N. Choudhary, G. H. Han, J. Park, D. Akinwande, Y. H. Lee, *Mater. Today* **2017**, *20*, 116.
[7] C. Tan, Z. Lai, H. Zhang, *Adv. Mater.* **2017**, *29*, 1701392.
[8] E. Shi, B. Yuan, S. B. Shiring, Y. Gao, Akriti, Y. Guo, C. Su, M. Lai, P. Yang, J. Kong, B. M. Savoie, Y. Yu, L. Dou, *Nature* **2020**, *580*, 614.
[9] G. Grancini, M. K. Nazeeruddin, *Nat. Rev. Mater.* **2019**, *4*, 4.
[10] L. Mao, C. C. Stoumpos, M. G. Kanatzidis, *J. Am. Chem. Soc.* **2019**, *141*, 1171.
[11] M. Naguib, V. N. Mochalin, M. W. Barsoum, Y. Gogotsi, *Adv. Mater.* **2014**, *26*, 992.
[12] Z. Fu, N. Wang, D. Legut, C. Si, Q. Zhang, S. Du, T. C. Germann, J. S. Francisco, R. Zhang, *Chem. Rev.* **2019**, *119*, 11980.
[13] Y. Li, S. Huang, C. Wei, C. Wu, V. N. Mochalin, *Nat. Commun.* **2019**, *10*, 3014.
[14] K. F. Mak, C. Lee, J. Hone, J. Shan, T. F. Heinz, *Phys. Rev. Lett.* **2010**, *105*, 136805.
[15] N. R. Glavin, R. Rao, V. Varshney, E. Bianco, A. Apte, A. Roy, E. Ringe, P. M. Ajayan, *Adv. Mater.* **2020**, *32*, 1904302.
[16] L. Li, Y. Yu, G. J. Ye, Q. Ge, X. Ou, H. Wu, D. Feng, X. H. Chen, Y. Zhang, *Nat. Nanotechnol.* **2014**, *9*, 372.
[17] A. Carvalho, M. Wang, X. Zhu, A. S. Rodin, H. Su, A. H. Castro Neto, *Nat. Rev. Mater.* **2016**, *1*, 16061.
[18] X. Liu, C. R. Ryder, S. A. Wells, M. C. Hersam, *Small Methods* **2017**, *1*, 1700143.
[19] M. Akhtar, G. Anderson, R. Zhao, A. Alruqi, J. E. Mroczkowska, G. Sumanasekera, J. B. Jasinski, *NPJ 2D Mater. Appl.* **2017**, *1*, 5.
[20] F. Xia, H. Wang, Y. Jia, *Nat. Commun.* **2014**, *5*, 4458.
[21] V. Tran, R. Soklaski, Y. Liang, L. Yang, *Phys. Rev. B* **2014**, *89*, 235319.
[22] G. Long, D. Maryenko, J. Shen, S. Xu, J. Hou, Z. Wu, W. K. Wong, T. Han, J. Lin, Y. Cai, R. Lortz, N. Wang, *Nano Lett.* **2016**, *16*, 7768.
[23] B. Radisavljevic, A. Radenovic, J. Brivio, V. Giacometti, A. Kis, *Nat. Nanotechnol.* **2011**, *6*, 147.
[24] N. Mao, J. Tang, L. Xie, J. Wu, B. Han, J. Lin, S. Deng, W. Ji, H. Xu, K. Liu, L. Tong, J. Zhang, *J. Am. Chem. Soc.* **2016**, *138*, 300.
[25] A. Favron, E. Gaufres, F. Fossard, A. L. Phaneuf L'Heureux, N. Y. W. Tang, P. L. Levesque, A. Loiseau, R. Leonelli, S. Francoeur, R. Martel, *Nat. Mater.* **2015**, *14*, 826.
[26] J. D. Wood, S. A. Wells, D. Jariwala, K. S. Chen, E. Cho, V. K. Sangwan, X. Liu, L. J. Lauhon, T. J. Marks, M. C. Hersam, *Nano Lett.* **2014**, *14*, 6964.
[27] T. Ahmed, S. Balendhran, M. N. Karim, E. L. H. Mayes, M. R. Field, R. Ramanathan, M. Singh, V. Bansal, S. Sriram, M. Bhaskaran, S. Walia, *NPJ 2D Mater. Appl.* **2017**, *1*, 18.
[28] F. Xia, H. Wang, J. C. M. Hwang, A. H. C. Neto, L. Yang, *Nat. Rev. Phys.* **2019**, *1*, 306.
[29] I. Pletikosic, F. von Rohr, P. Pervan, P. K. Das, I. Vobornik, R. J. Cava, T. Valla, *Phys. Rev. Lett.* **2018**, *120*, 156403.
[30] L. C. Gomes, A. Carvalho, A. H. Castro Neto, *Phys. Rev. B* **2016**, *94*, 054103.
[31] L. C. Gomes, A. Carvalho, *Phys. Rev. B* **2015**, *92*, 085406.
[32] Y. Guo, S. Zhou, Y. Bai, J. Zhao, *ACS Appl. Mater. Interfaces* **2017**, *9*, 12013.
[33] B. Liu, M. Niu, J. Fu, Z. Xi, M. Lei, R. Quhe, *Phys. Rev. Mater.* **2019**, *3*, 054002.
[34] J. R. Brent, D. J. Lewis, T. Lorenz, E. A. Lewis, N. Savjani, S. J. Haigh, G. Seifert, B. Derby, P. O'Brien, *J. Am. Chem. Soc.* **2015**, *137*, 12689.
[35] L. Xu, M. Yang, S. J. Wang, Y. P. Feng, *Phys. Rev. B* **2017**, *95*, 235434.
[36] S. Yang, Y. Liu, M. Wu, L. D. Zhao, Z. Lin, H. C. Cheng, Y. Wang, C. Jiang, S. H. Wei, L. Huang, Y. Huang, X. Duan, *Nano Res.* **2018**, *11*, 554.
[37] A. S. Rodin, L. C. Gomes, A. Carvalho, A. H. Castro Neto, *Phys. Rev. B* **2016**, *93*, 045431.
[38] T. Rangel, B. M. Fregoso, B. S. Mendoza, T. Morimoto, J. E. Moore, J. B. Neaton, *Phys. Rev. Lett.* **2017**, *119*, 067402.
[39] P. Z. Hanakata, A. Carvalho, D. K. Campbell, H. S. Park, *Phys. Rev. B* **2016**, *94*, 035304.
[40] B. R. Tuttle, S. M. Alhassan, S. T. Pantelides, *Phys. Rev. B* **2015**, *92*, 235405.
[41] P. Zhao, H. Yang, J. Li, H. Jin, W. Wei, L. Yu, B. Huang, Y. Dai, *J. Mater. Chem. A* **2017**, *5*, 24145.
[42] G. Michael, G. Hu, D. Zheng, Y. Zhang, *J. Phys. D: Appl. Phys.* **2019**, *52*, 204001.
[43] R. Fei, W. Li, J. Li, L. Yang, *Appl. Phys. Lett.* **2015**, *107*, 173104.
[44] R. Fei, W. Kang, L. Yang, *Phys. Rev. Lett.* **2016**, *117*, 097601.
[45] S. R. Panday, S. Barraza-Lopez, T. Rangel, B. M. Fregoso, *Phys. Rev. B* **2019**, *100*, 195305.
[46] Y. Bao, P. Song, Y. Liu, Z. Chen, M. Zhu, I. Abdelwahab, J. Su, W. Fu, X. Chi, W. Yu, W. Liu, X. Zhao, Q.-H. Xu, M. Yang, K. P. Loh, *Nano Lett.* **2019**, *19*, 5109.
[47] J. J. Zhang, J. Guan, S. Dong, B. I. Yakobson, *J. Am. Chem. Soc.* **2019**, *141*, 15040.
[48] H. Wang, X. Qian, *2D Mater.* **2017**, *4*, 015042.
[49] M. Wu, X. C. Zeng, *Nano Lett.* **2016**, *16*, 3236.
[50] C. Chen, X. Chen, Y. Shao, B. Deng, Q. Guo, C. Ma, F. Xia, *ACS Photonics* **2018**, *5*, 3814.
[51] S. Lin, A. Carvalho, S. Yan, R. Li, S. Kim, A. Rodin, L. Carvalho, E. M. Chan, X. Wang, A. H. Castro Neto, J. Yao, *Nat. Commun.* **2018**, *9*, 1455.
[52] H. Wang, X. Qian, *Nano Lett.* **2017**, *17*, 5027.
[53] A. I. Lebedev, *J. Appl. Phys.* **2018**, *124*, 164302.
[54] I. Lefebvre, M. A. Szymanski, J. O. Fourcade, J. C. Jumas, *Phys. Rev. B* **1998**, *58*, 1896.
[55] L. C. Zhang, G. Qin, W. Z. Fang, H. J. Cui, Q. R. Zheng, Q. B. Yan, G. Su, *Sci. Rep.* **2016**, *6*, 19830.
[56] H. Y. Song, J. T. Lu, *Chem. Phys. Lett.* **2018**, *695*, 200.
[57] N. Higashitarumizu, H. Kawamoto, M. Nakamura, K. Shimamura, N. Ohashi, K. Ueno, K. Nagashio, *Nanoscale* **2018**, *10*, 22474.
[58] J. Vidal, S. Lany, M. daAvezac, A. Zunger, A. Zakutayev, J. Francis, J. Tate, *Appl. Phys. Lett.* **2012**, *100*, 032104.
[59] U. V. Waghmare, N. A. Spaldin, H. C. Kandpal, R. Seshadri, *Phys. Rev. B* **2003**, *67*, 125111.

© 2020 The Authors. Published by Wiley-VCH GmbH

[60] A. Walsh, G. W. Watson, *J. Phys. Chem. B* **2005**, *109*, 18868.
[61] W. Shi, M. Gao, J. Wei, J. Gao, C. Fan, E. Ashalley, H. Li, Z. Wang, *Adv. Sci.* **2018**, *5*, 1700602.
[62] J. H. Yang, Y. Zhang, W. J. Yin, X. G. Gong, B. I. Yakobson, S. H. Wei, *Nano Lett.* **2016**, *16*, 1110.
[63] H. Jiang, T. Zhao, Y. Ren, R. Zhang, M. Wu, *Sci. Bull.* **2017**, *62*, 572.
[64] S. Karmakar, C. Chowdhury, A. Datta, *J. Phys. Chem. C* **2016**, *120*, 14522.
[65] L. Shi, Y. Dai, *J. Appl. Crystallogr.* **2014**, *47*, 527.
[66] R. K. Ulaganathan, Y. Y. Lu, C. J. Kuo, S. R. Tamalampudi, R. Sankar, K. M. Boopathi, A. Anand, K. Yadav, R. J. Mathew, C. R. Liu, F. C. Chou, Y. T. Chen, *Nanoscale* **2016**, *8*, 2284.
[67] L. H. Levy, *J. Appl. Behav. Sci.* **1976**, *12*, 310.
[68] B. Mukherjee, Y. Cai, H. R. Tan, Y. P. Feng, E. S. Tok, C. H. Sow, *ACS Appl. Mater. Interfaces* **2013**, *5*, 9594.
[69] D. J. Xue, J. Tan, J. S. Hu, W. Hu, Y. G. Guo, L. J. Wan, *Adv. Mater.* **2012**, *24*, 4528.
[70] J. Xia, X. Z. Li, X. Huang, N. Mao, D. D. Zhu, L. Wang, H. Xu, X. M. Meng, *Nanoscale* **2016**, *8*, 2063.
[71] Z. Shi, Z. Zhang, A. Kutana, B. I. Yakobson, *ACS Nano* **2015**, *9*, 9802.
[72] L. D. Zhao, S. H. Lo, Y. Zhang, H. Sun, G. Tan, C. Uher, C. Wolverton, V. P. Dravid, M. G. Kanatzidis, *Nature* **2014**, *508*, 373.
[73] J. Qiao, X. Kong, Z. X. Hu, F. Yang, W. Ji, *Nat. Commun.* **2014**, *5*, 4475.
[74] X. Wang, A. M. Jones, K. L. Seyler, V. Tran, Y. Jia, H. Zhao, H. Wang, L. Yang, X. Xu, F. Xia, *Nat. Nanotechnol.* **2015**, *10*, 517.
[75] J. Tao, W. Shen, S. Wu, L. Liu, Z. Feng, C. Wang, C. Hu, P. Yao, H. Zhang, W. Pang, X. Duan, J. Liu, C. Zhou, D. Zhang, *ACS Nano* **2015**, *9*, 11362.
[76] Y. Zhao, G. Zhang, M. H. Nai, G. Ding, D. Li, Y. Liu, K. Hippalgaonkar, C. T. Lim, D. Chi, B. Li, J. Wu, J. T. L. Thong, *Adv. Mater.* **2018**, *30*, 1804928.
[77] L. Li, W. Han, L. Pi, P. Niu, J. Han, C. Wang, B. Su, H. Li, J. Xiong, Y. Bando, T. Zhai, *InfoMat* **2019**, *1*, 54.
[78] E. Chatzikyriakou, J. Kioseoglou, *Nanoscale Adv.* **2019**, *1*, 4863.
[79] Z. Zhu, J. Guan, D. Liu, D. Tomanek, *ACS Nano* **2015**, *9*, 8284.
[80] Y. C. Huang, X. Chen, C. Wang, L. Peng, Q. Qian, S. F. Wang, *Nanoscale* **2017**, *9*, 8616.
[81] C. Wang, L. Peng, Q. Qian, J. Du, S. Wang, Y. Huang, *Small* **2018**, *14*, 1703536.
[82] J. H. Yang, X. G. Gong, *J. Mater. Chem. C* **2019**, *7*, 11858.
[83] K. Kosmider, J. W. Gonzalez, J. F. Rossier, *Phys. Rev. B* **2013**, *88*, 245436.
[84] M. Zhou, X. Chen, M. Li, A. Du, *J. Mater. Chem. C* **2017**, *5*, 1247.
[85] U. Argaman, R. E. Abutbul, Y. Golan, G. Makov, *Phys. Rev. B* **2019**, *100*, 054104.
[86] T. Barik, J. D. Sau, *Phys. Rev. B* **2020**, *101*, 045201.
[87] X. Lv, W. Wei, Q. Sun, F. Li, B. Huang, Y. Dai, *Appl. Catal., B* **2017**, *217*, 275.
[88] N. Makori, I. Amatalo, P. Karimi, W. Njoroge, *Am. J. Condens. Matter Phys.* **2014**, *4*, 87.
[89] P. Sinsermsuksakul, J. Heo, W. Noh, A. S. Hock, R. G. Gordon, *Adv. Energy Mater.* **2011**, *1*, 1116.
[90] L. C. Gomes, A. Carvalho, A. H. Castro Neto, *Phys. Rev. B* **2015**, *92*, 214103.
[91] A. J. Mannix, B. Kiraly, M. C. Hersam, N. P. Guisinger, *Nat. Rev. Chem.* **2017**, *1*, 0014.
[92] D. Wang, F. Luo, M. Lu, X. Xie, L. Huang, W. Huang, *Small* **2019**, *15*, 1804404.
[93] P. Tao, S. Yao, F. Liu, B. Wang, F. Huang, M. Wang, *J. Mater. Chem. A* **2019**, *7*, 23512.
[94] H. Li, J. Wu, Z. Yin, H. Zhang, *Acc. Chem. Res.* **2014**, *47*, 1067.
[95] K. S. Novoselov, A. Mishchenko, A. Carvalho, A. H. Castro Neto, *Science* **2016**, *353*, aac9439.
[96] N. Zhang, A. Surrente, M. Baranowski, D. K. Maude, P. Gant, A. Castellanos-Gomez, P. Plochocka, *Nano Lett.* **2018**, *18*, 7651.
[97] R. Frisenda, E. Navarro-Moratalla, P. Gant, D. Perez De Lara, P. Jarillo-Herrero, R. V. Gorbachev, A. Castellanos-Gomez, *Chem. Soc. Rev.* **2018**, *47*, 53.
[98] C. H. Ho, J. X. Li, *Adv. Opt. Mater.* **2017**, *5*, 1600814.
[99] H. C. Hsueh, J. X. Li, C. H. Ho, *Adv. Opt. Mater.* **2018**, *6*, 1701194.
[100] Z. Li, Y. Yang, X. Wang, W. Shi, D. J. Xue, J. S. Hu, *ACS Appl. Mater. Interfaces* **2019**, *11*, 24247.
[101] D. Tan, X. Wang, W. Zhang, H. E. Lim, K. Shinokita, Y. Miyauchi, M. Maruyama, S. Okada, K. Matsuda, *Small* **2018**, *14*, 1704559.
[102] W. C. Yap, Z. Yang, M. Mehboudi, J. A. Yan, S. Barraza Lopez, W. Zhu, *Nano Res.* **2018**, *11*, 420.
[103] Y. Yang, S. C. Liu, Y. Wang, M. Long, C.-M. Dai, S. Chen, B. Zhang, Z. Sun, Z. Sun, C. Hu, S. Zhang, L. Tong, G. Zhang, D. J. Xue, J. S. Hu, *Adv. Opt. Mater.* **2019**, *7*, 1801311.
[104] S. Sucharitakul, U. R. Kumar, R. Sankar, F. C. Chou, Y. T. Chen, C. Wang, C. He, R. He, X. P. A. Gao, *Nanoscale* **2016**, *8*, 19050.
[105] S. H. Cho, K. Cho, N. W. Park, S. Park, J. H. Koh, S. K. Lee, *Nanoscale Res. Lett.* **2017**, *12*, 373.
[106] Z. Wang, C. Fan, Z. Shen, C. Hua, Q. Hu, F. Sheng, Y. Lu, H. Fang, Z. Qiu, J. Lu, Z. Liu, W. Liu, Y. Huang, Z. A. Xu, D. W. Shen, Y. Zheng, *Nat. Commun.* **2018**, *9*, 47.
[107] D. Tan, H. E. Lim, F. Wang, N. B. Mohamed, S. Mouri, W. Zhang, Y. Miyauchi, M. Ohfuchi, K. Matsuda, *Nano Res.* **2017**, *10*, 546.
[108] X. Zhang, Q. H. Tan, J. B. Wu, W. Shi, P. H. Tan, *Nanoscale* **2016**, *8*, 6435.
[109] S. Zhang, N. Zhang, Y. Zhao, T. Cheng, X. Li, R. Feng, H. Xu, Z. Liu, J. Zhang, L. Tong, *Chem. Soc. Rev.* **2018**, *47*, 3217.
[110] A. S. Sarkar, A. Mushtaq, D. Kushavah, S. K. Pal, *NPJ 2D Mater. Appl.* **2020**, *4*, 1.
[111] H. R. Chandrasekhar, U. Zwick, *Solid State Commun.* **1976**, *18*, 1509.
[112] T. Fukunaga, S. Sugai, T. Kinosada, K. Murase, *Solid State Commun.* **1981**, *38*, 1049.
[113] X. Wang, Y. Li, L. Huang, X. W. Jiang, L. Jiang, H. Dong, Z. Wei, J. Li, W. Hu, *J. Am. Chem. Soc.* **2017**, *139*, 14976.
[114] A. Castellanos-Gomez, L. Vicarelli, E. Prada, J. O. Island, K. L. Narasimha-Acharya, S. I. Blanter, D. J. Groenendijk, M. Buscema, G. A. Steele, J. V. Alvarez, H. W. Zandbergen, J. J. Palacios, H. S. J. van der Zant, *2D Mater.* **2014**, *1*, 025001.
[115] S. Liu, N. Huo, S. Gan, Y. Li, Z. Wei, B. Huang, J. Liu, J. Li, H. Chen, *J. Mater. Chem. C* **2015**, *3*, 10974.
[116] Z. Guo, H. Zhang, S. Lu, Z. Wang, S. Tang, J. Shao, Z. Sun, H. Xie, H. Wang, X. F. Yu, P. K. Chu, *Adv. Funct. Mater.* **2015**, *25*, 6996.
[117] C. Zhang, H. Ouyang, R. Miao, Y. Sui, H. Hao, Y. Tang, J. You, X. Zheng, Z. Xu, X. Cheng, T. Jiang, *Adv. Opt. Mater.* **2019**, *7*, 1900631.
[118] N. Higashitarumizu, H. Kawamoto, K. Ueno, K. Nagashio, *MRS Adv.* **2018**, *3*, 2809.
[119] X. Wang, F. Xia, *Nat. Mater.* **2015**, *14*, 264.
[120] V. O. Ozcelik, M. Fathi, J. G. Azadani, T. Low, *Phys. Rev. Mater.* **2018**, *2*, 051003.
[121] W. Yang, H. Kawai, M. Bosman, B. Tang, J. Chai, W. L. Tay, J. Yang, H. L. Seng, H. Zhu, H. Gong, H. Liu, K. E. J. Goh, S. Wang, D. Chi, *Nanoscale* **2018**, *10*, 22927.
[122] D. Rhodes, S. H. Chae, R. Ribeiro-Palau, J. Hone, *Nat. Mater.* **2019**, *18*, 541.
[123] W. Tremel, R. Hoffmann, *Inorg. Chem.* **1987**, *26*, 118.
[124] M. Li, Y. Wu, T. Li, Y. Chen, H. Ding, Y. Lin, N. Pan, X. Wang, *RSC Adv.* **2017**, *7*, 48759.
[125] S. Yang, M. Wu, B. Wang, L. D. Zhao, L. Huang, C. Jiang, S. H. Wei, *ACS Appl. Mater. Interfaces* **2017**, *9*, 42149.
[126] D. D. Vaughn, S. I. In, R. E. Schaak, *ACS Nano* **2011**, *5*, 8852.
[127] J. Wu, N. Mao, L. Xie, H. Xu, J. Zhang, *Angew. Chem., Int. Ed.* **2015**, *54*, 2366.

© 2020 The Authors. Published by Wiley-VCH GmbH

[128] S. Huang, Y. Tatsumi, X. Ling, H. Guo, Z. Wang, G. Watson, A. A. Puretzky, D. B. Geohegan, J. Kong, J. Li, T. Yang, R. Saito, M. S. Dresselhaus, *ACS Nano* **2016**, *10*, 8964.
[129] X. Ling, S. Huang, E. H. Hasdeo, L. Liang, W. M. Parkin, Y. Tatsumi, A. R. T. Nugraha, A. A. Puretzky, P. M. Das, B. G. Sumpter, D. B. Geohegan, J. Kong, R. Saito, M. Drndic, V. Meunier, M. S. Dresselhaus, *Nano Lett.* **2016**, *16*, 2260.
[130] Y. Zhao, D. Yu, J. Lu, L. Tao, Z. Chen, Y. Yang, A. Wei, L. Tao, J. Liu, Z. Zheng, M. Hao, J. B. Xu, *Adv. Opt. Mater.* **2019**, *7*, 1901085.
[131] M. Hafeez, L. Gan, H. Li, Y. Ma, T. Zhai, *Adv. Mater.* **2016**, *28*, 8296.
[132] Y. Hernandez, V. Nicolosi, M. Lotya, F. M. Blighe, Z. Sun, S. De, I. T. McGovern, B. Holland, M. Byrne, Y. K. Gun'Ko, J. J. Boland, P. Niraj, G. Duesberg, S. Krishnamurthy, R. Goodhue, J. Hutchison, V. Scardaci, A. C. Ferrari, J. N. Coleman, *Nat. Nanotechnol.* **2008**, *3*, 563.
[133] K. R. Paton, E. Varrla, C. Backes, R. J. Smith, U. Khan, A. O'Neill, C. Boland, M. Lotya, O. M. Istrate, P. King, T. Higgins, S. Barwich, P. May, P. Puczkarski, I. Ahmed, M. Moebius, H. Pettersson, E. Long, J. Coelho, S. E. O'Brien, E. K. McGuire, B. M. Sanchez, G. S. Duesberg, N. McEvoy, T. J. Pennycook, C. Downing, A. Crossley, V. Nicolosi, J. N. Coleman, *Nat. Mater.* **2014**, *13*, 624.
[134] J. Kang, V. K. Sangwan, J. D. Wood, M. C. Hersam, *Acc. Chem. Res.* **2017**, *50*, 943.
[135] J. N. Coleman, M. Lotya, A. O'Neill, S. D. Bergin, P. J. King, U. Khan, K. Young, A. Gaucher, S. De, R. J. Smith, I. V. Shvets, S. K. Arora, G. Stanton, H. Y. Kim, K. Lee, G. T. Kim, G. S. Duesberg, T. Hallam, J. J. Boland, J. J. Wang, J. F. Donegan, J. C. Grunlan, G. Moriarty, A. Shmeliov, R. J. Nicholls, J. M. Perkins, E. M. Grieveson, K. Theuwissen, D. W. McComb, P. D. Nellist, V. Nicolosi, *Science* **2011**, *331*, 568.
[136] Y. Hernandez, M. Lotya, D. Rickard, S. D. Bergin, J. N. Coleman, *Langmuir* **2010**, *26*, 3208.
[137] J. Shen, Y. He, J. Wu, C. Gao, K. Keyshar, X. Zhang, Y. Yang, M. Ye, R. Vajtai, J. Lou, P. M. Ajayan, *Nano Lett.* **2015**, *15*, 5449.
[138] G. Cunningham, M. Lotya, C. S. Cucinotta, S. Sanvito, S. D. Bergin, R. Menzel, M. S. P. Shaffer, J. N. Coleman, *ACS Nano* **2012**, *6*, 3468.
[139] S. P. Ogilvie, M. J. Large, M. A. O'Mara, P. J. Lynch, C. L. Lee, A. A. K. King, C. Backes, A. B. Dalton, *2D Mater.* **2019**, *6*, 031002.
[140] D. Lam, K. S. Chen, J. Kang, X. Liu, M. C. Hersam, *Chem. Mater.* **2018**, *30*, 2245.
[141] Y. Ye, Q. Guo, X. Liu, C. Liu, J. Wang, Y. Liu, J. Qiu, *Chem. Mater.* **2017**, *29*, 8361.
[142] D. Ma, J. Zhao, R. Wang, C. Xing, Z. Li, W. Huang, X. Jiang, Z. Guo, Z. Luo, Y. Li, J. Li, S. Luo, Y. Zhang, H. Zhang, *ACS Appl. Mater. Interfaces* **2019**, *11*, 4278.
[143] X. Fan, L. Su, F. Zhang, D. Huang, D. K. Sang, Y. Chen, Y. Li, F. Liu, J. Li, H. Zhang, H. Xie, *ACS Appl. Mater. Interfaces* **2019**, *11*, 47197.
[144] W. Huang, Z. Xie, T. Fan, J. Li, Y. Wang, L. Wu, D. Ma, Z. Li, Y. Ge, Z. N. Huang, X. Dai, Y. Xiang, J. Li, X. Zhu, H. Zhang, *J. Mater. Chem. C* **2018**, *6*, 9582.
[145] Z. Xie, F. Zhang, Z. Liang, T. Fan, Z. Li, X. Jiang, H. Chen, J. Li, H. Zhang, *Photonics Res.* **2019**, *7*, 494.
[146] Z. Xie, D. Wang, T. Fan, C. Xing, Z. Li, W. Tao, L. Liu, S. Bao, D. Fan, H. Zhang, *J. Mater. Chem. B* **2018**, *6*, 4747.
[147] A. Jannat, F. Haque, K. Xu, C. Zhou, B. Y. Zhang, N. Syed, M. Mohiuddin, K. A. Messalea, X. Li, S. L. Gras, X. Wen, Z. Fei, E. Haque, S. Walia, T. Daeneke, A. Zavabeti, J. Z. Ou, *ACS Appl. Mater. Interfaces* **2019**, *11*, 42462.
[148] Y. Huang, L. Li, Y. H. Lin, C. W. Nan, *J. Phys. Chem. C* **2017**, *121*, 17530.
[149] Y. Ye, Y. Xian, J. Cai, K. Lu, Z. Liu, T. Shi, J. Du, Y. Leng, R. Wei, W. Wang, X. Liu, G. Bi, J. Qiu, *Adv. Opt. Mater.* **2019**, *7*, 1800579.
[150] D. D. Vaughn, R. J. Patel, M. A. Hickner, R. E. Schaak, *J. Am. Chem. Soc.* **2010**, *132*, 15170.
[151] Y. Hu, S. Zhang, S. Sun, M. Xie, B. Cai, H. Zeng, *Appl. Phys. Lett.* **2015**, *107*, 122107.
[152] H. Zhao, Y. Mao, X. Mao, X. Shi, C. Xu, C. Wang, S. Zhang, D. Zhou, *Adv. Funct. Mater.* **2018**, *28*, 1704855.
[153] C. Backes, B. M. Szydlowska, A. Harvey, S. Yuan, V. V. Mayoral, B. R. Davies, P.-L. Zhao, D. Hanlon, E. J. G. Santos, M. I. Katsnelson, W. J. Blau, C. Gadermaier, J. N. Coleman, *ACS Nano* **2016**, *10*, 1589.
[154] A. Harvey, X. He, I. J. Godwin, C. Backes, D. McAteer, N. C. Berner, N. McEvoy, A. Ferguson, A. Shmeliov, M. E. G. Lyons, V. Nicolosi, G. S. Duesberg, J. F. Donegan, J. N. Coleman, *J. Mater. Chem. A* **2016**, *4*, 11046.
[155] H. Ju, J. Kim, *ACS Nano* **2016**, *10*, 5730.
[156] R. Lv, J. A. Robinson, R. E. Schaak, D. Sun, Y. Sun, T. E. Mallouk, M. Terrones, *Acc. Chem. Res.* **2015**, *48*, 56.
[157] Y. Zhang, Y. Yao, M. G. Sendeku, L. Yin, X. Zhan, F. Wang, Z. Wang, J. He, *Adv. Mater.* **2019**, *31*, 1901694.
[158] A. Zafar, Z. Zafar, W. Zhao, J. Jiang, Y. Zhang, Y. Chen, J. Lu, Z. Ni, *Adv. Funct. Mater.* **2019**, *29*, 1809261.
[159] E. Sutter, B. Zhang, M. Sun, P. Sutter, *ACS Nano* **2019**, *13*, 9352.
[160] S. M. Yoon, H. J. Song, H. C. Choi, *Adv. Mater.* **2010**, *22*, 2164.
[161] H. Zhang, Y. Balaji, A. N. Mehta, M. Heyns, M. Caymax, I. Radu, W. Vandervorst, A. Delabie, *J. Mater. Chem. C* **2018**, *6*, 6172.
[162] P. Sutter, E. Sutter, *ACS Appl. Nano Mater.* **2018**, *1*, 3026.
[163] S. Zhao, H. Wang, Y. Zhou, L. Liao, Y. Jiang, X. Yang, G. Chen, M. Lin, Y. Wang, H. Peng, Z. Liu, *Nano Res.* **2015**, *8*, 288.
[164] X. Xu, Q. Song, H. Wang, P. Li, K. Zhang, Y. Wang, K. Yuan, Z. Yang, Y. Ye, L. Dai, *ACS Appl. Mater. Interfaces* **2017**, *9*, 12601.
[165] S. Liu, N. Sun, M. Liu, S. Sucharitakul, X. P. A. Gao, *J. Appl. Phys.* **2018**, *123*, 115109.
[166] X. Hu, P. Huang, K. Liu, B. Jin, X. Zhang, X. Zhang, X. Zhou, T. Zhai, *ACS Appl. Mater. Interfaces* **2019**, *11*, 23353.
[167] A. C. Ferrari, D. M. Basko, *Nat. Nanotechnol.* **2013**, *8*, 235.
[168] S. Lei, L. Ge, Z. Liu, S. Najmaei, G. Shi, G. You, J. Lou, R. Vajtai, P. M. Ajayan, *Nano Lett.* **2013**, *13*, 2777.
[169] Y. H. Lee, X. Q. Zhang, W. Zhang, M. T. Chang, C. T. Lin, K. D. Chang, Y. C. Yu, J. T. W. Wang, C. S. Chang, L. J. Li, T. W. Lin, *Adv. Mater.* **2012**, *24*, 2320.
[170] S. Najmaei, Z. Liu, W. Zhou, X. Zou, G. Shi, S. Lei, B. I. Yakobson, J. C. Idrobo, P. M. Ajayan, J. Lou, *Nat. Mater.* **2013**, *12*, 754.
[171] Q. Feng, N. Mao, J. Wu, H. Xu, C. Wang, J. Zhang, L. Xie, *ACS Nano* **2015**, *9*, 7450.
[172] Z. Tian, C. Guo, M. Zhao, R. Li, J. Xue, *ACS Nano* **2017**, *11*, 2219.
[173] A. Wangperawong, S. M. Herron, R. R. Runser, C. Hagglund, J. T. Tanskanen, H. B. R. Lee, B. M. Clemens, S. F. Bent, *Appl. Phys. Lett.* **2013**, *103*, 052105.
[174] R. Guo, X. Wang, Y. Kuang, B. Huang, *Phys. Rev. B* **2015**, *92*, 115202.
[175] R. Car, G. Ciucci, L. Quartapelle, *Phys. Status Solidi B* **1978**, *86*, 471.
[176] H. R. Chandrasekhar, R. G. Humphreys, U. Zwick, M. Cardona, *Phys. Rev. B* **1977**, *15*, 2177.
[177] X. H. Ma, K. H. Cho, Y. M. Sung, *CrystEngComm* **2014**, *16*, 5080.
[178] Z. Wang, F. Pang, *Chem. Phys. Lett.* **2018**, *702*, 90.
[179] N. D. Boscher, C. J. Carmalt, R. G. Palgrave, I. P. Parkin, *Thin Solid Films* **2008**, *516*, 4750.
[180] Y. Huang, K. Xu, Z. Wang, T. A. Shifa, Q. Wang, F. Wang, C. Jiang, J. He, *Nanoscale* **2015**, *7*, 17375.
[181] H. Khan, N. Mahmood, A. Zavabeti, A. Elbourne, M. A. Rahman, B. Y. Zhang, V. Krishnamurthi, P. Atkin, M. B. Ghasemian, J. Yang, G. Zheng, A. R. Ravindran, S. Walia, L. Wang, S. P. Russo, T. Daeneke, Y. Li, K. Kalantar-Zadeh, *Nat. Commun.* **2020**, *11*, 3449.
[182] F. Li, M. M. R. Moayed, E. Klein, R. Lesyuk, C. Klinke, *J. Phys. Chem. Lett.* **2019**, *10*, 993.
[183] A. J. Biacchi, S. T. Le, B. G. Alberding, J. A. Hagmann, S. J. Pookpanratana, E. J. Heilweil, C. A. Richter, A. R. H. Walker, *ACS Nano* **2018**, *12*, 10045.

© 2020 The Authors. Published by Wiley-VCH GmbH

[184] L. Li, Z. Chen, Y. Hu, X. Wang, T. Zhang, W. Chen, Q. Wang, *J. Am. Chem. Soc.* **2013**, *135*, 1213.
[185] C. Wang, G. Zhang, S. Huang, Y. Xie, H. Yan, *Adv. Opt. Mater.* **2019**, 1900996.
[186] Z. Li, X. Wang, S. C. Liu, W. Shi, X. Xing, D. J. Xue, J. S. Hu, *J. Appl. Phys.* **2019**, *125*, 082524.
[187] D. Tan, W. Zhang, X. Wang, S. Koirala, Y. Miyauchi, K. Matsuda, *Nanoscale* **2017**, *9*, 12425.
[188] X. Zhou, X. Hu, B. Jin, J. Yu, K. Liu, H. Li, T. Zhai, *Adv. Sci.* **2018**, *5*, 1800478.
[189] X. Zhou, Q. Zhang, L. Gan, H. Li, T. Zhai, *Adv. Funct. Mater.* **2016**, *26*, 4405.
[190] B. Li, T. Xing, M. Zhong, L. Huang, N. Lei, J. Zhang, J. Li, Z. Wei, *Nat. Commun.* **2017**, *8*, 1958.
[191] X. Zhou, L. Gan, W. Tian, Q. Zhang, S. Jin, H. Li, Y. Bando, D. Golberg, T. Zhai, *Adv. Mater.* **2015**, *27*, 8035.
[192] Y. Xu, H. Zhang, H. Shao, G. Ni, J. Li, H. Lu, R. Zhang, B. Peng, Y. Zhu, H. Zhu, C. M. Soukoulis, *Phys. Rev. B* **2017**, *96*, 245421.
[193] J. Liu, Y. Zhou, Y. Lin, M. Li, H. Cai, Y. Liang, M. Liu, Z. Huang, F. Lai, F. Huang, W. Zheng, *ACS Appl. Mater. Interfaces* **2019**, *11*, 4123.
[194] E. Liu, Y. Fu, Y. Wang, Y. Feng, H. Liu, X. Wan, W. Zhou, B. Wang, L. Shao, C. H. Ho, Y. S. Huang, Z. Cao, L. Wang, A. Li, J. Zeng, F. Song, X. Wang, Y. Shi, H. Yuan, H. Y. Hwang, Y. Cui, F. Miao, D. Xing, *Nat. Commun.* **2015**, *6*, 6991.
[195] S. Das, M. Demarteau, A. Roelofs, *ACS Nano* **2014**, *8*, 11730.
[196] M. Xie, S. Zhang, B. Cai, Y. Huang, Y. Zou, B. Guo, Y. Gu, H. Zeng, *Nano Energy* **2016**, *28*, 433.
[197] M. L. Tsai, S. H. Su, J. K. Chang, D. S. Tsai, C. H. Chen, C. I. Wu, L. J. Li, L. J. Chen, J. H. He, *ACS Nano* **2014**, *8*, 8317.
[198] E. Kymakis, *Adv. Mater. Interfaces* **2018**, *5*, 1801595.
[199] M. M. Stylianakis, D. Konios, C. Petridis, G. Kakavelakis, E. Stratakis, E. Kymakis, *2D Mater.* **2017**, *4*, 042005.
[200] G. Kakavelakis, E. Kymakis, K. Petridis, *Adv. Mater. Interfaces* **2018**, *5*, 1800339.
[201] A. S. Sarkar, S. K. Pal, *J. Phys. Chem. C* **2017**, *121*, 21945.
[202] A. S. Sarkar, A. D. Rao, A. K. Jagdish, A. Gupta, C. K. Nandi, P. C. Ramamurthy, S. K. Pal, *Org. Electron.* **2018**, *54*, 148.
[203] R. Ray, A. S. Sarkar, S. K. Pal, *Sol. Energy* **2019**, *193*, 95.
[204] A. Mushtaq, S. Ghosh, A. S. Sarkar, S. K. Pal, *ACS Energy Lett.* **2017**, *2*, 1879.
[205] R. Von Baltz, W. Kraut, *Phys. Rev. B* **1981**, *23*, 5590.
[206] M. Bernardi, M. Palummo, J. C. Grossman, *Nano Lett.* **2013**, *13*, 3664.
[207] G. Shi, E. Kioupakis, *Nano Lett.* **2015**, *15*, 6926.
[208] B. Ul Haq, S. AlFaify, R. Ahmed, F. K. Butt, A. Laref, M. Shkir, *Phys. Rev. B* **2018**, *97*, 075438.
[209] C. Xia, J. Du, W. Xiong, Y. Jia, Z. Wei, J. Li, *J. Mater. Chem. A* **2017**, *5*, 13400.
[210] C. He, M. Cheng, T. Li, W. Zhang, *ACS Appl. Nano Mater.* **2019**, *2*, 2767.
[211] D. J. Xue, S. C. Liu, C. M. Dai, S. Chen, C. He, L. Zhao, J. S. Hu, L. J. Wan, *J. Am. Chem. Soc.* **2017**, *139*, 958.
[212] K. Kushnir, Y. Qin, Y. Shen, G. Li, B. M. Fregoso, S. Tongay, L. V. Titova, *ACS Appl. Mater. Interfaces* **2019**, *11*, 5492.
[213] Z. Jiang, Z. Liu, Y. Li, W. Duan, *Phys. Rev. Lett.* **2017**, *118*, 266401.
[214] R. Frindt, A. Yoffe, *Proc. R. Soc. London, Ser. A* **1963**, *273*, 69.
[215] B. Radisavljevic, M. B. Whitwick, A. Kis, *ACS Nano* **2011**, *5*, 9934.
[216] Y. Yao, L. Tolentino, Z. Yang, X. Song, W. Zhang, Y. Chen, C. P. Wong, *Adv. Funct. Mater.* **2013**, *23*, 3577.
[217] A. M. Cook, B. M. Fregoso, F. de Juan, S. Coh, J. E. Moore, *Nat. Commun.* **2017**, *8*, 14176.
[218] E. Kutlu, P. Narin, S. B. Lisesivdin, E. Ozbay, *Philos. Mag.* **2018**, *98*, 155.
[219] X. Lv, W. Wei, C. Mu, B. Huang, Y. Dai, *J. Mater. Chem. A* **2018**, *6*, 5032.
[220] J. Zhao, Y. Li, G. Yang, K. Jiang, H. Lin, H. Ade, W. Ma, H. Yan, *Nat. Energy* **2016**, *1*, 15027.
[221] J. Dai, X. C. Zeng, *J. Phys. Chem. Lett.* **2014**, *5*, 1289.
[222] L. J. Zhou, Y. F. Zhang, L. M. Wu, *Nano Lett.* **2013**, *13*, 5431.
[223] D. D. Tune, N. Mallik, H. Fornasier, B. S. Flavel, *Adv. Energy Mater.* **2020**, *10*, 1903261.
[224] G. J. Hou, D. L. Wang, R. Ali, Y. R. Zhou, Z. G. Zhu, G. Su, *Sol. Energy* **2018**, *159*, 142.
[225] Y. Ji, M. Yang, H. Dong, T. Hou, L. Wang, Y. Li, *Nanoscale* **2017**, *9*, 8608.
[226] C. Chowdhury, S. Karmakar, A. Datta, *J. Phys. Chem. C* **2017**, *121*, 7615.
[227] Y. Ji, H. Dong, M. Yang, T. Hou, Y. Li, *Phys. Chem. Chem. Phys.* **2017**, *19*, 20457.
[228] H. T. T. Nguyen, T. V. Vu, N. T. T. Binh, D. M. Hoat, N. V. Hieu, N. T. T. Anh, C. V. Nguyen, H. V. Phuc, H. R. Jappor, M. M. Obeid, N. N. Hieu, *Chem. Phys.* **2020**, *529*, 110543.
[229] K. Maeda, K. Domen, *J. Phys. Chem. Lett.* **2010**, *1*, 2655.
[230] P. Zhang, J. Zhang, J. Gong, *Chem. Soc. Rev.* **2014**, *43*, 4395.
[231] J. R. Schaibley, H. Yu, G. Clark, P. Rivera, J. S. Ross, K. L. Seyler, W. Yao, X. Xu, *Nat. Rev. Mater.* **2016**, *1*, 16055.
[232] V. H. Nguyen, S. Dechamps, P. Dollfus, J. C. Charlier, *Phys. Rev. Lett.* **2016**, *117*, 247702.
[233] S. A. Vitale, D. Nezich, J. O. Varghese, P. Kim, N. Gedik, P. Jarillo-Herrero, D. Xiao, M. Rothschild, *Small* **2018**, *14*, 1801483.
[234] Z. M. Yu, S. Guan, X. L. Sheng, W. Gao, S. A. Yang, *Phys. Rev. Lett.* **2020**, *124*, 037701.
[235] W. Y. Tong, C. G. Duan, *NPJ Quantum Mater.* **2017**, *2*, 47.
[236] K. F. Mak, K. He, J. Shan, T. F. Heinz, *Nat. Nanotechnol.* **2012**, *7*, 494.
[237] H. Zeng, J. Dai, W. Yao, D. Xiao, X. Cui, *Nat. Nanotechnol.* **2012**, *7*, 490.
[238] Y. Ye, J. Xiao, H. Wang, Z. Ye, H. Zhu, M. Zhao, Y. Wang, J. Zhao, X. Yin, X. Zhang, *Nat. Nanotechnol.* **2016**, *11*, 598.
[239] B. D. Malone, E. Kaxiras, *Phys. Rev. B* **2013**, *87*, 245312.
[240] Y. R. Shen, *Nature* **1989**, *337*, 519.
[241] P. C. Ray, *Chem. Rev.* **2010**, *110*, 5332.
[242] X. Zhuang, P. B. Miranda, D. Kim, Y. R. Shen, *Phys. Rev. B* **1999**, *59*, 12632.
[243] M. J. Miller, S. H. Wei, I. Parker, M. D. Cahalan, *Science* **2002**, *296*, 1869.
[244] L. M. Malard, T. V. Alencar, A. P. M. Barboza, K. F. Mak, A. M. de Paula, *Phys. Rev. B* **2013**, *87*, 201401.
[245] D. H. Kim, D. Lim, *J. Korean Phys. Soc.* **2015**, *66*, 816.
[246] H. Chen, V. Corboliou, A. S. Solntsev, D. Y. Choi, M. A. Vincenti, D. de Ceglia, C. de Angelis, Y. Lu, D. N. Neshev, *Light: Sci. Appl.* **2017**, *6*, e17060.
[247] Z. Zeng, X. Sun, D. Zhang, W. Zheng, X. Fan, M. He, T. Xu, L. Sun, X. Wang, A. Pan, *Adv. Funct. Mater.* **2019**, *29*, 1806874.
[248] J. Ribeiro-Soares, C. Janisch, Z. Liu, A. L. ElìIas, M. S. Dresselhaus, M. Terrones, L. G. Canado, A. Jorio, *2D Mater.* **2015**, *2*, 045015.
[249] C. J. Kim, L. Brown, M. W. Graham, R. Hovden, R. W. Havener, P. L. McEuen, D. A. Muller, J. Park, *Nano Lett.* **2013**, *13*, 5660.
[250] X. Zhou, J. Cheng, Y. Zhou, T. Cao, H. Hong, Z. Liao, S. Wu, H. Peng, K. Liu, D. Yu, *J. Am. Chem. Soc.* **2015**, *137*, 7994.
[251] M. Cheng, S. Wu, Z. Z. Zhu, G. Y. Guo, *Phys. Rev. B* **2019**, *100*, 035202.
[252] Y. Li, Y. Rao, K. F. Mak, Y. You, S. Wang, C. R. Dean, T. F. Heinz, *Nano Lett.* **2013**, *13*, 3329.
[253] N. Leisgang, J. G. Roch, G. Froehlicher, M. Hamer, D. Terry, R. Gorbachev, R. J. Warburton, *AIP Adv.* **2018**, *8*, 105120.
[254] N. Luo, C. Wang, Z. Jiang, Y. Xu, X. Zou, W. Duan, *Adv. Funct. Mater.* **2018**, *28*, 1804581.

© 2020 The Authors. Published by Wiley-VCH GmbH

[255] G. P. Neupane, K. Zhou, S. Chen, T. Yildirim, P. Zhang, Y. Lu, *Small* **2019**, *15*, 1804733.
[256] K. Li, C. Chen, S. Lu, C. Wang, S. Wang, Y. Lu, J. Tang, *Adv. Mater.* **2019**, *31*, 1903914.
[257] M. Diao, H. Li, R. Hou, Y. Liang, J. Wang, Z. Luo, Z. Huang, C. Zhang, *ACS Appl. Mater. Interfaces* **2020**, *12*, 7423.
[258] J. N. Olding, A. Henning, J. T. Dong, Q. Zhou, M. J. Moody, P. J. M. Smeets, P. Darancet, E. A. Weiss, L. J. Lauhon, *ACS Appl. Mater. Interfaces* **2019**, *11*, 40543.
[259] N. Higashitarumizu, H. Kawamoto, C. J. Lee, B. H. Lin, F. H. Chu, I. Yonemori, T. Nishimura, K. Wakabayashi, W. H. Chang, K. Nagashio, *Nat. Commun.* **2020**, *11*, 2428.

Abdus Salam Sarkar received his M.Sc. degree in physics from the Department of Physics and Astrophysics, University of Delhi, India and his Ph.D. degree in emerging 2D materials optoelectronics from School of Basic Sciences, Indian Institute of Technology, Mandi, India, with Prof. Suman K. Pal. Currently, he is a postdoctoral research fellow in the Institute of Electronic Structure and Laser (IESL), Foundation for Research and Technology Hellas (FORTH), Greece with Dr. Emmanuel Stratakis. His research interests focused on introduction of novel 2D materials, understanding of 2D quantum science, and demonstration in optics, optoelectronics, photonics, energy, and biophysical electronic devices.

Emmanuel Stratakis is a research director at IESL/FORTH. He received his Ph.D. in physics and he was appointed as a visiting researcher at the University of California, Berkeley. He is currently leading the "Ultrafast Laser Micro- and Nano-processing" laboratory. His research interests are in the fields of ultrafast laser interactions with materials, nanomaterials, and related applications. He is the director of the Nanoscience Facility of FORTH, part of the NFFA-Europe EU Infrastructure. He is a national representative to the Horizon 2020 High-Level Group of EU on Nanotechnologies and a member of the Scientific Committee of COST.

© 2020 The Authors. Published by Wiley-VCH GmbH